UNIVERSITY OF
LATVIA

Mechanism of Photochromism in Yttrium Oxyhydride and Growth Kinetics of Yttrium Oxide Thin Films

by

Halil Arslan

Submitted to the Faculty of Science and Technology
in partial fulfillment of the requirements for the degree of

Doctorate in Solid State Physics

at the

Institute of Solid State Physics, University of Latvia

April 2025

Thesis supervisors:
Juris Purans, Dr. habil. phys.
Institute of Solid State Physics, University of Latvia, Latvia

Smagul Karazhanov, Dr. habil. phys.
Institute for Energy Technology, Norway
Institute of Solid State Physics, University of Latvia, Latvia

This doctoral thesis has been evaluated, reviewed, and documented by the following members of the committee.

Thesis Supervisors

1. Juris Purāns, Dr. habil. phys.; Institute of Solid State Physics, University of Latvia, Latvia;
2. Smagul Karazhanov, Dr. habil. phys.; Institute for Energy Technology, Norway; Institute of Solid State Physics, University of Latvia, Latvia.

Thesis Reviewers

1. Aline Rougier, Dr.; University of Bordeaux, CNRS, Bordeaux INP, ICMCB, France;
2. Lars Österlund, Professor; Department of Materials Science and Engineering, Uppsala University, Sweden;
3. Andris Anspoks, Dr. phys.; Institute of Solid State Physics, University of Latvia, Latvia.

This doctoral thesis will be defended in a public session of the Promotional Committee of the Faculty of Science and Technology, University of Latvia, on April 25, 2025, at the Institute of Solid State Physics, Ķengaraga Street 8.

The thesis is available at the Library of the University of Latvia, Raina Blvd 19.

Chairman of the Doctoral Committee
Linards Skuja, Dr. habil. phys.; Leading researcher of the Institute of Solid State Physics, University of Latvia.

Secretary of the Promotional Committee
Sintija Siliņa

All rights reserved.
© Institute of Solid State Physics, University of Latvia, 2025
© Halil Arslan, 2025

Acknowledgments

Completing my dissertation would not have been possible without the invaluable guidance of my committee members, the unwavering support of my colleagues and friends, and the encouragement of my family.

First and foremost, I express my deepest gratitude to my supervisors, Dr. habil. phys. Juris Purans and Dr. habil. phys. Smagul Karazhanov, for their exceptional guidance, care, and patience. Dr. Purans directed the research on yttrium oxide (YO) with invaluable expertise and support, while Dr. Karazhanov spearheaded the investigation into yttrium oxyhydride (YHO) through his insightful leadership. Their combined efforts fostered an excellent environment for my research throughout my doctoral studies.

I am equally indebted to Dr. phys. Alexei Kuzmin, whose expertise in X-ray Absorption Spectroscopy (XAS) was pivotal to the success of my research. His continuous advice, mentorship, and critical insights have been instrumental throughout my doctoral journey.

Special thanks to Dr. phys. Ilze Aulika, Ph.D. Inga Pudza, Dr. rer. nat. Georgijs Bakradze, Dr. phys. Martins Zubkins, Dr. phys. Jelena Butikova, Dr. Phys. Guna Krieke, and Dr. phys. Boris Polyakov for their assistance, support, and insightful discussions. Additionally, I wish to express my sincere gratitude to my former colleagues at the Institute of Solid State Physics, University of Latvia, as well as the members of the Thin Film and EXAFS Spectroscopy Research Group.

Preface

Throughout my doctoral journey, I have had the privilege of collaborating with esteemed researchers and participating in state-of-the-art experiments that have significantly enhanced my understanding of advanced materials. My work at DESY PERTA-III P65 and the Tandem Laboratory has been pivotal in refining my expertise in materials characterization techniques that are central to my research.

These collaborative experiences have underscored the power of teamwork in driving scientific advancement. Working alongside specialists from diverse fields has challenged my assumptions and fostered innovation, enabling me to approach complex problems from multiple perspectives. Each collaboration has broadened my understanding and enriched my analytical skills, allowing me to tackle challenges with greater creativity and rigor.

While collaboration has been rewarding, I encountered challenges that prompted me to stay focused on my scientific objectives. Navigating differing perspectives and expectations sometimes led to adjustments in my research plans. These experiences, though not without their complexities, provided valuable opportunities for growth and deepened my commitment to upholding the integrity of my research.

Throughout these hurdles, I remained dedicated to my work and continuously sought innovative ways to advance my research. Each challenge enhanced my problem-solving skills and deepened my commitment to contributing to knowledge in my field. I am grateful for the lessons learned along the way, which have significantly shaped my approach to scientific inquiry.

This thesis represents not only the culmination of years of academic training but also a meaningful contribution to the broader understanding of yttrium-based materials. I hope the insights presented here will inform future research and inspire continued innovation in materials science and solid-state physics, particularly in the development of next-generation photochromic materials and the study of oxidation and/or hydrogenation kinetics of rare-earth elements, with a focus on yttrium.

Mechanism of Photochromism in Yttrium Oxyhydride and Growth Kinetics of Yttrium Oxide Thin Films

by

Halil Arslan

Submitted to the Faculty of Science and Technology
April, 2025
in partial fulfillment of the requirements for the degree of
Doctorate in Solid State Physics

Abstract

Yttrium, a rare-earth metal, plays a vital role in advanced technologies such as fusion reactors[1], superconductors[2], and smart windows[3] due to its versatile chemistry. Yttrium compounds can form either single- or multi-anion systems, with yttrium monoxide (YO), where Y has a 2+ oxidation state (an unusual state for yttrium), representing a single-anion system that exhibits semiconducting properties[4], while yttrium oxyhydride (YHO), as a double-anion system, is known for its unique photochromic behavior under ambient conditions, making it particularly relevant for smart window applications[3].

Despite over a decade of research by multiple groups and efforts toward commercialization, including the production of windows, the mechanism behind the photochromic effect of YHO remains unclear. This gap in understanding hinders advancements in addressing degradation, enhancing photochromic performance, controlling color, increasing durability, and fully utilizing the material's potential applications. In this work, we studied YHO thin films produced by e-beam and reactive magnetron sputtering using various methods, including X-ray absorption spectroscopy (XAS), spectroscopic ellipsometry, X-ray diffraction (XRD), and ion beam instruments, combined with reverse Monte Carlo (RMC) simulations and ab initio multiple-scattering calculations. We report a breakthrough in understanding the mechanism behind the photochromic effect in YHO, rooted in the kinetics of anionic vacancies and the previously observed light-induced lattice relaxation, which enhances our knowledge of its material properties.

In addition, our findings indicate that during the growth, yttrium/yttrium oxide thin films undergo a metal--insulator transition as oxygen partial pressure increases, accompanied by distinct structural transformations (crystalline--amorphous-crystalline) at room temperature. At the same oxygen partial pressure level in the amorphous region, higher deposition temperatures (~623 K) promote the formation of yttrium monoxide (YO) with yttrium in the 2+ oxidation state alongside Y_2O_3, resulting in a semi-transparent, semiconducting material.

Keywords: Yttrium-based multi-anion system, photochromic yttrium oxyhydride (YHO), light-induced structural and chemical transformations in YHO, anionic defects in YHO, Y–Y coordination shell in YHO, oxidation kinetics of yttrium thin films, metal-to-insulator / phase transition in yttrium/yttrium oxide thin films, yttrium monoxide (YO).

Thesis Supervisor: Juris Purans
Title: Dr. habil. phys.
Thesis Supervisor: Smagul Karazhanov
Title: Dr. habil. phys.

Contents

List of Figures

List of Tables

Glossary

UV-VIS	*Ultraviolet-Visible Spectroscopy*
SE	*Spectroscopic Ellipsometry*
trSE	*Time-resolved Spectroscopic Ellipsometry*
MSE	*Mean Squared Error*
DO	*Drude oscillator*
GO	*Gaussian oscillator*
TLO	*Tauc-Lorentz oscillator*
HJPS	*Herzinger-Johs parameterized semiconductor*
XRD	*X-ray Diffraction*
trXRD	*Time-resolved X-ray Diffraction*
FCC	*Face centered cubic*
XPS	*X-ray Photoelectron Spectroscopy*
UPS	*Ultraviolet Photoelectron Spectroscopy*
SEM	*Scanning Electron Microscopy*
TEM	*Transmission Electron Microscopy*
SIMS	*Secondary-ion Mass Spectrometry*
TDCm	*Temperature Dependent Conductivity Measurements*
XAS	*X-ray Absorption Spectroscopy*
XANES	*X-ray Absorption Near Edge Structure*
EXAFS	*Extended X-ray Absorption Fine Structure*
FT	*Fourier Transform*
RMC	*Reverse Monte Carlo*
RDFs	*Radial Distribution Functions*
DFT	*Density Functional Theory*
RBS	*Rutherford Backscattering Spectrometry*
TOF-E ERDA	*Time-of-Flight Elastic Recoil Detection Analysis*
DC	*Direct-Current*
HiPIMS	*High-power Impulse Magnetron Sputtering*

Fundamental Physical Constants

Speed of Light in vacuum (c)	3.00×10^{8} m/s
Planck's Constant (h)	6.626×10^{-34} J.s
Reduced Planck's Constant (ħ)	1.054×10^{-34} J·s
Coulomb Constant (k)	8.99×10^{9} N·m^2 /C^2
Boltzmann Constant (k)	1.381×10^{-23} J/K
Extinction Coefficient (k)	*Dimensionless*
Refractive Index (n)	*Dimensionless*
Permittivity of free space (ε_0)	8.854×10^{-12} F/m
Permeability of Free Space (μ_0)	1.256×10^{-6} N·A^{-2}
Rydberg Constant ($R\infty$)	1.097×10^{7}/m
Wiedemann-Franz Law Constant (L)	$2.44 \times 10^{-8} W\Omega K^{-2}$
Fine Structure Constant (α)	7.297×10^{-3}
Wavelength of Cu K_α radiation	λ= 1.5406 Å
Avogadro's number (N_A)	6.022×10^{23} mol^{-1}
Electron Volt (eV)	1 eV = 1.602×10^{-19} J
Electron Charge (e)	1.602×10^{-19} C
Electron Mass (m_e)	9.109×10^{-31} kg
Bohr Radius (a_0)	5.291×10^{-11} m
De Broglie Wavelength (λ)	h/p; p is momentum
Atomic Mass Unit (AMU)	1amu=1.66054×10^{-27} kg
Alpha Particle Mass (m_α)	6.644×10^{-27} kg

Chapter 1

1 Introduction

1.1 Scientific Context

Yttrium oxyhydride (YHO) belongs to the emerging class of materials called mixed anion systems that include more than one type of anion. Such a material might possess unique properties that are not available in single anion counterparts. As discovered by Mongstad et. al. YHO, exhibits photochromic properties at room temperature[3]. Upon illumination with sunlight, the material absorbs the UV light and changes its color from the transparent state with transmittance T>85% to the Photodarkened state with T<30%.

Table 1-1 | Performance analysis for electrochromic, thermochromic, and photochromic films.

Parameter	EC	TC	PC	
		VO_2	YHO	WO_3 (hybrid)
Consumes energy	Yes	No	No	No
Human presence	Yes	No	No	No
Fabrication cost	High	Low	Low	Low
Price per m^2	250-700 Euro	~12 Euro	<10 Euro	
Critical elements	Yes	Yes	Yes	Yes
Mechanism	⧗	⧖	⧫	
Switching optical properties	<5s	<5s	>5 min	>1 min
Bleaching time	<5s	<5s	>10 min	>5 min
Contrast	>40%	<40 %	30-50%	30-50 %
Transmittance	>85%	<60%	>85%	>85%
Durability	15-20 years	>15 years	>10 years	>5 years

EC- Electrochromic; TC- Thermochromic; PC- Photochromic
⧗ Ion transport between layers enhances degradation.
⧖ Structural rearrangement
⧫ Local structural rearrangement around anion vacancies.
Durable coatings are expected.

Unlike conventional inorganic oxide-based chromic films that require heating or an electric field for bleaching, YHO offers both photodarkening and bleaching under ambient conditions without the need for additional energy

input. Furthermore, the limited lifespan of polymer-based photochromic materials, often containing hazardous chemicals, restricts their commercial viability. In contrast, YHO is the first inorganic photochromic material with substantial commercial potential for applications in building windows, goggles, helmet visors, and automotive roof glass, achieved without hazardous chemicals during its deposition. This highlights YHO's technological significance relative to current smart coatings (refer to Table 1.1).

Research on yttrium oxyhydride (YHO) has gained traction among scientists from various countries, including the Netherlands, Sweden, Germany, the USA, China, Latvia, Estonia, and India. Since 2017, YHO and related materials have been key topics at MRS and E-MRS Symposia. In 2018, systematic research led by Smagul Karazhanov culminated in the establishment of Sunphade AS, which began producing YHO-based photochromic films on flexible substrates using roll-to-roll technology in April 2024. Despite over a decade of investigation, the mechanism underlying the photochromic effect remains an open question among researchers.

By the extended X-ray absorption fine structure (EXAFS) for the oxyhydrides of Gd[5] and Y[6], it was shown that upon air exposure, most O^{2-} anions enter the tetrahedral sites of the fcc-lattice. This proves the mixed anion nature of the Gd- and Y-based oxyhydrides. However, no EXAFS study was performed about local structural arrangements around anion vacancies in the transparent and Photodarkened states and no attempt was made to relate it to the photochromism of YHO.

Intrinsic point defects and impurities have also been studied by some authors[7-9]. However, the role of the defects in the photochromic properties of YHO is not clarified.

Here by employing first-principles calculations combined with the x-ray diffraction (XRD), extended x-ray absorption fine structure (EXAFS), optical ellipsometry, and ion beam instruments, we report a breakthrough result about the mechanism of the photochromic effect in YHO and of the earlier reported light-induced lattice relaxation.

Yttrium oxide systems, belonging to the category of single-anion materials, represent a promising research frontier due to their considerable potential in advanced technologies. Yttrium primarily exists in the 3+ oxidation state and can adopt three crystal phases: cubic (α), monoclinic (β), and hexagonal (γ). Trivalent yttrium oxide (Y_2O_3) showcases exceptional properties, such as a high melting point (~2700 K), a substantial optical excitation threshold (~5.6 eV), and remarkable mechanical and chemical

stability. Growing interest in the 2+ oxidation state has led to investigations into yttrium monoxide (YO). Although early studies began in 2016[4], there have been no prior reports of divalent yttrium oxide deposition via reactive pulsed-DC magnetron sputtering from a metallic target. This research fills a critical gap in understanding yttrium's oxidation dynamics, marking the first successful production of solid-phase YO through this technique.

1.2 Motivation

As technological advancements increasingly rely on materials with precisely controlled and adaptable properties to meet extreme and diverse functional demands, deepening our understanding of these systems is essential for driving future innovations. Rare-earth elements, such as yttrium with its exceptional electronic configuration, have become pivotal in this progress, serving as versatile platforms for exploring cutting-edge material functionalities and offering transformative potential across a wide range of advanced applications.

This doctoral research aims to advance the understanding of yttrium-based materials, with a particular focus on the photochromic behavior of yttrium oxyhydride (YHO). As a multi-anion compound, YHO offers a unique framework for exploring novel mechanisms underlying light-induced phenomena, making it a significant subject of study in materials science and solid-state physics.

Furthermore, the investigation of yttrium and yttrium oxide thin film formation under ultralow/low oxygen partial pressures offers valuable insights into material synthesis and structural kinetics. Complementing this, the study of yttrium monoxide (YO) addresses critical gaps in scientific understanding, as its formation mechanisms and physical, chemical, and/or structural properties deviate from theoretical predictions. These findings present opportunities to refine existing models and enhance our knowledge of this distinctive material.

1.3 Objective of the Thesis

This doctoral research aims to deepen the understanding of yttrium-based double-anion (H, O) system, with particular emphasis on yttrium oxyhydride (YHO) in thin film form and its light-induced chromic properties. Additionally, the study explores yttrium-based single-anion (O) system.

1- Yttrium Oxyhydride (YHO) System (Primary Focus):

I- Role of intrinsic point defects in local structural arrangements in YHO.
II- Role of intrinsic point defects in photochromic properties and lattice contraction in YHO.
III- Establishing stoichiometry of the YHO films.

2- Yttrium Oxide (YO) System (Secondary/ Supplementary Focus):

I- Understanding the transition from metallic to fully oxidized states in yttrium thin films, providing insights into the metal-to-oxide transformation process.
II- Investigating the conditions required to obtain/stabilize divalent yttrium (YO) in the solid phase, contributing to a broader understanding of the chemical and structural factors involved in this less common oxidation state.

1.4 Scientific Novelty

1- Yttrium Oxyhydride (YHO) System:

I- By employing EXAFS measurements combined with RMC simulations, we demonstrate that anion vacancies and interstitial hydrogen can cause local structural arrangements that split the radial distribution function (RDF) for Y-Y cations in YHO thin films, a property that persists within the temperature range of 10–300 K.

II- By combining ellipsometry measurements with DFT modeling, we show that anion vacancies form deep-level defect states in the band gap of YHO, which absorb UV/blue light and transfer electrons from the valence band to these defect states. The mechanism of the photochromic effect is related to the absorption of UV/blue light by the defect states, without changing the oxidation state of the majority of Y cations. This finding is consistent with studies of the oxidation state of Y conducted using EXAFS measurements.

III- By RBS and ERDA measurements, we demonstrated that the YHO films are not stoichiometric and have a high concentration of anion vacancies.

2- Yttrium Oxide (YO) System:

Phase Transition Insights:

I- The study reveals how crystalline--amorphous-crystalline (metal--insulator) transitions correlate with variations in oxygen partial pressure during deposition.

II- A previously unreported range of oxygen partial pressures, spanning from ultralow (~10^{-7} Pa) to low (~10^{-3} Pa), provides new insights into yttrium-based oxide thin film behavior under these conditions.

Formation and Characterization of Amorphous and Semiconducting Phases:

I- At an oxygen partial pressure of approximately 7.57×10^{-5} Pa, the material undergoes a transition to a fully amorphous, semi-transparent phase during deposition.

II- Concurrently, at deposition temperatures near 623 K, semiconducting yttrium monoxide (YO) is formed, coexisting with yttrium oxide (Y_2O_3) in both cubic and amorphous phases, contributing to the semi-transparent nature of the material.

Terminological Clarification:

1- It is important to note that there is no universally accepted definition of YHO. In this study, we will refer to the compound as yttrium oxyhydride until the results and discussion chapter, where the designation of YHO will be adapted based on the context of the research findings.
2- In the Results and Discussion section of this dissertation, characterization methods are primarily categorized under general titles based on the investigated property rather than the specific techniques used. For example, the term 'chemical characterization' refers to the analyzed property, such as the oxidation state, rather than the method employed for its determination.
3- A powder is a collection of fine, discrete solid particles, typically ranging in size from sub-microns to millimeters. It can be produced through various methods, including chemical synthesis, mechanical grinding, or the fragmentation of materials, such as bulk solids and thin films.

1.5 Author's Contribution

This doctoral research is inherently multidisciplinary, integrating multiple advanced experimental techniques and theoretical calculations to achieve a comprehensive understanding of the materials' properties and behaviors.

The research can be separated into two main sections. The first section covers the production of thin film samples employing magnetron sputtering (DC, Pulsed DC, and High-power impulse) and thermal evaporation (e-beam). Y (by magnetron sputtering and e-beam evaporator), YO (by magnetron sputtering and e-beam evaporator), and photochromic YHO (by e-beam evaporation) thin films were produced in the multi-functional vacuum cluster tool at the ISSP clean room in Riga, Latvia. Y thin film and photochromic YHO, including a large area, were produced at the Institute for Energy Technology clean room in Kjeller, Norway by DC magnetron sputtering. All the material productions were done by the author of the treatise.

The second section involves the characterization of the produced materials, which is divided into two subsections: laboratory-scale characterizations and large-scale research infrastructure based characterizations. The laboratory-scale characterizations include Ultraviolet-Visible Spectroscopy (UV-VIS), Spectroscopic Ellipsometry (SE), X-ray Diffraction (XRD), X-ray Photoelectron Spectroscopy (XPS), Scanning Electron Microscopy (SEM), Transmission Electron Microscopy (TEM), Secondary-ion Mass Spectrometry (SIMS), and Temperature Dependent Conductivity Measurements (TDCm). The large-scale research infrastructure based characterizations comprise X-ray Absorption Spectroscopy (XAS) at DESY PERTA-III P65 undulator beamline in Hamburg, Germany, as well as Rutherford Backscattering Spectrometry (RBS) and Time-of-Flight Elastic Recoil Detection Analysis (TOF-E ERDA) at the Tandem Laboratory in Uppsala, Sweden.

The Author of the thesis made the following contributions:

Conceptualization and Methodology: The author played a central role in the initial conceptualization of the research, particularly in designing the experimental framework for the laboratory-scale characterizations (UV-VIS, SE, XPS, XRD SEM, TEM, SIMS, TDCm) and the large-scale research infrastructure based characterizations (XAS, RBS, TOF-E ERDA). This involved defining the objectives, selecting appropriate characterization

techniques, and establishing the methodology required to meet the research goals.

Data Collection: The author actively performed/participated in the data collection process, particularly for UV-VIS, SE, TDCm, XAS, XRD, RBS, and TOF-E ERDA. This involved operating sophisticated instrumentation, calibrating equipment, and ensuring the accuracy and reliability of the data obtained from these techniques.

Data Analysis and Interpretation: The author conducted in-depth analyses of the data from UV-VIS, SE, XRD, XPS, SEM, TEM, TDCm, and XAS. The author also interpreted the results in the context of existing literature, contributing to the development of novel conclusions about the properties of the synthesized materials.

Visualization: The author was responsible for the visualization of the data, including the creation of graphs, charts, and other illustrative materials that effectively communicated the findings of the study. This included the visualization of results from UV-VIS, SE, XRD, XPS, SEM, TEM, TDCm, and XAS, ensuring that the data were presented in a clear and accessible manner to support the study's conclusions.

Supportive Roles and Computational Section:

The author of this thesis contributed to the analysis and visualization of the results.

Smagul Karazhanov and K. Vinoth Kumar:
Conducted first-principles calculations pertinent to the research.

Alexei Kuzmin:
Directed the X-ray Absorption Spectroscopy (XAS) efforts, including the design of experiments, data acquisition, and analytical processing, and performed EXAFS-related computational work (RMC, DFT).

Ilze Aulika:
Directed the Spectroscopic Ellipsometry (SE) studies, focusing on the development of measurement protocols and the analysis of results by Copmelete ESASE (J.A. Woollam).

1.6 Structure of the Thesis

The thesis is structured into eleven chapters: eight main chapters, followed by three additional chapters, which include the developed theses along with a list of the author's participation in conferences, international schools, and large-scale research infrastructure-based experiments; the bibliography; and the appendix.

Main Chapters

Chapter 1: This introductory chapter covers the scientific context, motivation, objectives, scientific novelty, the author's contributions, and the overall structure of the thesis.

Chapter 2: This chapter provides a literature review of the materials investigated in this study.

Chapter 3: This chapter outlines the production methods and characterization techniques utilized in the research, providing the principal information necessary for understanding these production and characterization methods.

Chapter 4: This chapter primarily examines the kinetics of yttrium/yttrium oxide thin films under ultra-low to moderate oxygen partial pressure, with a specific focus on the formation kinetics of yttrium monoxide (YO).

Chapter 5: This chapter analyzes photochromic YHO thin films characterized as stoichiovariants, produced through e-beam evaporation, and compares their properties with those of films obtained via magnetron sputtering.

Chapter 6: This chapter investigates local structural and chemical variations in the photochromic YHO structure as a function of temperature, specifically under cryogenic conditions.

Chapter 7: This chapter studies light-induced structural and chemical alterations at the atomic and nanoscale levels within the photochromic YHO thin film.

Chapter 8: This concluding chapter summarizes the main interpretations derived from the study and explores the connection between yttrium-based single anion systems (O) and double anion systems (O, H).

Additional Chapters

Chapter 9: This chapter presents the list of theses developed in this dissertation, along with the author's patents and publications during the doctoral study. Additionally, it includes a list of the author's participation in conferences, international schools, and large-scale research infrastructure-based experiments.

Chapter 10: Bibliography.

Chapter 11: Appendix, including additional images and tables related to the research.

Chapter 2

2 Literature Review

2.1 Overview: Yttrium-Based Materials

Yttrium is a versatile element with significant applications in advanced materials and emerging technologies. It is a critical component in high-performance materials such as Yttrium Barium Copper Oxide (YBCO; $YBa_2Cu_3O_{7-\delta}$), a high-temperature superconductor used in powerful magnets for Magnetic Resonance Imaging (MRI) machines[10], and maglev trains[11].

Yttrium Aluminum Garnet (YAG) lasers, often doped with neodymium (Nd), are utilized in medical procedures[12], and military applications[13] due to their efficiency and stability.

In aerospace and automotive industries, yttrium is alloyed with magnesium and aluminum to improve strength, thermal resistance, and oxidation resistance, making these alloys crucial for lightweight, high-strength engine components[14].

Its biocompatibility and corrosion resistance make yttrium suitable for medical implants and prosthetics, enhancing their durability[15].

Yttrium oxide (Y_2O_3) stabilizes zirconia (YSZ), enhancing its thermal and chemical stability, and is widely used in fuel cells[16], oxygen sensors[17], and thermal barrier coatings[18].

Yttrium is used in Oxide Dispersion Strengthened (ODS) steels to enhance high-temperature strength, radiation resistance, and corrosion resistance, with reduced activation and improved microstructural stability[19,20].

Yttrium's capacity to form stable hydrides renders it highly valuable for hydrogen storage applications[21]. Yttrium hydride (YH) is noted for its high-temperature superconductivity[22]. Additionally, yttrium oxyhydride (YHO) exhibits photochromic properties, making it a promising candidate for smart window technologies in buildings, and automotive roof glass[3,23,24].

Table 2.1 provides the fundamental structural characteristics of yttrium (Y), as well as the binary (Y-O, Y-H) and ternary (Y-H-O) relationships between the cation and anions. The table also discusses the physical, chemical, and/or structural properties associated with these relationships, such as photochromism, insulating behavior, superconductivity, and semiconducting properties.

Additionally, Table A.1 provides comprehensive data on the atomic structure, physical properties, and thermodynamics of Y. Tables A.2 and A.3 offer fundamental data on the atomic structure, physical properties, and

thermodynamics of oxygen (O) and hydrogen (H), respectively, supporting a detailed understanding of these elements' roles and interactions.

Table 2-1 | Yttrium-based single and double anion systems. Basic physical, chemical, and/or structural characteristics of Y, YO, YH, and YHO materials.

<table>
<tr><th colspan="6">Y-O-H</th></tr>
<tr><th>Cation</th><td colspan="5">Y</td></tr>
<tr><th rowspan="5">Structure / Structural transformation</th><td colspan="2">Temperature dependency, 1 atm</td><td colspan="3">Pressure dependency, 300 K</td></tr>
<tr><td>Crystal Phase</td><td>Transition</td><td>Crystal Phase</td><td colspan="2">Transition</td></tr>
<tr><td>hcp
(0 - 1751 K)
α-phase [25]</td><td rowspan="3">(1751 K, 1 atm)
hcp »
bcc [25]</td><td>hcp [26]</td><td colspan="2" rowspan="4">~ 10 GPa
hcp » hex
(Sm-type) [27]
~ 26 GPa
hex » hex
(dhcp) [28,29]
~ 39 GPa
dhcp » fcc [26]
> 40 GPa
fcc » hex
symmetry [29]
(expectative)</td></tr>
<tr><td rowspan="2">bcc
(1751 – 1795 K)
β-phase [25]</td><td>hex [27]
(Sm-type)</td></tr>
<tr><td>hex
(dhcp) [28]</td></tr>
<tr><td>fcc [26]</td></tr>
<tr><th>Anion 1</th><td colspan="5">O</td></tr>
<tr><th>Anion 2</th><td colspan="5">H</td></tr>
<tr><th>Pairing</th><td colspan="3">Single cation
Single anion</td><td colspan="2">Single cation
Double anion</td></tr>
<tr><th>System</th><td colspan="2">Y-O</td><td>Y-H</td><td colspan="2">Y-O-H</td></tr>
<tr><th>Phase</th><td>YO</td><td>Y_2O_3</td><td>YH</td><td colspan="2">YHO</td></tr>
<tr><th>Crystal structure (Literature)</th><td>Cubic
Orthorhombic
Tetragonal</td><td>Cubic
Monoclinic
Hexagonal</td><td>Hexagonal
Cubic
Triclinic</td><td colspan="2">Cubic</td></tr>
<tr><th rowspan="2">Properties</th><td>Bulk/Metallic/
⧗</td><td rowspan="2">Insulating
⧫</td><td rowspan="2">Insulating
Metallic
⧖</td><td colspan="2" rowspan="2">Photochromic</td></tr>
<tr><td>Thin film/
Semiconducting</td></tr>
</table>

⧖ Superconducting at high pressure
⧗ Superconducting at high pressure and high temperature
⧫ Good thermal and chemical resistance

Some of the physical, chemical, and/or structural properties of YH and Y_2O_3 are outlined in Table 2.1. These properties are provided solely for comparative purposes and will be discussed briefly.

While the table highlights key physical, chemical, and/or structural properties, it does not comprehensively address variations within these systems, such as the influence of stoichiometry, structural forms, or their specific relationships to physical, chemical, and/or structural behaviors. The table is designed to illustrate the broad diversity of these materials and their potential characteristics. Following this, Chapter 2.2 will delve into YO, while Chapters 2.3 and 2.3.1 will focus on yttrium-based multi-anion and photochromic YHO structures, respectively.

YH structures display a broad spectrum of electrical properties, ranging from insulating to superconducting, depending on the hydrogen concentration and external factors such as applied pressure and temperature. A theoretical study by Liu et al.[30] predicted the pressure-dependent crystal structures of YH_x (x=2, 3, 4, 6, 8, 10, 12), observing a structural transition from P6/mmm to C2/c based on hydrogen concentration. This study also suggested that YH_{10} might possesses superconducting properties, although a subsequent experimental study[31] failed to stabilize YH_{10}.

YH_6, which shares the same crystal structure Im-3m, has demonstrated superconducting behavior under various conditions: between 251 and 264 K at 120 GPa (theoretical)[32]; at 227 K and 237 GPa (experimental)[31]; and 224 K and 166 GPa (combined theoretical and experimental)[33].

Furthermore, at ambient pressure, the incorporation of hydrogen into the yttrium crystal lattice (refer to Tables A.1, A.3, and 2.1) can lead to a transition from metallic to insulating behavior, as observed in $YH_{1.8}$ to $YH_{2.9}$[34]. The same experimental study also found that $YH_{3-\delta}$ might exhibit semiconducting properties with an optical excitation threshold of 1.8 eV. Additionally, another study[35] predicted that YH_3 might exhibit superconducting properties under high pressure (18 GPa) and low temperature (40 K). However, despite these theoretical predictions, subsequent experimental attempts[31,36] have been unable to confirm the superconducting state of YH_3.

The studies referenced above highlight the challenges in stabilizing these phases under the predicted conditions, emphasizing the need for further research into the phase kinetics of YH under high pressure. To address this gap, Purans et al.[22] investigated the local structural arrangement around the cation, focusing on the transition from a hexagonal to a cubic structure in YH_3. They reported the pressure-dependent transition from hexagonal to cubic at approximately 20 GPa, and a transition from an insulator to a metal around 50

GPa. However, their results did not include the observation of a critical temperature for superconducting transition. Additionally, they identified a region described as a gapless semi-metal, which could provide supportive evidence for the findings reported by Huiberts et al.[34].

2.2 Yttrium's Oxidation Chemistry: Divalent Yttrium

The electronic configuration of yttrium is represented as [Kr] $5s^2$ $4d^1$, indicating the orbital filling order of its electrons (refer to Table A.1). However, yttrium achieves its most stable state when it loses all three valence electrons, adopting a noble gas-like configuration similar to krypton. Upon the loss of three electrons, yttrium forms a Y^{3+} ion, characterized by an effective ionic radius of 90 pm and a crystal radius of 104.0 pm (for coordination number 6; refer to Table A.1 for additional details)[37] In this trivalent state, Y^{3+} can bond with hydrogen, often resulting in a hexagonal structure as previously described[22].

When hydrogen is replaced by oxygen, yttrium forms yttrium oxide. Depending on the specific conditions, yttrium can exhibit oxidation states ranging from 2+ to 3+. The most common oxidation state is 3+, forming yttrium oxide (Y_2O_3), which can exist in three distinct crystal phases: cubic (α phase), monoclinic (β phase), and hexagonal (γ phase)[38-41].

The structural variations of Y_2O_3 are influenced by the ionic radius of the rare-earth element and anion (refer to Tables A.1 and 2) and temperature, leading to five different polymorphic forms[39]. Yttrium oxide (Y_2O_3) exhibits several exceptional properties, including a high melting point (~2700 K)[42], a high optical excitation threshold (~5.9 eV)[43], and notable mechanical and chemical stability. These characteristics make Y_2O_3 highly relevant in various advanced applications. Due to the multifaceted nature of trivalent yttrium oxide structures, much of the existing research has been focused on exploring its dielectric and catalytic properties [44,45].

Divalent yttrium, with the electronic configuration [Kr] $4d^1$, is a rare and unconventional formation[46] that has recently gained significant attention from researchers[4,47] due to its unique properties including semiconductor behavior [4,48], and superconductivity[49].

In this thesis, the state of the art of divalent yttrium oxide (YO) will be examined through both theoretical approaches and experimental verification, presented in chronological order. As previously mentioned, discrepancies exist between theoretical predictions and experimental results for yttrium

hydride (YH) structures, which may provide valuable insights into the behavior of YO.

The first major discussion on the formation of divalent yttrium in the solid state was conducted by Kaminaga et al. in 2016[4]. Their study successfully demonstrated the deposition of YO using the pulsed laser (PL) from an insulating target material (Y_2O_3). However, the deposited material was a mixture of YO and Y_2O_3. They reached two key conclusions: YO forms in cubic unit cells with tetragonal distortion and exhibits semiconducting properties.

Subsequent theoretical calculations[47] examining metastable sub-oxide structures for Y-O, Zr-O, and Hf-O suggested that YO forms in orthorhombic and pseudo-degenerate orthorhombic unit cells with metallic conductivity, contrary to experimental observations. These calculations also proposed that orthorhombic YO might arise from anionic defects in Y_2O_3.

A study by Yang et al. in 2021[49]. Revealed that bulk YO adopts two distinct unit cell structures based on the applied pressure: a higher symmetry cubic structure (Fm-3m) above approximately 9.9 GPa and a lower symmetry cubic structure (Pm-3m) between approximately 110 and 300 GPa. The study also concluded that NaCl-type YO exhibits superconductivity at 13.0 K and 25 GPa. Additionally, it was found that the orthorhombic and pseudo-degenerate orthorhombic phases suggested by[47] are less thermodynamically stable compared to Y_2O_3 at near-ambient pressures.

In 2023, we deposited YO using magnetron sputtering from a metallic target material. Our research was the first to successfully obtain divalent yttrium from a metallic target and by magnetron sputtering. However, as noted by[4], the material we produced was not a single-phase compound but rather a mixture of Y_2O_3 and YO. Additionally, we observed a higher degree of amorphization than what was reported by Kaminaga et al.[4] While neither study calculated the degree of crystallinity, this can be further assessed through analysis of the X-ray diffractograms. We also noted that our material exhibited semiconducting behavior, which is consistent with the d-cubic crystal structure reported in[4].

Following our article, another study combining theory and experiment was published in 2023[50]. This research, like the other theoretical studies mentioned, investigates yttrium monoxide in bulk/powder form. The study demonstrated that at high pressure (15 GPa) and high temperature (1837 K), YO with an Fm-3m crystal structure could be synthesized. Additionally, the research team succeeded in producing mixed oxides containing YO at

relatively lower temperatures (1637 K and 1473 K) and lower pressure levels (10 GPa). One of the most striking results of this research is that the superconducting transition in YO, which had been suggested by previous studies, was not observed. Moreover, the research does not report the electrical characteristics of the material.

The referenced studies highlight the increasing scientific significance of YO in the 2+ oxidation state, making it a prominent and current topic of interest.

2.3 Yttrium-Based Multi-Anion Systems

This chapter emphasizes the significance of yttrium-based multi-anion structures and their role in current and emerging technologies. Before exploring the specifics of yttrium oxyhydride (YHO) structures the primary focus of this thesis (and will be discussed in chapter 2.3.1) we will briefly outline the key characteristics of selected multi-anion systems.

Yttrium-Based Multi-Anion Systems are complex compounds in which yttrium combines with various anions to form advanced materials. An example is yttrium oxyfluoride (YOF), where yttrium is in the 3+ oxidation state, existing in both stoichiometric and non-stoichiometric forms[51]. Stoichiometric YOF is widely used in advanced ceramics, primarily due to its superior plasma resistance compared to Y_2O_3[52-54]. The non-stoichiometric form, known as the Vernier phase, is distinguished by its ability to incorporate various rare-earth elements such as Tb^{3+}, Er^{3+}, and Ho^{3+}, enhancing its suitability for fluorescence-based applications[55]. Interestingly, the same study[55] identified an intermediate phase, $Y(CO_3)_{1-x}(OH)_3F_{1+2x+y,}$ which plays a crucial role in the formation of the Vernier phase YOF.

Yttrium oxychloride (YClO), although not a final product, serves as a reactive intermediate in carbochlorination reactions due to its ability to undergo anionic exchange. During carbochlorination, oxygen anions in yttrium compounds are replaced by chloride anions, facilitating the production of high-purity yttrium chloride. This process transforms stable yttrium oxide (Y_2O_3), which makes direct yttrium extraction difficult, into yttrium chloride (YCl_3), which can be more easily reduced to metallic yttrium[56]. This technique is versatile and extends beyond yttrium, as it can be used to extract other rare earth metals such as neodymium, and Cerium[57].

The unique physical, chemical, and/or structural properties of yttrium-based multi-anion systems have attracted significant interest from research

teams exploring multi-anionic compounds. A study led by A. Pishtshev[58] theoretically examined the electrostatic properties of predicted rare-earth-based compounds $Ln_2OF_{2-x}Cl_xH_2$, where Ln stands for Gd, Y, and La. These materials show great potential for use in sensors that detect mechanical stress, which is vital for controlling and monitoring mechanical loads.

Furthermore, these compounds are promising as highly sensitive tactile sensors that operate across a wide range of forces, from 0.01 N to 1000 N, making them ideal for applications that require precise touch or force detection, such as robotics and medical devices. Their responsive nature could also be leveraged in the development of artificial skin, enhancing tactile feedback in robots and prosthetics and expanding their use in advanced electromechanical systems.

However, the study suggests promising potential for $Ln_2OF_{2-x}Cl_xH_2$. To the best of the authors' knowledge, there are no reported experimental studies on this material to date.

2.3.1 Photochromic Yttrium Oxyhydride

Yttrium oxyhydride (YHO) is classified as a multi-anionic compound[59,60] that represents photochromic properties at ambient conditions[3,7,61-64], making them of interest for building window applications. The production of YHO involves two key stages: First, Yttrium Hydride (YH) thin films with face-centered (fcc) crystal structure, which contain a single cation and single anion, are produced using techniques such as magnetron sputtering[61,65-68], and e-beam evaporation[69-71]. Second, these YH films undergo a post-oxidation process to form YHO, which incorporates a single cation and double anions. This second stage can be referred to as anion exchange or anion balancing, and results in structural relaxation of the initial material (YH). Ultimately a material that contains Y, H, and O is produced. Furthermore, the material can be synthesized in powder form through chemical processes[72,73] and magnetron sputtering[74].

YHO has been reported into two distinct chemical formulas: $YH_{3-2x}O_x$[60,75], and $YH_{2-x}O_x$[66,70,76]. Both are characterized by a face-cantered cubic (fcc) crystal structure[61,70]. Further studies[65,74] on the crystal structure of the material confirm its classification within the cubic (FCC) crystal family. Structural characterization using Rietveld refinement was performed on a powder sample obtained by scraping a YHO thin film deposited through magnetron sputtering[65]. However, definitive conclusions regarding the

Wyckoff positions of the ions, particularly hydrogen and oxygen, remain uncertain. Synchrotron radiation and neutron powder diffraction measurements presented in[77], revealed that oxygen anions occupy tetrahedral sites alongside hydrogen anions within the structure. Furthermore, another study[7] confirms that in magnetron-sputtered powders, hydrogen occupies interstitial tetrahedral sites, while oxygen occupies both tetrahedral and octahedral sites, resulting in the formation of hydrogen and oxygen rich regions. Around the same time, we reported[69] the stoichiovariants photochromic oxidized yttrium hydride thin films produced by e-beam evaporation.

One of the next crucial aspects to address was the anionic ratio (H/O), which we recently explored in our study[65]. This topic will be comprehensively examined in the results and discussion chapter of the thesis.

As indicated, YHO can be produced by various methods, each directly influencing its structure, composition, and characteristics. Films of YHO made by magnetron sputtering or electron beam evaporation exhibit high resistivity[3], while epitaxial films deposited via magnetron sputtering can show high conductivity[64]. Additionally, the literature indicates that the photochromic performance of YHO films deposited by magnetron sputtering[62,63] is superior to that of films produced by electron beam evaporation[70,71]. However, research on the photochromic properties of YHO films produced by electron beam evaporation is relatively sparse. Essential information about the relationship between film composition, microstructure, and photochromic performance is still missing[70]. We address this gap in article[69], which will be elaborated upon in the results and discussion chapter of this thesis.

The electron beam evaporation method is significant due to its cost-effectiveness and user-friendly nature, especially compared to magnetron sputtering. Although magnetron sputtering is commonly used in the glass industry for large-area depositions and provides uniform film coverage, it often has slower deposition rates when reactive sputtering is used and consumes more electrical energy to maintain the plasma.

Existing literature identifies two main approaches for understanding the kinetics behind the transition between transparent and dark states in YHO. The first approach examines the structural and chemical changes that occur. For instance, a 2020 study by Baba E.M. et al. provided insights into the light-induced reversible structural transformations in photochromic YHO[63]. It was

also suggested[7] that the reduction of the cation's oxidation state results from the interaction between the excited electron and the cation.

The second approach focuses on anion transfer, particularly the interactions between multiple or dual phases. In 2020, Hans, M. et al. published a study on photochromic gadolinium oxyhydride and its formation of dual phases (Gd_2O_3, and GdH_2) formation. Their research proposed photon-induced hydrogen transfer between these phases. This phenomenon led them to conclude that photochromism in gadolinium/yttrium oxyhydride arises from the dynamic interaction and exchange of hydrogen atoms between the REM_2O_3, and $REMH_2$ (REM: Gd, Y)[78].

Additionally, previous research[79] has shown that the photochromism of Y(D, H)O films is not related to long-distance material transport. There is no evidence of light-induced or thermal diffusion of hydrogen over large distances, even though deuterated thin films display a robust photochromic response.

In conclusion, although several hypotheses have been proposed, including electron-cation interactions and structural rearrangements under light exposure (as referenced above), the exact mechanisms driving the reversible optical changes in YHO remain poorly understood. This complexity highlights the need for further experimental and theoretical research to elucidate the intricate interplay of electronic, structural, and chemical factors that contribute to its photochromic behavior.

Therefore, building on the referenced studies we conducted[65,69] this dissertation delves deeper into the atomic and nanoscale kinetics of YHO, as detailed in Chapters 5, 6, and 7.

Chapter 3

3 Methodology

3.1 Introduction

The methodology of this research is designed to systematically investigate/represent the production and characterization methods of Y, YO, and YHO thin films. It encompasses two main phases: material synthesis and material characterization.

This chapter serves to elucidate the key theoretical frameworks and fundamental physical principles that underpin the production and characterization techniques utilized in this research. The equations presented within this section are intended to illustrate the underlying physical phenomena associated with these methods, providing a conceptual understanding without delving into comprehensive derivations or theoretical proofs, which exceed the scope of this work. For those seeking in-depth mathematical treatments, readers are encouraged to consult standard academic textbooks and relevant literature discussed in the corresponding sub-chapters.

It is essential to emphasize that specific experimental procedures and protocols for material production and characterization are thoroughly documented in the associated articles, which form the foundational basis for this dissertation. This chapter highlights the theoretical principles underlying the employed methodologies, while including only the necessary experimental details within the relevant chapters to support a focused discussion.

Material Synthesis:

The synthesis phase focuses on the production of thin films using advanced deposition/evaporation techniques. Y, YO, and YHO thin films were produced using both magnetron sputtering (DC, pulsed DC, and high-power impulse) and thermal evaporation (e-beam evaporation). To prevent contamination or degradation, all the samples were stored in a glovebox with a controlled atmosphere (Ar or N), ensuring stable conditions for subsequent analysis

Magnetron Sputtering: This technique was employed to deposit Y, YO, and YHO thin films, both at the laboratory scale and as large-area YHO films.

1- Laboratory-Scale Thin Film Deposition: Y, YO, and YHO thin films were deposited at 298 and 623K (∓5) using a magnetron sputtering system integrated into a multi-functional vacuum cluster tool, operated within an ISO 8 class clean room environment. (Institute of Solid State Physics, University of Latvia, Latvia)

2- Large-Scale Thin Film Deposition: YHO thin film deposition at 298K (∓5). was performed using a Leybold Optics A550V7 magnetron sputtering system. (Institute for Energy Technology, Norway)

The deposition parameters, such as power, pressure, and substrate temperature, were carefully optimized to produce films with the desired material properties. Powder samples (YHO) were then obtained by scraping the thin film off the large-area samples produced via this method.

E-beam Evaporation: This technique was used to grow metallic yttrium, fully oxidized yttrium, and photochromic YHO films at 298K (∓5). The process was conducted using a system integrated into a multi-functional vacuum cluster tool, operated within an ISO 8 class clean room environment. (Institute of Solid State Physics, University of Latvia, Latvia)
Evaporation parameters, including e-beam current and chamber pressure, were carefully optimized to achieve films with the desired structural characteristics.

Material Characterization:

After production, the thin film (and powder) samples were subjected to a comprehensive set of characterizations to assess their structural, chemical, optical, and electronic properties. This characterization phase is divided into laboratory-scale and large-scale research infrastructure based techniques.

Laboratory-Scale Characterization:

Ultraviolet-Visible Spectroscopy (UV-VIS): Employed to measure the optical transmittance and absorbance of YO, Y_2O_3, and photochromic YHO thin films. (Cary 7000 Spectoremeter; Institute of Solid State Physics, University of Latvia, Latvia)

Spectroscopic Ellipsometry (SE): Used to determine the film refractive index, extinction coefficient, and thickness. (RC2-XI, Wollam; Institute of Solid State Physics, University of Latvia, Latvia)

X-ray Diffraction (XRD): Applied to assess the crystalline structure and phase composition of the films. (Rihaku, Miniflex, Cu K_{α}; Institute of Solid State Physics, University of Latvia, Latvia)

X-ray Photoelectron Spectroscopy (XPS): Utilized to analyze the elemental composition and oxidation states of the elements on the film surface and for depth profiling. (ThermoFisher, ESCALAB 250Xi; Institute of Solid State Physics, University of Latvia, Latvia)

Scanning Electron Microscopy (SEM) and Transmission Electron Microscopy (TEM) are employed to visualize the film morphology and microstructure. (SEM, Tesca Lyra; TEM, Fei Tecnai; Institute of Solid State Physics, University of Latvia, Latvia)

Scanning Electron Microscopy/Focused Ion Beam (SEM-FIB): Lamella extraction from YHO thin films for TEM charecterizations. (Helios 5 UX, Thermo Scientific; Institute of Solid State Physics, University of Latvia, Latvia)

Secondary-Ion Mass Spectrometry (SIMS): Used for depth profiling to determine the distribution of elements (H, O) within the YO film. (Cameca IMS 7f microanalyezer; Oslo Univeristy, Norway)

Temperature-Dependent Conductivity Measurements (TDCm): Conducted to study the electrical properties of the Y/YO films as a function of temperature. (Ecopia 5000; Institute of Solid State Physics, University of Latvia, Latvia)

Large-Scale Research Infrastructure Based Characterizations:

X-ray Absorption Spectroscopy (XAS): Performed at DESY PERTA-III P65 undulator beamline in Hamburg, Germany, to explore the local atomic structure, electronic structure and oxidation states of the elements within the films.

Rutherford Backscattering Spectrometry (RBS) and Time-of-Flight Elastic Recoil Detection Analysis (TOF-E ERDA): Conducted at the Tandem Laboratory in Uppsala, Sweden, to obtain precise elemental composition and depth profiles of the YHO films.

3.2 Thin Film Production Methods

3.2.1 Magnetron Sputtering

Sputtering is a widely used method for thin film deposition that involves the continuous etching of a target material's surface by high-energy ions. This process relies on the ionization of gases, such as argon (Ar^+) and krypton (Kr^+), using an electric field generated by various power sources, including direct current (DC), pulsed direct current (Pulsed DC), radio frequency (RF), and high-power impulse techniques. Each power source characterizes a different sputtering technique. The ejected atoms from the target are then deposited onto a substrate positioned near the target, forming a thin film[80].

The interaction between target atoms and ions during sputtering primarily depends on the mass of the ions and their incident energy, with a minimum threshold energy required for sputtering to occur. This process involves the physical transfer of momentum and kinetic energy between energetic ions and target atoms, independent of the particle's charge. These collisions can be elastic, resulting mainly in reflected particles, or inelastic, which may produce secondary electrons, photons, X-rays, and implanted particles (refer to Figure 3.1 for particle/ion-target interactions). For a detailed discussion on ion-solid interactions and the magnetron sputtering technique, consult[81].

Sputtering yield is a critical parameter, defined as the average number of target atoms ejected per incident ion, serving as a measure of sputtering efficiency. Refer to Equation 3.1.

$$S = \frac{N_s}{I_P} = \alpha \frac{Mm}{(M+m)^2} \frac{E_m}{U_M} \tag{3.1}$$

In this context, S represents the sputtering yield; N_s denotes the number of sputtered atoms, and I_P is the incident particle flux; M is the mass of the target atom; m is the mass of the incoming particle; E_m is the kinetic energy of the ion; U_M is the bonding energy of the target atom. The coefficient α accounts for the angle of incidence.

Another crucial parameter is the sputtering rate, which relates to the sputtering yield. Refer to Equation 3.2

$$\mathrm{R} = \frac{SJ_i}{\rho \frac{\mathcal{M}}{eN_A}} \tag{3.2}$$

In this context, R represents the sputtering rate; S represents the sputtering yield; $\mathcal{M}$ is the molar mass of the target: ρ stands for target density; J_i is ion current, and N_A is the Avogadro's number.

(a)

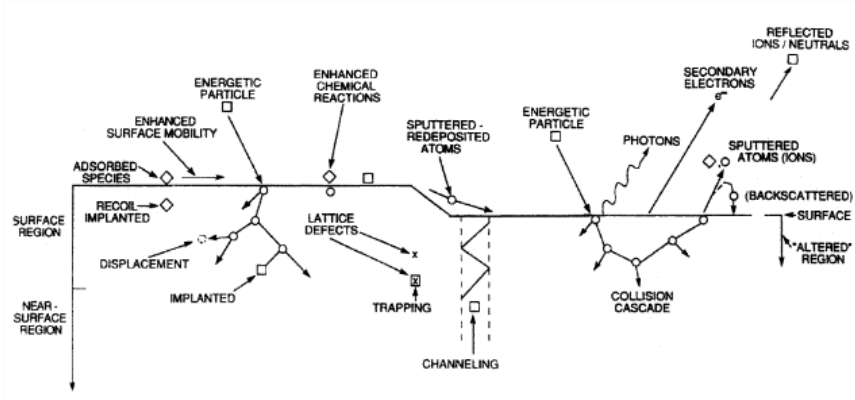

(b)

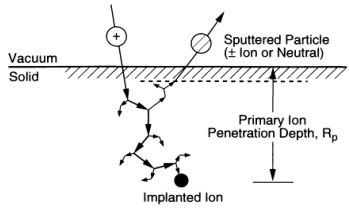

Figure 3-1 | Particle-solid interaction. (a) Detailed kinetics of the interaction process, showing the step-by-step dynamics occurring when particles interact with a solid[81]. (b) The sputtering process illustrates how particles are ejected from the surface of the material due to the impact of incident particles[82].

In magnetron sputtering, magnets positioned beneath the target material create a magnetic field that traps electrons and ions within the generated electric field. This magnetic confinement increases collisions between secondary electrons and ions in the plasma, enhancing ionization and boosting sputtering yield and rate, thereby improving process efficiency. Depending on the design of the system, the magnets used can have various shapes (refer to Figure 3.2).

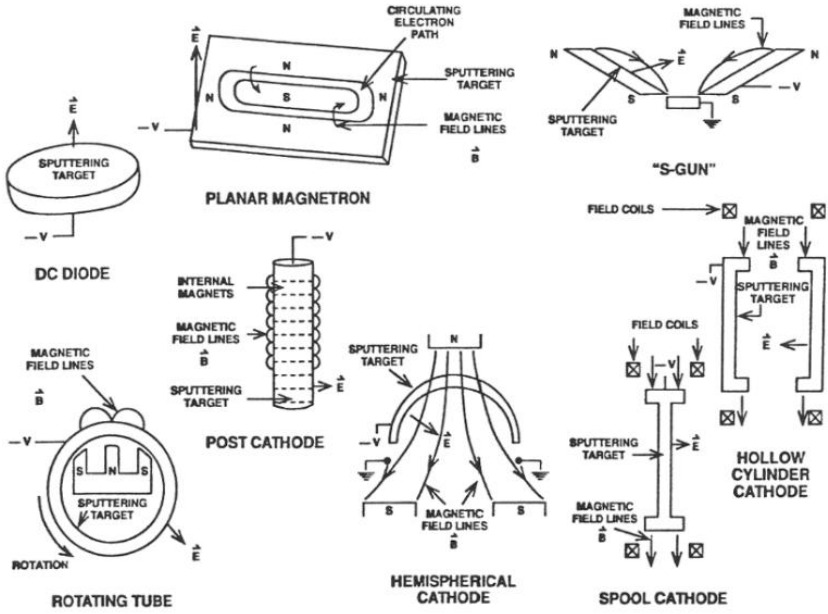

Figure 3-2 | Examples of magnet geometries used in the field[81]. These examples highlight how different magnet shapes and arrangements are utilized for specific applications and experiments.

3.2.2 Electron Beam Evaporation

Evaporation, one of the oldest thin film deposition techniques, involves heating a target material using resistive or electron beam (e-beam) methods until it evaporates. Under high vacuum conditions, the vaporized atoms possessing a kinetic energy of approximately 0.025 eV travel from the target to the substrate and condense to form a thin film[83]. E-beam evaporation is versatile and can be used for a wide range of materials, including metals, metal alloys, and even some low molecular-weight polymers[84].

In the e-beam evaporation technique, a high-energy electron beam is directed at the evaporation source. Electrons are emitted from a heated filament and are guided to the target material using magnetic fields. The electron beam can operate in two configurations: unfocused e-beam evaporation, where the beam covers a broader area, and focused e-beam evaporation, where the beam is concentrated on a smaller spot, as shown in Figure 3.3. Typically, an operating power of around 5 kW is used to accelerate the electrons.

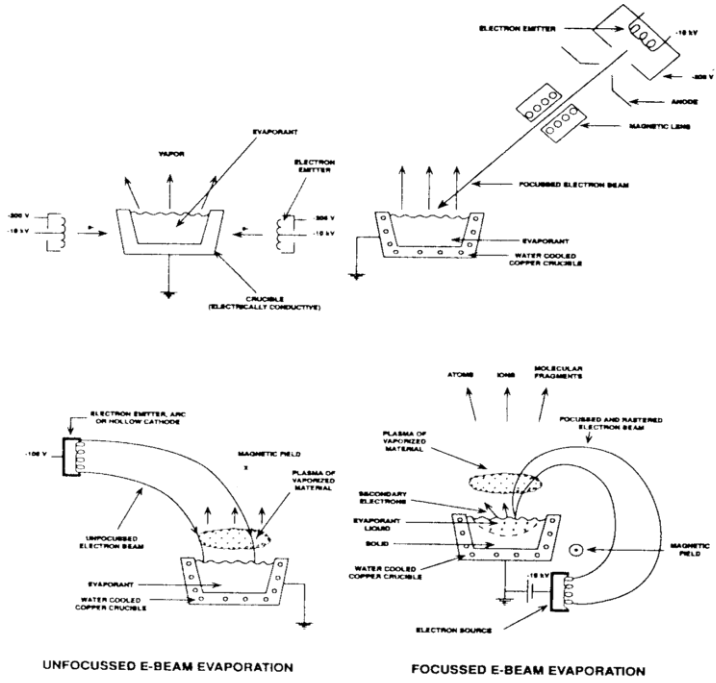

Figure 3-3 | Vaporization sources and geometries in the e-beam evaporation process.[81] The image shows two types of beam configurations: unfocused (left side) and focused (right side)

In unfocused e-beam evaporation (refer to Figure 3.3, left column), the electron beam is dispersed over a larger area, causing some heating of both the crucible and the source material. This occurs because the beam is not tightly concentrated, allowing indirect heat transfer to surrounding components, including the crucible. As a result, this configuration is less efficient at delivering energy to the target material compared to focused e-beam evaporation (refer to Figure 3.3, right column), where the beam is tightly concentrated on the source, minimizing heat transfer to the crucible. This localized heating minimizes the risk of contamination from crucibles or other components, enhancing film purity and quality.

The properties of the deposited film are further influenced by several key factors, including chamber pressure, the distance between the evaporation source and the substrate (which is typically greater than in magnetron sputtering), the mean free path and arrival ratio of the evaporated particles, and the deposition rate. For a detailed discussion on the e-beam evaporation technique, consult[81,84].

3.3 Thin Film Characterization Methods

The classification strategy is as follows: Light-Matter Interactions: This category includes UV-VIS, SE, XAS, XRD, and XPS; Electron-Matter Interactions: SEM, and TEM; Ion-Matter Interactions: Encompassed here are SIMS, RBS, and TOF-E ERDA; Electrical and Thermal Measurements: This section involves TDCm. Within the scope of these characterization methods, the production of electromagnetic radiation, electrons, and ionized particles, as well as the specifics of product detection, will not be discussed in detail.

3.3.1 Ultraviolet-Visible Spectroscopy (UV-Vis)

Ultraviolet-visible (UV-VIS) spectroscopy is an analytical technique that measures the absorption, reflectance, and transmittance of ultraviolet and visible light by a sample[85]. To cover the entire UV-VIS spectrum, the spectrometer typically uses a combination of light sources such as Deuterium lamps for UV light (200-400 nm) and Tungsten-Halogen lamps for visible light (400-750 nm). These measurements reveal important optical characteristics of the material, including how it interacts with light and the presence of specific features or electronic transitions within the sample. The absorbance characteristic is governed by the Beer-Lambert Law[86], as given in equation 3.3.

$$A = \log(\frac{I_0}{I}) = \varepsilon cl, \qquad T = \frac{I}{I_0} \tag{3.3}$$

In this context, A is the Absorbance (dimensionless); I_0, is the incident light intensity; I Transmitted light intensity; ε is the molar absorptivity or extinction coefficient (L $\mathrm{mol}^{-1} cm^{-1}$); c is the concentration of the absorbing species; l is the path length through the sample (cm); and T is the transmittance

Determining the absorption, reflectance, and transmittance allows the calculation of the absorption coefficient of the material of interest (refer to Equation 3.4). By analyzing the spectral distribution of the absorption coefficient, it is possible to determine the light-induced electronic transitions within the material, as well as other optical properties. Refer to Figure 3.12 and Equations 3.4-5.

$$\alpha = \frac{1}{l}\ln\left(\frac{1-R}{T}\right), \qquad \alpha = \frac{2.303A}{l} \tag{3.4}$$

$$(\alpha hv)^n = A\left(hv - E_g\right), \quad E = hv = \frac{hc}{\lambda} \tag{3.5}$$

In this context, E is the photon energy; h is Planck's constant; v is the frequency of light; c is the speed of light in vacuum, λ is the wavelength of light; l is the thickness of the film; R is the reflectance of the film; T is the transmittance of the film; α is absorption coefficient; 2.303 is converts the logarithmic absorbance into a linear absorption coefficient.

UV-VIS spectroscopy fundamentally involves molecular absorption, which is crucial to consider during thin film characterization. Thin films can produce interference patterns in UV-VIS spectra due to multiple reflections of light within the film. This interference can be constructive or destructive, thereby altering the absorption coefficient and the spectrum observed. Refer to Equations 3.6-7.

$$2n_t l\cos\theta = \left(m + \frac{\sigma}{2}\right)\lambda \tag{3.6}$$

$$\alpha_{eff} = \alpha + Interference\ Term \tag{3.7}$$

In this context, n_t represents the refractive index of the thin film; l is the thickness of the film; θ is the angle of incidence of the light; m is an integer representing the order of interference; λ is the wavelength of light; α_{eff} is the effective absorption coefficient; α is the absorption coefficient and σ accounts for the phase shift.

Depending on the experimental setup, different types of detectors are employed, each with its unique characteristics. Photomultiplier Tubes (PMTs) amplify the light signal, enabling the detection of very weak absorption signals. Photodiodes convert light into a current, with the magnitude of the current proportional to the light intensity. Diode Array Detectors (DADs) consist of an array of photodiodes that simultaneously measure light across a range of wavelengths. Charge-coupled devices (CCDs) capture and store

light-induced charge, which is then read out and processed to form the spectral data.

Interested readers are encouraged to explore further details on UV-VIS spectroscopy by consulting the referenced source[87] for in-depth insights.

3.3.2 Spectroscopic Ellipsometry (SE)

Ellipsometry is an optical technique used to measure changes in the polarization of light (electric field component) after it reflects off or transmits through a sample. Its sensitivity to optical properties makes it particularly effective for characterizing thin films and multilayer structures.

The electric field vector $E(z,t)$ for elliptical polarization, as represented in equation 3.12, can be described within the framework of Maxwell's equations[88] outlined in equations 3.8-11.

$$\nabla . E = \frac{\rho}{\varepsilon_O} \tag{3.8}$$

$$\nabla . B = 0 \tag{3.9}$$

$$\nabla \, x \, E = -\frac{\partial B}{\partial t} \tag{3.10}$$

$$\nabla \, x \, B = \, \mu_0 J + \mu_0 \varepsilon_0 \frac{\partial E}{\partial t} \tag{3.11}$$

$$E(z,t) = E_{x0} \, \hat{\mathrm{x}} \cos(kz - \omega t) + \, E_{y0} \, \hat{\mathrm{y}} \cos(kz - \omega t + \boldsymbol{\delta}) \tag{3.12}$$

In this context, ρ is the charge density; ε_O is the permittivity of free space ; J is the current density;μ_0 is the permeability of free space; k is the wave number; ω is the angular frequency; and $\boldsymbol{\delta}$ is the phase difference between the x and components of the electric field (elliptical polarization).

The change in polarization, which describes how electric field propagates through space-time couple, is characterized by two parameters: Psi (Ψ), which represents the amplitude ratio between the p- and s-polarized components of light, and Delta (Δ), which denotes the phase difference between these two components. The Fresnel equations[89] (3.13-17) are used to

calculate the relation between the reflection and transmission coefficients and Psi and Delta.

$$r_s = \frac{n_1 \cos\theta_i - n_2 \cos\theta_t}{n_1 \cos\theta_i + n_2 \cos\theta_t} \tag{3.13}$$

$$r_p = \frac{n_2 \cos\theta_i - n_1 \cos\theta_t}{n_2 \cos\theta_i + n_1 \cos\theta_t} \tag{3.14}$$

$$t_s = \frac{2n_1 \cos\theta_i}{n_1 \cos\theta_i + n_2 \cos\theta_t} \tag{3.15}$$

$$t_p = \frac{2n_1 \cos\theta_i}{n_2 \cos\theta_i + n_1 \cos\theta_t} \tag{3.16}$$

$$\rho = \frac{r_p}{r_s} = \tan(\Psi)\, e^{i\Delta} \tag{3.17}$$

In this context, θ_i is the incident light angle; θ_t is the transmitted light angle n_1 and n_2 are the refractive index of two media for air and the complex refractive index of the medium at the interface; r_p and r_s are the p and s polarized reflection coefficients respectively; t_p and t_s are the p and s polarized transmission coefficients respectively; ρ complex reflectance ratio.

The refractive index (n) and extinction coefficient (k) are critical parameters for characterizing the optical properties of materials. Equation 3.18 relates n to the parameters Psi (Ψ) and Delta (Δ), which are derived from the ellipsometric measurements. Equation 3.19 expresses the extinction coefficient k in terms of Ψ and Δ, allowing for a comprehensive understanding of how light interacts with the material.

$$n = \left(\frac{1 + \tan(\Psi)\cos(\Delta)}{1 - \tan(\Psi)\cos(\Delta)}\right) \tag{3.18}$$

$$k = \frac{1}{2}\left(\frac{(\mathrm{n}^2 + 1)\tan(\Psi)}{1 - \tan^2(\Psi)\cos^2(\Delta)}\right) \tag{3.19}$$

The complex refractive index (ñ, refer to Equation 3.20) combines the refractive index and the extinction coefficient to provide a comprehensive description of how light propagates through and is absorbed by a material.

$$\tilde{n} = n - ik \tag{3.20}$$

It is also possible to derive complex dielectric function (refer to Equation 3.21) by refractive index and extinction coefficient.

$$\tilde{\varepsilon} = \varepsilon_1 + i\varepsilon_2 \qquad \tilde{n} = \sqrt{\tilde{\varepsilon}} \tag{3.21}$$

The complex dielectric function (ε_1, real part; ε_2, imaginary part) introduces or introduced by the Kramers-Kronig relations which are used to validate and interpret experimental data given in equations 3.22-23. For readers interested in more details about optical properties, it is recommended to refer to the following source [90]

$$\varepsilon_1(\omega) = 1 + \frac{2}{\pi} P \int_0^{\infty} \frac{\omega' \varepsilon_2(\omega')}{\omega'^2 - \omega^2} d\omega' \tag{3.22}$$

$$\varepsilon_2(\omega) = -\frac{2\omega}{\pi} P \int_0^{\infty} \frac{\varepsilon_1(w') - 1}{\omega'^2 - \omega^2} d\omega' \tag{3.23}$$

In this context, P stands for the Cauchy principal value of the integral; $\varepsilon_2(\omega)$ is the imaginary part of the complex dielectric function $\tilde{\varepsilon}$; ε_1 is the real part of the complex dielectric function $\tilde{\varepsilon}$; ω is the angular frequency.

There are different types of ellipsometers including null, photometric, and spectroscopic models, each differing in measurement principles, precision, wavelength range, and typical applications. Null ellipsometers achieve high precision by balancing polarization to reach a null condition, typically measuring at a single wavelength, making them ideal for high-precision thin film analysis. Photometric ellipsometer, in contrast, measures variations in intensity with polarization at a single wavelength, offering moderate precision and being commonly used for routine thin film and surface analysis. Spectroscopic ellipsometers provide high precision by analyzing

polarization changes across a broad wavelength range, making them well-suited for detailed material characterization.

Interested readers are encouraged to explore further details on spectroscopic ellipsometry by consulting the referenced sources[91-93] for in-depth insights.

3.3.3 X-ray Absorption Spectroscopy (XAS)

X-ray absorption spectroscopy (XAS) is a synchrotron-based technique used to examine the local environment and electronic structure of a specific atom within a material. The method mainly relies on analyzing the spectral attenuation of X-rays as they pass through/interact with the material, a process that is primarily governed by the Beer-Lambert law[86,94] (refer to Equation 3.24). The absorption coefficient strongly depends[95] on the atomic number of the atom of interest and the energy of the photon (refer to Equation 3.25).

$$\mu(E) = \frac{1}{d}\log(\frac{I_0}{I}) \tag{3.24}$$

$$\mu(E) \approx \frac{\rho Z^4}{AE^3} \tag{3.25}$$

In this context, E represents the energy of the incoming photon; d denotes the thickness of the sample; I_0 is the intensity of the incident light; I is the intensity of the light transmitted through the sample; $\mu(E)$ is the absorption coefficient of the sample; Z stands for the atomic number; ρ refers to the density; A is the atomic mass.

When X-rays with sufficient energy (specific to the element and its corresponding core levels, such as 1s (K), 2s (L_1), and 2p (L_2, L_3)) are directed at a sample, they interact with core electrons, causing their ejection as photoelectrons with energy E_k (refer to Equation 3.26) and leaving behind core holes. These core holes represent an excited state of the atom, which typically has a lifetime on the order of femtoseconds. The primary mechanisms of core hole relaxation are X-ray fluorescence[96] and Auger[97,98] electron emission. Fluorescence occurs when an electron from a higher energy level (outer shell) falls into the core hole. As this transition occurs, the energy difference between the two levels is released in the form of an emitted X-ray photon.

During the Auger process, instead of emitting an X-ray photon, the energy released by the transition of a higher-level electron filling the core hole is transferred to another electron, which is then ejected from the atom. This process competes with fluorescence and is more common in lighter elements.

$$E_k = E - E_0 \tag{3.26}$$

In this context, E_k, E, and E_0 represent the kinetic energy of the photoelectron, the energy of the incoming photon, and the minimum energy required to excite the core electron of the atom of interest (known as the absorption edge). The energies of absorption edges, which correspond to different core electron levels (such as 1s, 2s, 2p, etc.), are distinctive for each element. This uniqueness renders XAS a highly effective technique for characterizing materials.

The ejected photoelectrons, with energy E and wavenumber k, move away from the central atom. In the absence of scattering by other atoms, the photoelectrons are expected to travel freely throughout space. The process of X-ray absorption and photoelectron formation in an isolated atom is illustrated in Figure 3.4a (shown in purple). If another atom is brought nearby, the emitted photoelectron can scatter off the electrons of this atom, as shown in the grey sphere in the same figure. The outgoing and incoming waves at the central atom will create interference, as shown in Figure 3.4b, and this will affect the absorption characteristics of the atom of interest. As a result, oscillations (refer to Figure 3.4c, grey line) will appear in the spectrum in the energy region above the absorption edge. This oscillation, known as Extended X-ray Absorption Fine Structure (EXAFS), provides key information about the distance between the central absorbing atom and the surrounding scatterer atom(s), the number of scatterer atoms at specific distances (coordination number), the type of scatterer atoms, and the static and thermal disorder in the local environment.

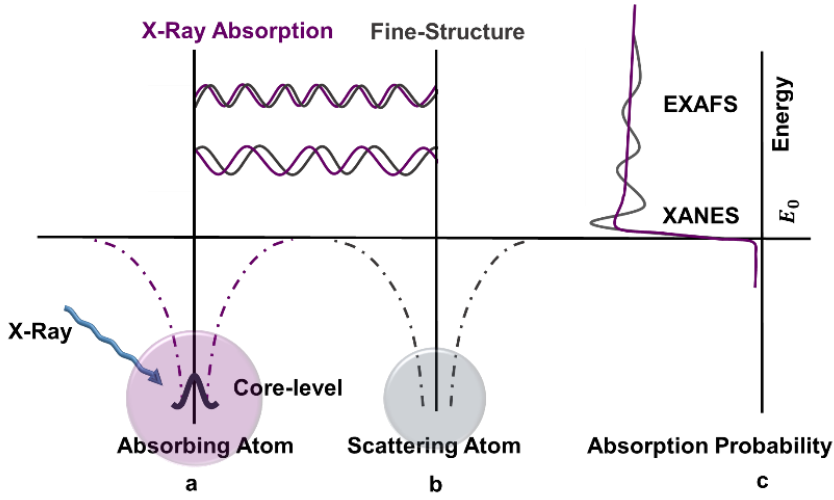

Figure 3-4 | Illustration of X-ray absorption and scattering of photoelectron. When the X-ray energy corresponds to that of a tightly bound core electron level (highlighted atom in purple, (a)), the ejected core-level electron (photoelectron) travels as a wave and backscatters from neighboring atoms (b). The interference between incoming and outgoing waves results in oscillations in the X-ray absorption (c, black line).

This phenomenon can be explained/investigated using Fermi's Golden Rule[99] (refer to Equation 3.27), which describes X-ray absorption as a transition between two distinct quantum states: the initial and final states. In the initial state, the system consists of an X-ray and a core electron, while in the final state, a core hole and a photoelectron are present.

$$\mu(E) \propto |\langle i|\mathcal{H}|f\rangle|^2 \tag{3.27}$$

In this context, $\langle i \mid$ represent the initial state; $\mid f\rangle$ denotes the final state; $\mathcal{H}$ is the Hamiltonian term ($\mathcal{H} = \vec{p}.\hat{\varepsilon}e^{i\vec{k}.\vec{r}}$) governs the interaction.

If we expand the final state into its components we obtain equation 3.28 and we re-construct equation 3.27 we can drive equation 3.29 which represents the absorption kinetics of the atom of interest. In light of the given information, equation 3.29 can be re-defined as equation 3.30.

$$\mid f\rangle = \mid f_0\rangle + \mid \Delta f\rangle \tag{3.28}$$

$$\mu(E) \propto |\langle i|\mathcal{H}|f_0\rangle|^2 \left(1 + |\langle i|\mathcal{H}|\Delta f\rangle| \frac{|\langle f_0|\mathcal{H}|i\rangle|^*}{|\langle i|\mathcal{H}|f_0\rangle|^2} + CC\right) \quad (3.29)$$

$$\mu(E) = \mu_0(E)\big(1 + \chi(E)\big) \quad (3.30)$$

In this context, $\mu_0(E) = |\langle i|\mathcal{H}|f_0\rangle|^2$ is the bare atom absorption and $|\langle i|\mathcal{H}|\Delta f\rangle|$ is the EXAFS oscillation; CC is the complex conjugate

Considering that the final state of the system is represented by the photoelectron's wave function, this approach is justified because the initial state is modeled as a delta function in space. The oscillation part can be written as 3.33

$$\chi(E) \propto \int \psi_{scatt}(r)\delta(r)dr = \psi_{scatt}(r) \quad (3.31)$$

Since the photoelectron propagates in a wave-like manner, creating an interference pattern (as illustrated in Figure 3.4), its behavior is most effectively analyzed by transforming the solution into momentum space. This transformation (equation 3.33) is achieved using equation 3.32

$$\psi(k,r) = \frac{e^{ikr}}{kr} \quad (3.32)$$

$$\chi(k) \propto \psi_{scatt}(k, r = 0) = \frac{e^{ikR}}{kR}\big(2kF(k)e^{i\delta(k)}\big) + CC \quad (3.33)$$

In this context, R is the distance between absorbing and scattering atom; $F(k)$ and $\delta(k)$ neighboring atom(s) related scattering characteristics.

If there is only one scattering atom chi (χ) can be evaluated in Equation 3.34.

$$\chi(k) = \frac{F(k)}{kR^2}\sin\big(2kR + \delta(k)\big) \quad (3.34)$$

Equation 3.34 represents a very simplified situation where only two atoms are involved in the scattering process, which is far from the complexity

of real-world scenarios. In realistic conditions, many atoms participate in the scattering process, necessitating the inclusion of an additional term N in the equation to account for the contributions from multiple atoms (refer to Equation 3.35).

$$\chi(k) = \frac{Ne^{-2k^2\sigma^2}F(k)}{kR^2}\sin\big(2kR + \delta(k)\big) \tag{3.35}$$

In this context, N is the number of the scatterer atoms; σ^2 is the mean square relative displacement between the distance (R) of atoms which represents the thermal and/or static disorder.

Equation 3.35 requires further adjustments to account for the presence of more than one type of scatterer atom. This will involve including a summation term over different types of scatterers in the equation (refer to Equation 3.36). The parameters F(k) and δ(k), introduced in deriving the main EXAFS formula from equation 3.37, represent the scattering amplitude and phase shift, respectively. The scattering of the F(k) typically increases with higher k values for elements with higher atomic numbers (Z), whereas the δ(k) exhibits more pronounced variations for very heavy elements.
The scattering process involves several kinetic factors, including multiple scatterings (MS), where the photoelectron is likely to scatter several times before returning to its original position (In our research, we employ MS theory[99] as the primary approach.) Additionally, inelastic losses can occur, where the excited atom relaxes through the refilling of the core hole, depending on the mean free path of the photoelectron and the lifetime of the core hole. These dynamics necessitate the incorporation of a damping factor into the electron's wavefunction (refer to Equation 3.36)

$$\chi(k) = \sum_j \frac{N_j F_j^{eff}(k)}{kR_j^2}\ \sin\big(2kR_j^2 + \delta_j^{eff}(k)\big)\, e^{-2k^2\sigma_j^2}\, e^{\frac{-2R_j}{\lambda(k)}} \tag{3.36}$$

In this context, j denotes the individual coordination shell of identical atoms located at the same distance from the central atom, $e^{\frac{-2R_j}{\lambda(k)}}$ is the damping factor.

Intrinsic losses, such as the Coulomb interaction between the positively charged core hole and the negatively charged photoelectron, as well as shake-up and shake-off processes that involve the excitation or ejection of

other electrons within the atom, can diminish the observed EXAFS signal (refer to Equation 3.37 (main EXAFS equation[99])).

$$\chi(k) = S_0^2 \sum_j \frac{N_j F_j^{eff}(k)}{kR_j^2} \sin\left(2kR_j^2 + \Phi_j^{eff}(k)\right) e^{-2k^2\sigma_j^2} e^{\frac{-2R_j}{\lambda(k)}} \qquad (3.37)$$

In this context, S_0^2 is the amplitude reduction factor which ranges between 0.7 and 1.0

The EXAFS/XAS signal (grey line) shown in Figure 3.4c can be divided into two main regions: The X-ray Absorption Near Edge Structure (XANES), also referred to as Near-Edge XAFS (NEXAFS), which spans the region around the absorption edge (up to approximately 30-50 eV beyond the edge), and the Extended X-ray Absorption Fine Structure (EXAFS), which extends much further, often thousands of electronvolts beyond the absorption edge. EXAFS provides information about interatomic distances, coordination numbers, type of neighboring atoms, and disorder in the local structure. On the other hand, XANES offers insights into the oxidation state, electronic structure, symmetry, and coordination geometry of the absorbing atom.

If the scattering amplitude F(k), the phase shift, δ(k), and the mean free path, λ(k) are known, it is possible to determine the Interatomic distance R, coordination number N, and disorder parameter σ^2.
Considering this, the main EXAFS equation (refer to Equation 3.37) can be separated into two components: An amplitude term and a phase term. This separation allows for a more detailed analysis of the experimental signal obtained, where the amplitude term provides information about the intensity and damping of the signal, and the phase term gives insights into the oscillatory behavior, which is related to the atomic distances and scattering effects (refer to Equation 3.38).

$$A_j(k) = S_0^2 \frac{N_j F_j^{eff}(k)}{kR_j^2} e^{-2k^2\sigma_j^2} e^{\frac{-2R_j}{\lambda(k)}}$$
$$\phi_j(k) = \sin\left(2kR_j^2 + \Phi_j^{eff}(k)\right) \qquad (3.38)$$

The excited electron can return to the central atom after a single scattering event (refer to Figure 3.5, black arrows), or it can undergo multiple scattering events (refer to Figure 3.5, red and purple arrows).

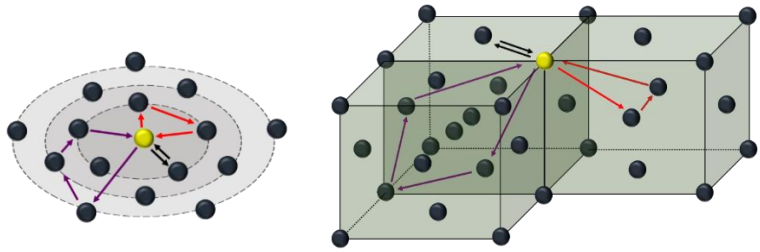

Figure 3-5 | 2D and 3D representations of scattering events for excited electrons and coordination shells. Possible scattering events of excited electrons are shown in both 2D (left side) and 3D (right side) representations. The circles indicate the coordination shells surrounding the absorbing atom. Note that the coordination shells depicted in the left image do not correspond directly to those in the right image; they are illustrated for conceptual purposes only.

In single scattering, the excited electron scatters off a neighboring atom and returns directly to the central atom. The phase and amplitude of the resulting EXAFS oscillations are directly influenced by bond lengths, coordination numbers, and the types of neighboring atoms. Traditional EXAFS spectrum analyses focus on single scattering events.

In contrast, during multiple scattering (MS)[99], the electron can scatter off several atoms before returning to the central atom, leading to additional oscillations in the EXAFS signal. The EXAFS equation (equation 3.37) can be modified considering the MS approximation as a sum of contributions from various scattering paths.

After data collection, the collected data /spectrum undergoes a series of processing steps, including energy calibration, background subtraction, and normalization, to minimize both external (instrumental) effects, and internal (atomic background) effects; and the signal is transferred to momentum space (refer to Equation 3.39). This processing is carried out using various software tools, such as XAESA[100], LARCH[101], and ATHENA[102].

$$\chi(k) = \frac{\mu(k) - \mu_0(k) - \mu_{bkg}(k)}{\mu_0(k)} \tag{3.39}$$

These oscillations, often observed as higher-order peaks in the Fourier-transformed spectrum, correspond to more distant atomic shells. Given that the EXAFS oscillations arise from all interactions, including single and multiple scattering events (refer to Figure 3.5), it is crucial to isolate the signal contributions from single scattering and identify the corresponding coordination shells. To achieve this, a well-characterized reference structure, closely related to the sample of interest, is calculated using the FEFF 8 code[99,103]. This helps in determining the coordination shells responsible for single scattering events.

Subsequently, the signal must be filtered to remove contributions from shells involved in multiple scattering, using Fourier transformation/filtering techniques (refer to Equations 3.40 (Fourier transform)-41(inverse Fourier transform)).

$$ft(R) = \sqrt{\frac{2}{\pi}} \int_{k_{min}}^{k_{max}} \left(\chi(k) k^n Y(k) e^{-i2kR}\right) dk \tag{3.40}$$

$$bft(k) = \sqrt{\frac{2}{\pi}} \int_{R_{min}}^{R_{max}} ft(R)\, e^{i2kR} \left(k^n Y(k)\right)^{-1} dR \tag{3.41}$$

In this context, k_{max}, k_{min}, R_{max}, R_{min} represent the upper and lower limits in momentum and real space, respectively, and $Y(k)$ stands for Window function.

In conventional EXAFS analysis, fitting experimental spectra often requires many adjustable parameters, which can introduce significant uncertainties and correlations between variables. These challenges are amplified when considering distant coordination shells and multiple scattering effects, which are difficult to model accurately using conventional methods as described above.

To address these limitations, scientists have developed simulation-based EXAFS analysis methods. Approaches such as Molecular Dynamics (MD)[104-106], Machine Learning (ML)[107-109], and Reverse Monte Carlo (RMC)[110-114] simulations offer a more robust solution to these issues. In this chapter, a brief description of these methods will be provided.

Molecular Dynamics (MD) simulates atomic motion in materials by solving Newton's equations of motion, generating time-dependent 3D models

under defined conditions like temperature and pressure. MD-EXAFS combines these simulations with EXAFS data to improve structural analysis without the need for experimental data fitting. This approach offers detailed insights into atomic interactions, thermal fluctuations, and structural dynamics. The accuracy of MD results depends on the chosen force-field model, and the method requires significant computational power for large systems.

Machine Learning (ML) methods enhance experimental data analysis by identifying patterns in large datasets, and effectively applying them to both XANES and EXAFS treatment. By establishing relationships between input and output data through training, artificial neural networks (ANN) can quickly predict structural features from EXAFS spectra. Incorporating thermal disorder via classical molecular dynamics (CMD) simulations allows for realistic structural modeling, enabling rapid processing of experimental spectra for in situ and high-throughput studies. However, critical evaluation of results is essential to ensure accuracy.

Reverse Monte Carlo (RMC) is another simulation-based approach that iteratively refines atomic models to match experimental data. Unlike MD, it does not require pre-defined interatomic potentials and provides good structural models for EXAFS data interpretation.

In this research, we employed the Reverse Monte Carlo method combined with the Evolutionary Algorithm (RMC/EA)[115-117]. This approach enhances computational efficiency by simultaneously exploring multiple atomic configurations, facilitating information exchange among them. It enables the analysis of complex scattering paths and distant coordination shells while accommodating significant contributions from multiple scattering. The EvAX code[115] aids in constructing a unified structural model that aligns with experimental EXAFS data across various absorption edges.

RMC/EA initiates with an arbitrary initial atomic configuration, often based on a supercell derived from diffraction studies, and involves random displacements to simulate thermal disorder. Periodic boundary conditions are employed to minimize surface effects. At each iteration, the method calculates the EXAFS signal by comparing the theoretical spectrum, generated using ab initio codes such as FEFF, with the experimental data. This comparison is conducted in both k-space and R-space, utilizing metrics such as the sum of weighted squared differences (ξ) and the Morlet wavelet transform (WT)[118] to enhance accuracy.

The optimization process incorporates the Metropolis algorithm[119], which accepts moves that reduce the difference between the calculated and experimental signals. A temperature parameter (φ) is used to balance exploration and exploitation during the search for a global minimum. A simulated annealing approach may be implemented to dynamically adjust φ, promoting convergence toward the global minimum.

Interested readers are encouraged to explore further details on X-ray absorption spectroscopy by consulting the referenced sources [95,120-122] for in-depth insights.

3.3.4 X-Ray Diffraction (XRD)

X-ray diffraction (XRD) is a powerful non-destructive analytical technique used to study the structural properties of materials. It operates by directing a beam of X-rays at a sample (which can be crystalline and/or amorphous) and analyzing how these X-rays are coherently scattered by the periodic arrangement of atoms in the crystal lattice for crystalline materials. In amorphous materials, while there is no long-range order, some short-range order may still cause diffuse scattering, which does not produce sharp peaks but rather broad features. The intensity and angles of the scattered X-rays depend on the spacing between atomic planes and the incident angle of the X-rays. This phenomenon is governed by Bragg's Law[123], which is expressed by the following equation:

$$n\lambda = 2d \sin\theta \tag{3.42}$$

In this context, n is an integer number and the order of reflection, λ is the wavelength of the incident X-rays, d is the distance between atomic planes in the crystal (interplanar spacing), θ is the angle between the incident X-ray beam and the crystallographic planes.

Due to the arrangement of atoms in a material (regular arrangement in crystals), scattered X-rays can constructively or destructively interfere with each other, depending on the angle of incidence and the spacing between the planes of atoms in the crystal. Bragg's Law describes the conditions under which constructive interference occurs, resulting in a detectable diffraction peak. (refer to Figure 3.6). By measuring the angles (2θ) and intensities of these peaks, it can be inferred the spacing between planes of atoms and other

structural features of the crystal. The scattering efficiency/intensity of X-rays depends on different factors such as the electron density of the related atom; i.e., the more electrons an atom or ion possesses, the higher its scattering efficiency on the corresponding plane (refer to Equations 3.47-50).

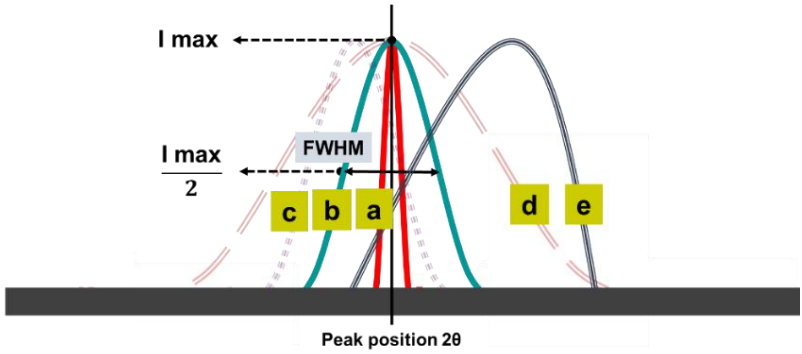

Figure 3-6 | X-ray diffraction peak characteristics. X-ray diffraction peak characteristics: (a) Ideal diffraction peak, (b) standard diffraction peak showing full width at half maximum (FWHM) and I_{max}, (c) symmetric peak shift of the peak in (b), (d) symmetric broadening of the peak in (b), (e) asymmetric peak shift of the peak in (b). The peaks are provided for illustrative purposes only.

In an ideal scenario, XRD peaks are symmetrical and typically resemble Gaussian or Lorentzian shapes. They should be sharp and narrow, with clearly defined separations between peaks (refer to Figure 3.6, a). However, in realistic systems and materials, the peaks often become broader, slightly shift from their original positions, and exhibit asymmetry, as shown in Figure 3.6d, c, and e, respectively. Additionally, the intensity of the observed peaks can vary (Note that this variation is not represented in the corresponding figure).

The observed peak variation/ broadening can originate from various factors, such as grain size, instrumental effects, and stress-strain accumulation (particularly in thin films) within the structure. The peak width/broadening can be quantitatively related to the average crystallite size using the Scherrer equation (refer to Equation 3.43a).

$$\tau = \frac{\lambda\kappa}{\beta\cos\theta} \quad (a) \qquad \varepsilon = \frac{\beta}{2\tan\theta} \quad (b) \tag{3.43}$$

In this context, τ represents crystal size, λ is the wavelength, κ is a constant, β indicates broadening or FWHM, and ε denotes micro-strain.

If the crystal lattice experiences internal or external stress/strain, it can deform like an accordion, which can alter the symmetry and/or position of the detected peaks (refer to equation 3.43). Dislocation density measures the number of dislocation defects within the crystal structure, where atoms are misaligned (refer to Equation 3.44b). Additionally, when peaks from different crystalline phases overlap, it can distort the shape of the peaks and cause shifts in their observed positions.

$$\varepsilon_0^2 = \frac{1}{4\pi}\rho C b^2 In\frac{R_c}{L} \quad (a) \qquad \rho = \frac{k\varepsilon_0^2}{b^2} \quad (b) \tag{3.44}$$

In this context, ρ is the number of dislocations per unit volume. C is a constant related to the material properties or the specific dislocation structure being analyzed. b is the Burgers vector, which represents the magnitude and direction of lattice distortion caused by a dislocation. L denotes the characteristic length, and k is the constant of proportionality.

The intensity of an XRD peak is influenced by several factors, including the structure factor, multiplicity, Lorentz-polarization factor, and temperature factor (refer to Equation 3.45)

$$I(hkl) = |S(hkl)|^2 M_{hkl}\, LP(\theta)\, TF(\theta) \tag{3.45}$$

$$S(hkl) = \sum_j f_j e^{\left(-2\pi\left(hx_j + ky_j + lz_j\right)\right)} \tag{3.46}$$

$$LP(\theta) \propto \frac{(1 + cos^2 2\theta)}{(8sin^2\theta \cos\theta)} \tag{3.47}$$

$$TF(\theta) = e^{\left(-B\left(\sin\frac{\theta}{\lambda}\right)^2\right)} \tag{3.48}$$

In this context, M_{hkl} are the multiplicity factor accounts for the number of equivalent lattice planes that contribute to a diffraction peak in a crystal structure; $S(hkl)$ quantifies how the atomic arrangement in a crystal contributes to the intensity of a diffraction peak; $LP(\theta)$ is the Lorentz-polarization factor, which accounts for the geometry of the diffraction process; $TF(\theta)$ is the temperature factor; B stands for temperature factor; f_j

is the form factor of j^{th} atom; h, k, and l are the Miller indices; $x_j y_j z_j$ Fractional coordinates of the atom j.

Interested readers are encouraged to explore further details on X-ray diffraction by consulting the referenced sources[124,125] for in-depth insights.

3.3.5 X-Ray Photoelectron Spectroscopy (XPS)

When an electromagnetic field interacts with a material, it can participate in several distinct physical processes, including Rayleigh scattering, Compton scattering, the photoelectric effect, and Raman scattering. XPS is a non-destructive technique based on the photoelectric effect, where the energy of photoelectrons ejected from a material is measured (refer to Equation 3.49).

$$KE = h\upsilon - BE \tag{3.49}$$

In this context, $h\upsilon$ is the energy of the incoming photon(soft X-ray); KE is the kinetic energy of the photoelectron; BE is the binding energy of the electron to the core level such as 1s, 2p,3d.

During the X-ray absorption process, both photoelectrons and Auger electrons are emitted, and both types of electrons are detected by the spectrometer. The energy of the photoelectrons depends on the energy of the incoming X-ray photon. In contrast, the energy of the Auger electrons is independent of the incoming photon energy.

To accurately determine the energies of these electrons, it is essential to calibrate the energy scale of the spectrometer considering the Fermi levels of sample and spectrometer (refer to Equation 3.50, and figure 3.7).

$$BE = h\upsilon - KE - \Phi_{spec} - E_{sce} \tag{3.50}$$

In this context, $h\upsilon$ is the energy of the incoming photon; KE is the kinetic energy of the photoelectron; BE is the binding energy of the electron to the core level; Φ_{spec} is the work function of the spectrometer; E_{sce} Surface charge energy.

This calibration fundamentally requires taking into account Fermi-Dirac statistics, which describe how fermions are distributed across energy states in a system at thermal equilibrium (refer to Equation 3.51)

$$F(E) = \frac{1}{e^{\frac{(E-E_F)}{k_B T}} + 1} \tag{3.51}$$

In this conjunction, $F(E)$ is occupation probability of the energy state E; E_F the energy level of Fermi level; k_B denotes Boltzmann constant; T is the absolute temperature.

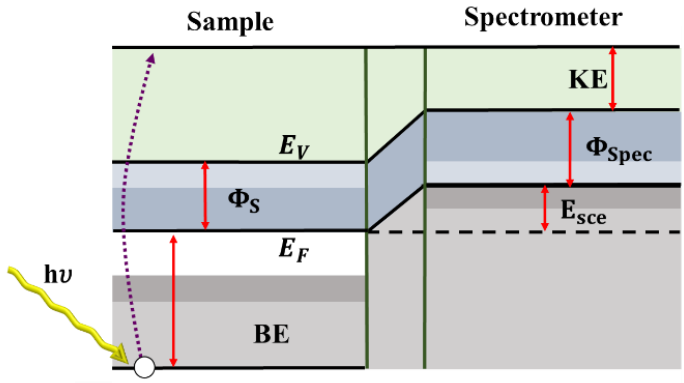

Figure 3-7 | Sample-Spectrometer energy level diagram. In this context, $h\upsilon$ is the energy of incoming photon; KE is the kinetic energy of the photoelectron; BE is the binding energy of the electron; Φ_{spec} is the work function of the spectrometer; E_{sce} surface charge energy. Φ_S is the sample work function.

XPS measures the intensity/counts of photoelectrons as a function of their binding energy, typically spanning from approximately 0 to 1500 eV. This range covers the binding energies of most elements, enabling detailed analysis of their elemental composition. The identification of XPS peaks is related to term symbols (refer to Equation 3.52), as these peaks correspond to the excitation of specific core-level electrons such as O1s, Cu2p, and Y3d. Furthermore, the oxidation state of the atom influences the binding energy of the core electron. For instance, as an atom becomes negatively charged, the interaction between the nucleus and the electrons in the orbital weakens, resulting in a lower binding energy for an individual electron.

$$nQ_j \qquad j = l \mp s \tag{3.52}$$

In this context, n represents the principal quantum number; Q stands for the orbital angular momentum quantum number (0, 1, 2, 3, … corresponding to s, p, d, f orbitals, respectively); s stands for the spin quantum number ($\mp\frac{1}{2}$); the term j=l∓s describes the total angular momentum quantum number, where l is the orbital angular momentum quantum number and s is the spin quantum number

The s, p, d, and f orbitals have different shapes and symmetries that affect the angular distribution of photoelectrons, thereby influencing the shape and separation (in the doublet formation scenario) of the resulting peaks. This characteristic is inherent to the type of orbital and not specific to any particular element.

On the other hand, the intensity of the spectrum depends not only on the sample of interest but also on the characteristics of the spectrometer, including factors like the inelastic mean free path, photoelectric cross-section, and detector efficiency (refer to Equation 3.53[126])

$$I = \lambda\sigma\Lambda\tau\varphi J\epsilon N \tag{3.53}$$

In this context, λ refers to the inelastic mean free path of a photoelectron. σ represents the probability of photoelectron emission from a core level due to X-ray irradiation. Λ denotes the sample surface area. τ is the efficiency of the spectrometer's analyzer in transmitting photoelectrons to the detector. φ relates to the symmetry and angular distribution of the orbital from which the photoelectron is emitted. J indicates the number of X-ray photons incident on the sample per unit time. ϵ is the efficiency with which the detector counts the incoming photoelectrons. N represents the atomic density of the sample, indicating the number of atoms in a given volume.

The intensity of the signal decreases exponentially as it travels through a material due to absorption and scattering processes, making XPS a surface-sensitive technique. The sampling depth is defined as the depth from which 95% of the detected photoelectrons are emitted. This implies that the majority of the photoelectrons measured by the detector originate from within this depth. The sampling depth is closely related to the inelastic mean free path of

the photoelectrons, which is influenced by their kinetic energy and material properties. Typically, the sampling depth is approximately three times the inelastic mean free path (refer to Equation 3.54).

$$I_s = I_0 e^{\frac{-d}{\lambda \cos\theta}} \tag{3.54}$$

In this context, I_s represents the detected intensity after the signal has traveled through a material of thickness d; I_0 denotes the initial intensity of the signal before it enters the material; d is the thickness of the material the signal traverses; λ is the inelastic mean free path; and θ is the angle between the direction of the emitted photoelectrons and the surface normal.

Interested readers are encouraged to explore further details on X-ray photoelectron spectroscopy by consulting the referenced sources[126-129] for in-depth insights.

3.3.6 Scanning Electron Microscopy (SEM)

Scanning electron microscopy (SEM)[130] is a widely used imaging technique that employs a focused beam of electrons, directed by electromagnetic lenses, to systematically scan the surface of a sample using a raster scanning technique, which involves both horizontal and vertical movements to create a grid-like pattern. As the electrons interact with the sample, they produce various signals, including secondary electrons, backscattered electrons, and X-rays. SEM typically collects secondary electrons (SEs) and backscattered electrons (BSEs) simultaneously to create high-resolution images (typically in the nanometer range) of the sample's surface, revealing detailed information about its morphology, topography, and composition. The X-rays generated during this interaction are often used for energy-dispersive X-ray spectroscopy (EDX) to analyze the elemental composition (refer to Figure 3.8)

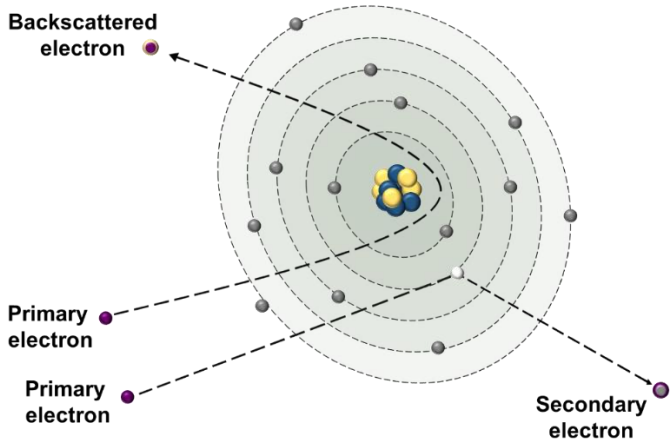

Figure 3-8 | Graphical description of backscattered electron and secondary electron production. Backscattered electrons originate from the incident beam, reflecting off the nucleus of the atom of interest, while secondary electrons are generated when the beam interacts with the electrons of the atom of interest, releasing lower-energy electrons.

Backscattered electrons (BSEs) are high-energy electrons that are elastically scattered back from the sample. The probability of backscattering increases with the atomic number of the material, making BSE images particularly useful for contrasting based on compositional differences. The number of backscattered electrons is influenced by both the number of incident electrons and the atomic number (or the average atomic number if the sample consists of multiple elements), refer to Equation 3.55. Additionally, the number of BSEs that escape from the surface depends on their angle of emission relative to the surface normal.

$$\eta_{bse} = \frac{n_{bse}}{n_0} = PZ^2 \tag{3.55}$$

In this context, η_{bse} represents the backscattering coefficient; n_{bse} is the number of backscattered electrons; n_0 is the number of incoming electrons; P is the proportionality constant; Z stands for the average atomic number of the sample of interest.

In contrast, secondary electrons (SEs) are produced through inelastic scattering interactions between the incoming electrons and weakly bound conduction-band electrons/the electrons in the atomic orbitals of the sample.

These SEs, typically with energies below 50 eV, are highly sensitive to surface features within just a few nanometers. This sensitivity makes SE imaging particularly effective for revealing fine details and surface textures, such as edges, corners, and small features. The secondary electron coefficient can be defined as shown in equation 3.56.

$$\eta_{se} = \frac{n_{se}}{n_0} \tag{3.56}$$

In this context, η_{se} represents the backscattering coefficient; n_{se} is the number of the backscattered electron; n_0 is the number of incoming electrons.

The behavior of electrons exemplifies particle-wave duality, which can be described by the standard de Broglie wavelength[131] equation $\lambda=h/p$, where p is the momentum of the electron. For relativistic electrons, the de Broglie wavelength can be expressed as follows, incorporating the Lorentz factor (refer to Equation 3.57-58).

$$\lambda = \frac{h}{\left(\left(2m_0(m_0C^2(\xi-1))\right)\left(1+\frac{m_0C^2(\xi-1)}{2m_0C^2}\right)\right)^{\frac{1}{2}}} \tag{3.57}$$

$$\xi = \frac{1}{\sqrt{1-\frac{V^2}{C^2}}} \tag{3.58}$$

In this context, λ represents the de Broglie wavelength; h is Planck's constant; m_0 is the rest mass of the electron, C is the speed of light, and ξ denotes the Lorentz factor.

The resolution of SEM is influenced by several factors, including electron wavelength (refer to Equations 3.57-58) and interaction volume. Increasing the accelerating voltage of the electron beam reduces the de Broglie wavelength, which enhances resolution. Additionally, minimizing the interaction volume improves spatial resolution by focusing on surface features rather than deeper material interactions.

Interested readers are encouraged to explore further details on scanning electron microscopy by consulting the referenced source[132] for in-depth insights.

3.3.7 Transmission Electron Microscopy (TEM)

Transmission Electron Microscopy (TEM) involves passing a beam of electrons through an extremely thin sample. As these electrons traverse the sample, they interact with it, producing an image that reflects variations in electron density. TEM offers high-resolution imaging of internal structures, such as lattice planes, defects, and nanoscale features, enabling atomic-scale imaging due to the small wavelength of electrons compared to visible light. As discussed in chapter 3.3.6, electrons exhibit both particle and wave properties, with a de Broglie wavelength (refer to equations 3.57-58).

When accelerated electrons pass the sample they interact with the material. To analyze this interaction, it is accepted electron has plane wave behavior. The total wave function of the electron can be defined as the combination of incident electron wave function and scattered electron wavefunction (refer to Equation 3.59)

$$\psi(r) = \psi_0(r) + \psi_s(r) \qquad \psi_0(r) = e^{ik_0 \cdot r} \tag{3.59}$$

In this context, $\psi(r)$ total wavefunction; $\psi_0(r)$ incident plane wavefunction; $\psi_s(r)$ is the scattered wavefunction; k_0 is the wave vector of the incident electron

Equation 3.59 can be re-written incorporating the potential term (refer to Equation 3.60)

$$\psi(r) = e^{ik_0 \cdot r} + \frac{m_e}{2\pi\hbar^2} \int dr' \frac{e^{ik(r-r')}}{|r-r'|} V(r')\psi(r') \tag{3.60}$$

In this context, m_e, is the electron mass; $\hbar$ is the reduced Planck constant; k is the wave vector of the scattered electron; and $V(r')$ is the potential at the position r'.

If equation 3.60 is modified considering the Born Approximation the scattered wave can be simplified as equation 3.61

$$\psi(r) = e^{ik_0.r} + \frac{m_e}{2\pi\hbar^2}\frac{e^{ikr}}{r}\int dr'\, e^{i(k-k_0).r'}V(r') \tag{3.61}$$

In this context, $e^{i(k-k_0).r'}$ denoted for the Fourier transform of the potential.

The amplitude of the scattering beam is the Fourier transform of the specimen's potential (transformation from position space to momentum space). And if the sample is considered a crystal the potential can be written as in equation 3.62

$$V(r) = \sum_n \sum_\alpha V_\alpha(r - R_n - r_\alpha)S_p(r) \tag{3.62}$$

In this context, R_n and r_α stands for the lattice and atomic positions, respectively; V_α is the potential at an atomic site; and, $S_p(r)$ is the shape factor of the crystal; r is a position vector within the crystal lattice where the potential is being evaluated.

In TEM, the scattering of electrons is analyzed using Fourier transforms, refer to equation 3.63, to move between real space (where the crystal potential V(r) is defined) and reciprocal space (where the diffraction pattern is analyzed). The Dirac delta function is used to represent discrete reciprocal lattice points in the Fourier domain.

$$\begin{aligned} \phi(u) &= \sum_g \delta(u - g)V_g \\ V_g &= \sum_\alpha e^{-2\pi i g.r_\alpha} f_\alpha(g) \end{aligned} \tag{3.63}$$

In this context, $\phi(u)$ stands for the Fourier transform of the crystal potential $V(r)$ in reciprocal space; V_g is the structural factor; and g form factor; u stands for reciprocal lattice vector; δ is used to represent discrete points in reciprocal space where diffraction peaks occur; $f_\alpha(g)$ is the form factor of atoms in the crystal.

The diffraction intensity, which gives information on dark and bright spots in the TEM image, is related to the modulus square of the Fourier transform of the potential (refer to Equation 3.64).

$$|\phi(u)|^2 = \left|\left(\sum_g \delta(u-g)V_g\right).S_p(u)\right|^2 \tag{3.64}$$

In this context, $S_p(u)$ is the shape factor in reciprocal space.

Interested readers are encouraged to explore further details on transmission electron microscopy by consulting the referenced sources[133,134] for in-depth insights.

3.3.8 Ion-Beam Analysis

Ion beam analysis (IBA) techniques are based on analyzing the interaction between an ion beam and a sample to provide depth-resolved elemental composition. Depending on the specific type of interaction between the ion beam and the sample, IBA methods can be categorized into several types, such as Rutherford Backscattering Spectrometry (RBS), Elastic Recoil Detection Analysis (ERDA), Particle-Induced X-ray Emission (PIXE), Nuclear Reaction Analysis (NRA), Secondary Ion Mass Spectrometry (SIMS), Elastic Backscattering Spectroscopy (EBS), Particle Induced γ-Ray Emission Analysis (PIGE). Readers interested in learning more about ion-beam-based methods can find additional details in other sources[135]. A diagram of ion-beam analysis methods is presented in Figure 3.9 [135]. Each method provides distinct advantages for analyzing material composition and structure. In this treatise, SIMS, RBS, and ERDA were employed to examine the elemental composition of thin film structures.

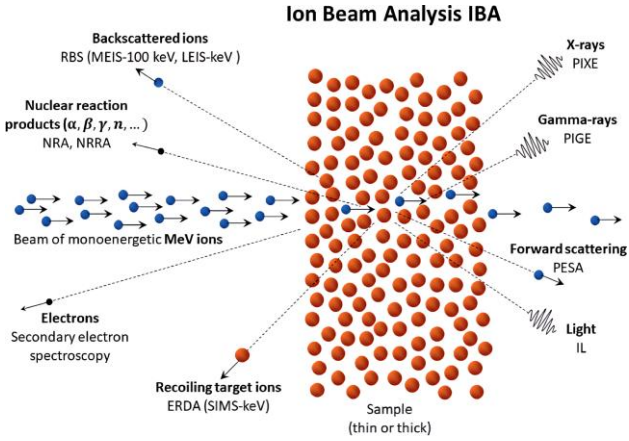

Figure 3-9 | Diagram of detailed ion-beam interaction with matter[135]. This visual representation illustrates the intricate processes of ion-beam analysis and material modification. It shows how ions penetrate the material, leading to various effects such as ionization, atomic displacement, and secondary electron emission.

3.3.8.1 Secondary-Ion Mass Spectrometry (SIMS)

The interaction between the ion beam and the sample of interest takes place through different mechanisms. Those mechanisms are emission, absorption, and reflection/scattering as represented in the figure above. SIMS is a surface and sub-surface analysis method that identifies the elemental composition and impurity elements of a sample by analyzing the mass-to-charge (m/q) ratio as given in equation 3.65 of the emitted particles, including even the lightest elements like hydrogen.

$$\frac{m}{q} = \frac{B^2}{2V} r^2 \tag{3.65}$$

In this context, $\frac{m}{q}$ represents the mass-to-charge ratio (measured in kilograms per coulomb, Kg/C). *B* is the strength of the magnetic field (Wb/m²), *V* is the ion accelerating voltage (V), and r is the radius of curvature of the ion's path in the magnetic field (m).

During the analyses, primary ion beams such as Cs^+, O^{2+}, Ga^+, Ar+, or cluster ions like $C60^+$, with energies ranging from 0.1 to 30 keV, are directed at the sample under an ultra-high vacuum environment, causing the sample's atoms, particles, or clusters to be sputtered away[136]. The effective

depth of the primary particles can vary between 1 to 10 nm depending on the sample of interest. The sputtered atoms can be neutral or charged. The ejected particles, secondary ions, are then detected by a mass analyzer, such as a quadrupole, magnetic sector, double-focusing magnetic sector, or time-of-flight analyzer. The intensity of the secondary ions which is known as SIMS equation[137] is described as follows.

$$I_m = Y\alpha\frac{I_p}{e}\beta C_m \tag{3.66}$$

In This context, I_m is the intensity of secondary ions, representing the measured signal corresponding to a specific element or species; Y is the sputter yield, which is the number of atoms or molecules ejected from the sample per incident primary ion; α is the ionization probability; β is the transmission efficiency of the mass spectrometer, accounting for how efficiently the system detects the ionized particles; e is the elementary charge; C_m is the concentration of element m and I_p is the intensity of the primary ion beam. The term $\frac{I_p}{e}$ converts the primary ion beam current into the number of primary ions striking the sample per unit time.

Various operating modes in SIMS are employed depending on the specific application and the type of information needed. Dynamic mode, also known as time-resolved mode, is used for depth profiling, where the primary ion beam continuously sputters material from the surface, and secondary ions are analyzed to determine the composition of different layers. Static mode focuses on surface analysis with minimal sputtering, utilizing short pulses or low currents to preserve the sample's outermost layers. High mass resolution mode distinguishes ions with similar mass-to-charge ratios by employing mass analyzers with high resolving power. Imaging mode scans the primary ion beam across the sample surface to create detailed maps of secondary ion distribution, providing spatial information about various elements or molecules. Tandem mode involves multiple stages of mass analysis, where secondary ions are first analyzed in one mass analyzer and then further analyzed in a second stage, offering detailed insights into the structure and composition of complex molecules.

Interested readers are encouraged to explore further details on secondary ion mass spectroscopy by consulting the referenced sources[138,139] for in-depth insights.

3.3.8.2 Rutherford Backscattering Spectrometry (RBS)

Rutherford backscattering spectrometry (RBS) is a reflection-based, non-destructive technique that provides depth-resolved elemental composition of the material under investigation. RBS is widely used to analyze the surface composition, layer thickness, and interface of thin films and materials. In RBS, a high-energy ion beam (on the order of MeV, typically helium ions (He^+) or hydrogen ions (H^+)), is directed at the sample. As these ions penetrate the material, they interact with the nuclei of the atoms (refer to Figure 3.9). Some of the ions are elastically scattered back toward a detector positioned at a specific angle, usually between 150° and 170° relative to the incident beam. The choice of scattering angle is crucial as it influences the depth resolution and sensitivity of the analysis. The detector (Silicon Surface Barrier Detector (SSBD)) measures the energy of the backscattered ions, which depends on the mass of the target atoms and the depth at which the scattering occurred. Heavier atoms cause greater energy loss in the backscattered ions, making RBS more sensitive to heavier elements, while lighter atoms result in smaller energy losses.

The process in RBS is governed by Coulombic interactions and follows the equation provided below.

$$V(r) = \frac{Z_1 Z_2 e^2}{r}, \quad \alpha = Z_1 Z_2 e^2 \tag{3.67}$$

In this context, $V(r)$ is the electrostatic potential energy between the two charges as a function of the distance, Z_1 is the atomic number of the incident ion, Z_2 is the atomic number of the target atom, e is the elementary charge, and r distance between the incident ion and the nucleus of the target atom. The scattering process in RBS is conceptually similar to Compton scattering, but instead of photons, it involves high-energy ions interacting with atomic nuclei.

The energy of the backscattered ions is determined by the kinematic factor (refer to Equation 3.68), which characterizes the energy shift based on the masses involved in the scattering process.

$$K = \frac{E_1}{E_0} = \left(\frac{m_1 \cos\theta + \sqrt{m_1^2 - m_2^2 \sin^2\theta}}{m_1 + m_2} \right)^2 \tag{3.68}$$

$$E_0 = \frac{1}{2} m_1 V_0^2 \tag{3.69}$$

$$E_1 = \frac{1}{2} m_1 V_1^2 \tag{3.70}$$

In this context, E_0 is the energy of the incident ion, E_1 is the energy of the scattered ion, m_1 is the mass of the incident ion, m_2 is the mass of the target atom, θ is the scattering angle (the angle between the direction of the incident ion and the direction of the scattered ion), V_0 is the velocity of the incoming ion, V_1 is the velocity of the back-scattered ion

The probability of scattering of the incoming particles given is by equation 3.71. and also known as differential scattering cross-section that gives the probability of scattering into a specific solid angle.

$$\frac{d\sigma}{d\Omega} = \left(\frac{Z_1 Z_2 e^2}{4E_0}\right)^2 \frac{4}{\sin^4\theta} \left(\frac{\cos\theta + \sqrt{\left(1 - \left(\frac{m_2}{m_1}\sin\theta\right)^2\right)}}{\sqrt{\left(1 - \left(\frac{m_2}{m_1}\sin\theta\right)^2\right)}} \right)^2 \tag{3.71}$$

Figure 3.10 illustrates the scattering process graphically. When accelerated ions interact with nuclei, they produce a 3D ring-shaped pattern on an imaginary sphere. The particles that strike the ring within the interval from b to $b+ db$ are scattered at angles ranging from θ to θ+dθ.

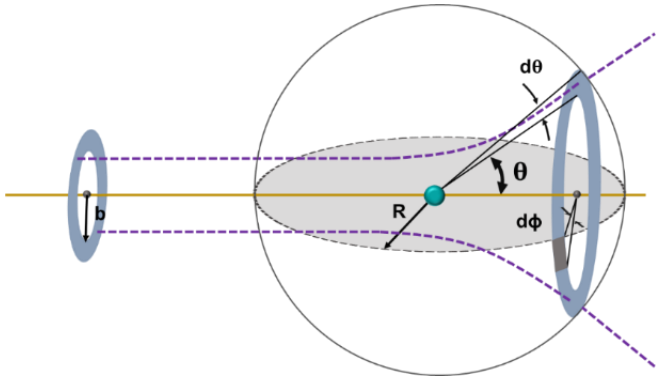

Figure 3-10 | Graphical demonstration of the ion beam scattering geometry. The image illustrates how ions are scattered as they interact with a material. It also shows the angles and paths of scattered ions.

Equation 3.72 represents the solid angle of an infinitesimally small segment of the ring, whereas equation 3.73 describes the solid angle of the entire ring on which the backscattered particles strike. Equation 3.74 on the other hand, stands for the total cross-section of Rutherford scattering, which gives the total probability of scattering into all directions.

$$d\Omega = \sin\theta \, d\theta d\phi = \frac{d\phi R \sin\theta \, R d\theta}{R^2} \tag{3.72}$$

$$d\Omega = 2\pi \sin\phi \, d\theta d\phi \tag{3.73}$$

$$\sigma = \left(\frac{1}{\pi 4\varepsilon_0}\right)^2 \left(\frac{Z^2 e^4}{m_1^2 v^4}\right) \frac{1}{\sin^4(\theta/2)} \tag{3.74}$$

In this context. Z atomic number of the target atom, m_1 denotes the mass of the incoming particle, m_2 refers to the mass target atom, ε_0 is the dielectric constant, *v* indicates the speed of the incoming particle, and θ is the scattering angle.

The number of back-scattered particles (N) per unit time from the target atom into the solid angle (Fig. 3.10) is given by equation 3.75.

$$dN = Nbdbd\Phi = N\sigma(\theta) \sin\theta \, d\theta d\Phi \tag{3.75}$$

RBS not only provides information about the type and concentration of target atoms within a material but also enables the determination of thin film thickness by analyzing the depth-resolved energy distribution of ions scattered back from the sample. As the ions travel through the material to the scattering site/target atom and then out to the detector, they lose energy due to inelastic collisions with the electrons in the material. The energy resolution of the detector plays a crucial role in distinguishing between elements with similar masses and in detecting thin layers. The thickness determination is carried out by equation 3.76 This continuous energy loss, which depends on the depth of penetration, indicates that both elastic and inelastic interactions occur in RBS.

$$t = \frac{\Delta E}{S(E)\cos\varphi}, \qquad S(E) = -\frac{dE}{dx} \tag{3.76}$$

In this context, t is the thickness of the film, ΔE is the energy difference between the backscattered ions from the surface of the film and those from the interface, S(E) is the stopping power of the film material, representing the energy loss per unit path length of the ion as it travels through the material, and ϕ is the angle of incidence of the ion beam relative to the sample surface normal.

Interested readers are encouraged to explore further details on Rutherford backscattering spectrometry by consulting the referenced sources[140,141] for in-depth insights.

3.3.8.3 Elastic Recoil Detection Analysis (ERDA)

Elastic recoil detection analysis (ERDA) is an analytical technique often used as a complementary method to RBS. It is utilized to determine the composition and depth profile of light elements, such as hydrogen (H), deuterium (D), or helium (He), within a material. This method is particularly valuable for thin film analysis due to its high sensitivity and ability to provide precise quantitative information about elemental concentrations. ERDA relies on the elastic recoil of light atoms triggered by high-energy (MeV) incident ions, such as chlorine (Cl), iodine (I), or gold (Au) (refer to Figures 3.9 and 3.11). The technique involves measuring the energy of these recoiled ions. The use of heavy ion beams as incoming particles limits the information depth to a few hundred nanometers, whereas Rutherford Backscattering Spectrometry (RBS) offers an effective depth of around 1 micrometer. The interaction between the ion and the target atom follows similar geometric dynamics in both RBS and ERD (refer to Figure 3.10).

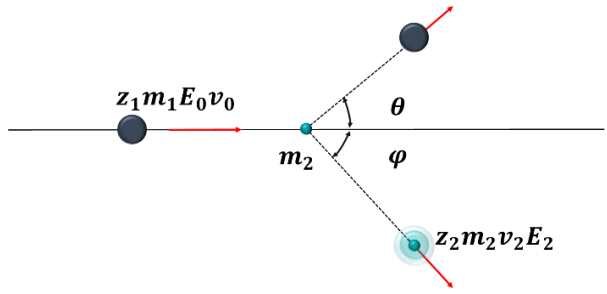

Figure 3-11 | Graphical demonstration of the recoiling geometry. The image illustrates the angles and trajectories of recoiling particles.

In ERDA, a high-energy ion (mass m_1 and initial energy E_0) collides elastically with a target atom (mass m_2) in the material. The target atom recoils, and the energy E_2 of this recoiled atom is measured. The energy of the recoiled atom depends on the kinematic factor K, which determines how much energy is transferred from the incident ion to the target atom (refer to Equation 3.77)

$$K = \frac{E_2}{E_0} = \frac{4m_1 m_2 cos^2\varphi}{(m_1 + m_2)^2} \tag{3.77}$$

The kinematic factor is crucial because it shows that the energy transferred depends on the masses of the incident and target atoms. By measuring the energy of the recoiled atoms and knowing the incident ion's energy and mass, one can determine the mass of the target atoms and their depth distribution within the material. The solid angle, defined in equation 3.73 and graphically demonstrated in figure 3.10, defines the portion of space in which scattered or recoiled particles are detected.

The total cross section is obtained by integrating the differential cross section over the solid angle (refer to Equation 3.78) and provides the overall scattering probability.

$$\sigma = \int_{\Phi_{min}}^{\Phi_{max}} \int_{\theta_{min}}^{\theta_{max}} \frac{d\sigma}{d\Omega} \sin\theta d\theta d\phi \tag{3.78}$$

If $\frac{d\sigma}{d\Omega}$ is substituted by equation 3.70 the total cross section equation evolves into equation 3.80.

$$\frac{d\sigma}{d\Omega} = \left(\frac{Z_2 Z_1 e^2}{2E_0}\right)^2 \left(\frac{\left(\frac{m_2}{m_1}\right)^2}{cos^3\varphi}\right) \tag{3.79}$$

$$\sigma = \frac{\left(Z_1 Z_2 e^2 (m_1 + m_2)\right)^2}{(2m_2 E_0)^2 cos^3\varphi} \tag{3.80}$$

In this context, Z_1 *and* Z_2 are the atomic numbers of the incident ion and target atom, respectively; e is the elementary charge; m_1 is the mass of the

incident ion; m_2 is the mass of the target atom; is the energy of the incident ion; φ is the scattering angle.

Another fundamental metric in ERD is recoil yield which refers to the number of recoiled particles detected per unit of incident ion flux. It provides a quantitative measure of how effectively atoms within the material of interest are ejected and detected. Recoil yield is essential for understanding the distribution and concentration of elements throughout the thin film. The relation of the recoil yield for the thin film is given in equation 3.81

$$\frac{dN(x)}{dx} = \frac{N_o Q d\sigma(E,\phi)}{d\Omega \Delta\Omega} \tag{3.81}$$

In this context, N_o is the initial number of incident ions; Q is a factor related to the quantum efficiency or detection efficiency of the recoil detector; $\frac{d\sigma(E,\phi)}{d\Omega}$ is the differential cross-section, which describes the probability of scattering as a function of energy E, and scattering angle ϕ; $\Delta\Omega$ represents the solid angle over which the recoiled particles are detected

Similar to RBS, ERDA provides depth profiles, but its depth resolution is limited by the stopping power of the recoiled atoms and typically extends to a few hundred nanometers. Depth-resolved energy relation of the process is given by equations 3.82-85.

$$L_{in} = \frac{x}{\cos\alpha} \qquad L_{out} = \frac{x}{\cos\alpha} \qquad L_r = \frac{x}{\cos\beta} \tag{3.82}$$

$$E_0(x) = E_0 - \int_0^{\frac{x}{\cos\alpha}} S(E)dl \tag{3.83}$$

$$E_1(x) = KE_0(x) - \int_0^{\frac{x}{\cos\alpha}} S(E)dl \tag{3.84}$$

$$E_2(x) = K'E_0(x) - \int_0^{\frac{x}{\cos\alpha}} S_r(E)dl \tag{3.85}$$

In this context, $\beta = \pi - \varphi - \alpha$; where α is the angle of incidence relative to the surface normal; L_{in}, L_{out}, L_r represent the incoming path, outgoing path, and recoiled path, respectively; $E_0(x)$, $E_1(x)$, $E_2(x)$ denote the energy of the incident ion just before the collision, the energy of the scattered incident ion

as it exits the target, and the energy of the recoiled target atom, respectively; $S(E)$, $S_r(E)$ are the stopping powers of the incident ion and the recoiled ion, respectively.

ERDA experimental setup includes two primary geometries: a) Transmission Geometry, which is used for thin targets not ideal for depth-resolved analyses; and b) Reflective Geometry, which is ideal for thin films and provides better depth resolution.

In ERDA, all recoiled particles need to be detected, separated, and analyzed, which can complicate interpretation if only a single energy detector is used. This is particularly challenging when particles have similar energies, necessitating the use of multiple detectors simultaneously to ensure accurate analysis.

There are several approaches developed to address this ambiguity in detecting and analyzing recoiled particles. One method involves using a stopping foil in front of the detector. A foil with the appropriate material and thickness is selected to stop undesired recoiled particles. While this approach is effective for detecting light elements such as hydrogen, it is not ideal for obtaining depth-resolution information.

Another approach involves the separation of heavy and light atoms or ions by employing a differential energy (ΔE) detector placed in front of the energy detector. In this setup, ΔE is proportional to the atomic number (Z) of the ions, allowing the detector to separate ions based on their energy loss per unit path length (dE/dx).

Time-of-flight (TOF) based measurements offer another solution, where the time of flight between two points is measured, taking into account that ions with different masses have different kinetic energies. This method enables precise mass separation.

Sophisticated Magnetic Spectrometers (SMS) are often used in conjunction with other detectors in a combined setup. These spectrometers further enhance ion separation and analysis by employing magnetic fields to deflect ions based on their mass-to-charge ratio, providing greater accuracy and resolution in the detection process.

Interested readers are encouraged to explore further details on elastic recoil detection analyses by consulting the referenced sources[142,143] for in-depth insights.

3.3.9 Temperature-Dependent Conductivity Measurements (TDCm)

Temperature-dependent conductivity measurements (TDCm) involve evaluating a material's electrical conductivity across different temperatures. This analysis reveals valuable information about charge carriers, activation energies, and the underlying conduction mechanisms. The band diagram of metals, semiconductors, and insulators is given in Figure 3.12

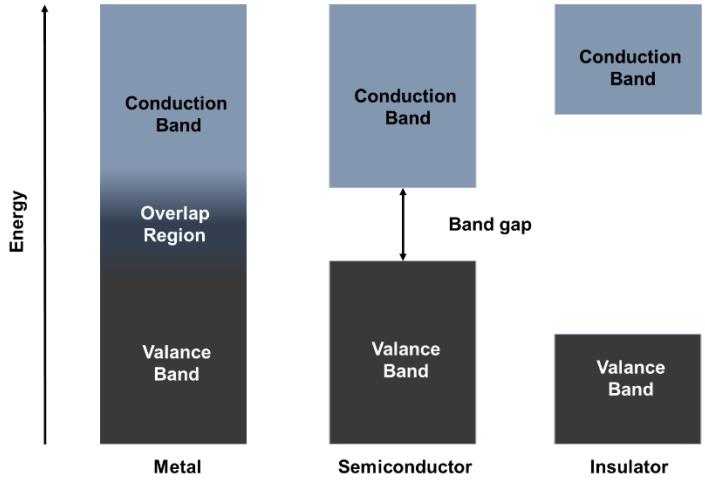

Figure 3-12 | The relative energy levels of occupied and empty bands for metals, semiconductors, and insulators. Metals; The conduction and valence bands overlap or the conduction band is partially filled, allowing free electron movement and electrical conductivity; Semiconductors: A small energy gap between the valence and conduction bands. At absolute zero, the valence band is filled and the conduction band is empty, but thermal energy can excite electrons across the gap, enabling conductivity**;** Insulators: A large energy gap separates the valence and conduction bands, making it difficult for electrons to cross the gap, resulting in very low electrical conductivity.

Metals have a lattice structure composed of positively charged ions (cations) surrounded by a 'sea' of delocalized electrons that are not associated with any particular atom. When an electric field is applied, these free electrons experience a force that causes them to gain kinetic energy, leading to a net drift velocity toward the positive terminal and thereby creating an electric current[144]. Due to frequent scattering (primarily with lattice ions and impurities), the electrons do not continuously accelerate but instead drift with an average velocity in the direction of the applied field. The distribution of

free electrons in a metal can be described by Fermi-Dirac statistics at low temperatures[145] which is given in formula 3.86. At temperatures close to absolute zero, all states below the Fermi level are occupied, and those above are empty. With increasing temperature, electrons can be excited to higher energy states, but the overall number of conduction electrons remains nearly constant because metals have a high density of free electrons. As temperature increases, the metal's lattice ions vibrate more intensely (phonons), causing more collisions between electrons and ions. This scattering reduces the mobility of electrons, thereby increasing resistance and decreasing conductivity.

$$f(E) = \frac{1}{\left(e^{\frac{(E-\mu)}{k_B T}}\right) + 1} \tag{3.86}$$

$$f(E) = A.\, e^{\frac{(\mu - E)}{k_B T}} \tag{3.87}$$

In this context, $f(E)$ is the occupation probability of a state of energy, μ is the chemical potential (Fermi level at absolute zero), k_B is the Boltzmann constant, and T is the temperature.

In semiconductors[146], electrons are initially located in the valence band, with the conduction band remaining empty (intrinsic semiconductors) at absolute zero. The energy gap between these bands is small enough that electrons can be excited by external stimuli such as temperature and light from the valence band to the conduction band. When this happens, electrons leave behind holes (positive charge carriers) in the valence band. Both electrons in the conduction band and holes in the valence band (electron-hole pairs) contribute to electrical conductivity.

While the behavior of charge carriers (electrons/ holes) is generally governed by Fermi-Dirac statistics, in non-degenerate semiconductors at moderate to high temperatures, the electron distribution can often be approximated using a Boltzmann-like formula (refer to Equation 3.87). This approximation is valid because only a small fraction of electrons have enough thermal energy to be excited across the band gap, allowing for a simplified treatment of carrier behavior. As temperature increases, conductivity also rises due to the higher number of thermally excited charge carriers contributing to the conduction process.

The Van der Pauw method[147] is one of the most reliable techniques for measuring the electrical properties of thin films. Various measurement geometries (samples) can be used, with some of the most commonly employed ones illustrated in Figure 3.13.

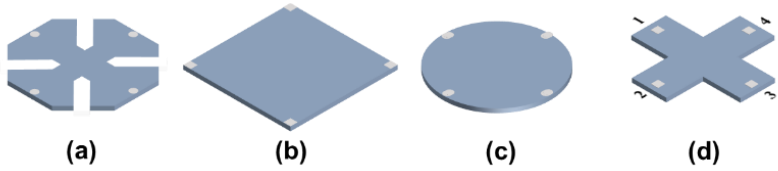

Figure 3-13 | Van der Pauw geometries commonly used for thin film characterization. Listed from right to left, include cloverleaf (a), square (b), circle (c), and cross shapes (d). Brighter spots indicate the ohmic contact between the measurement system and the sample.

The resistivity is calculated by the following formula;

$$\rho = \frac{\pi t}{\ln(2)}(R_s)$$

$$R_S = (R_A + R_B)/2 \tag{3.88}$$

$$R_A = (R_{21,34} + R_{12,34} + R_{43,12} + R_{34,21})/4$$

$$R_B = (R_{32,41} + R_{23,14} + R_{14,23} + R_{41,23})/4$$

In this context, $R_{ij,kl} = \frac{V_{kl}}{I_{ij}}$ with V_{kl} is the voltage measured between contacts k and l ; I_{ij} is the current injected between contacts i and j; and $R_{ij,kl}$ is the related resistance.

Results and Discussions

The research findings are organized into two main sections: yttrium-based single anion (O) system and double anion (O, H) system.

The first section (Chapter 4) focuses on yttrium-based single anion (O) system primarily examining the properties of yttrium monoxide (YO). It explores yttrium oxide thin films deposited under varying oxygen partial pressures, ranging from ultralow to moderate. This chapter provides a foundational analysis of the structural evolution kinetics at room temperature, illustrating the transition from metallic yttrium to fully oxidized states. Additionally, it investigates the physical, chemical, and/or structural properties underlying the solid-state formation of divalent yttrium monoxide (YO) with a 2+ oxidation state at elevated temperatures.

The second section delves into the complexities of double anion system, revealing the interplay between temperature and light-induced kinetics, which leads to unique photochromic properties. This section is divided into three focused chapters (5, 6, and 7), addressing various aspects of YHO's behavior, including atomic-level investigations of thin films, the effect of temperature on the YHO structure, and the structural and chemical transitions between bleached and Photodarkened states.

Chapter 4

4 Yttrium/Yttrium Oxide Thin Films

Metallic yttrium/yttrium oxide thin films were deposited using magnetron sputtering at room temperature under various ultra-low to moderate oxygen partial pressures to investigate the fundamental transition kinetics from metallic yttrium to fully oxidized yttrium oxide (Y_2O_3) thin films. The specific oxygen partial pressure levels and basic growth parameters for all samples are detailed in Table 4.1. This research serves as a preliminary study, with X-ray diffraction (XRD) and optical data collected and presented (see Figure 4.1a and Appendix Figure A1, respectively) as part of this investigation. After determining the optimal oxygen partial pressure at which the material forms a fully amorphous and semi-transparent phase, the focus shifted to high-temperature deposition to explore the conditions that facilitate the formation of divalent yttrium structures. For further experimental and technical details on the sputtering process and characterization methods, please refer to the published article[48].

Table 4-1 | Deposition/evaporation parameters of the Samples. Samples labeled as S_{xx} were produced using magnetron sputtering, while the sample labeled EB_6 was produced via e-beam evaporation.

Sample	P_{O_2} Deposition / Evaporation (Pa)	Growth Temperature (K)	Power (W/cm^2)
S_{11}	~ 2.31 x 10^{-3}	298 ∓5	~7.4
S_{10}	~ 3.97 x 10^{-4}	298 ∓5	
S_9	~ 2.11 x 10^{-4}	298 ∓5	
S_8	~ 1.26 x 10^{-4}	623 ∓5	
S_7	~ 7.60 x 10^{-5}	298 ∓5	
S_6	~ 7.55 x 10^{-5}	623 ∓5	
S_4	~ 4.06 x 10^{-5}	298 ∓5	
S_3	~ 1.37 x 10^{-5}	298 ∓5	
S_2	~ 2.13 x 10^{-6}	298 ∓5	
			Current on e-Gun (mA)
EB_6	~ 10^{-7}	298 ∓5	~43

4.1 Structural Characterization

At room temperature, the deposited films exhibit visible structural transformations (see Figure 4.1a) depending on the oxygen partial pressure levels. During this transition, the oxygen partial pressure can be categorized into two regions based on electrical properties and into three regions based on structural properties.

Between ~ 2 x 10^{-6} and ~ 4 x 10^{-5} Pa pressure levels, the films exhibited metallic-type electrical conductivity, with resistivity increasing as the oxygen partial pressure increased for the samples S_2, S_3, and S_4. At around 7.60 x 10^{-5} Pa and higher, the deposited thin films represent insulating behavior, characteristic of Y_2O_3 (refer to Figure 4.4).

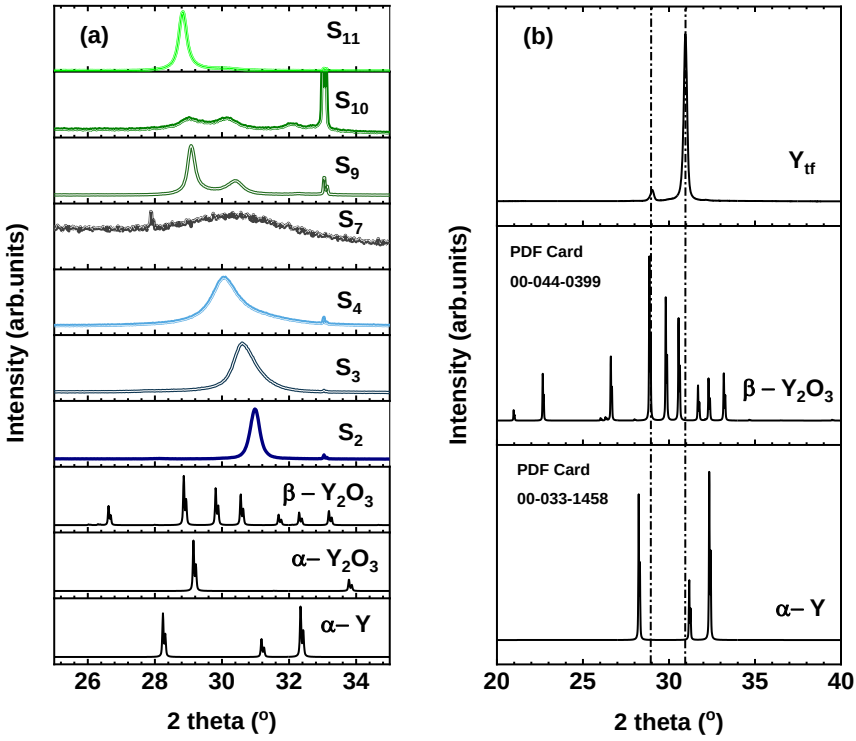

Figure 4-1 | X-ray Diffraction Patterns. a-X-ray diffraction of samples that were deposited at room temperature along with the reference diffractograms from the ICDD database corresponding from α-Y (00-033-1458), α-Y_2O_3 (01-089-5592), β-Y_2O_3 (00-044-0399). b- X-ray diffractogram of sample Y_{tf} with the same reference diffractograms used in a (α-Y_2O_3, and β-Y_2O_3).

The structural transformation exhibits dynamic characteristics (refer to Figure 4.1a), influenced by the presence of α-Y, β-Y_2O_3, α-Y_2O_3 (with some literature referring to the oxide as $Y_2O_{3-\delta}$). The concentration ratio of these structures varies depending on the oxygen partial pressure. At around 7.60 x 10^{-5} Pa, the sample (S_7) represents an X-ray amorphous characteristic. This region, referred to as Region Two (which will later be defined as the partial oxidation region), will be the focus of further investigation.

In region 3, that covers at around 7.60 x 10^{-5} Pa and higher oxygen partial pressure levels. Between ~ 2 x 10^{-4} and ~ 4 x 10^{-4} Pa, the film is postulated to consist of β-Y_2O_3, and α-Y_2O_3. At around 2 x 10^{-3} Pa, the thin film is expected to have pre-dominantly, α-Y_2O_3, however, the peak observed at around 29 degrees is inferred to originate from the simultaneous formation of α, and β-Y_2O_3.

In region 1, the films (S_2, S_3, and S_4) exhibit metallic electrical conductivity, indicating the formation of a metallic phase of yttrium. This is confirmed by the corresponding diffractogram (refer to Figure 4.1a), which shows a peak around 31° α-Y. On the other hand, the shape and position of the observed main peak around 31° vary with increasing oxygen partial pressure levels. The peak shift to lower angles is likely due to the incorporation of oxygen into the host crystal lattice (α-Y) and/or the formation of sub-oxide phases.

A closer analysis of the peak shape reveals that the variation is not symmetric. Additionally, the peak observed around 33° (samples S_2, and S_4) is associated with β-Y_2O_3.

If the incorporation of oxygen into the host crystal structure (α-Y) is regarded as the sole explanation, the discrepancies observed in the diffractograms of samples S_2, S_3, S_4, and S_7 remain unaccounted for, particularly when considering the reference diffractograms provided.

This complexity necessitates additional investigation, prompting the production of another metallic yttrium thin film (Y_{tf}), with the deposition parameters to be detailed in a subsequent article. The diffractogram for this film (refer to Figure 4.1b) suggests that at very low oxygen partial pressures, yttrium crystals form alongside the sub-oxide phase (β-Y_2O_3). Additionally, the XRD measurement of another metallic sample shown in Figure 4.14 (eb_3) corroborates the idea that the sub-oxide phase is β-Y_2O_3. Nevertheless, thermodynamic calculations[148] propose that the sub-oxide phase is α-Y_2O_3 at high temperature.

The variation in peak position observed in samples S_2, S_3, and S_4 is inferred to originate from the formation of the sub-oxide β-Y_2O_3 (if the peak around 33° observed in samples S_2, S_4, S_9, and S_{10} is considered simultaneously). However, the incorporation of oxygen into the host crystal lattice (α-Y) is also a plausible explanation. The relative contributions of these potential phases are still unclear.

A previous study[149] provides a thermodynamic model of the temperature-dependent phase diagram for Y-O systems (refer to Figure 4.2) but lacks specific details for the relevant region.

Current literature indicates a significant gap in comparative studies both experimental and theoretical concerning the characteristics of yttrium in ultralow oxygen environments, the kinetics of sub-oxide phase formation, and the oxygen-dependent structural variations associated with the transition from crystalline metallic yttrium to the insulating amorphous phase. This deficiency in comprehensive empirical and theoretical data hinders the establishment of definitive conclusions regarding these phenomena.

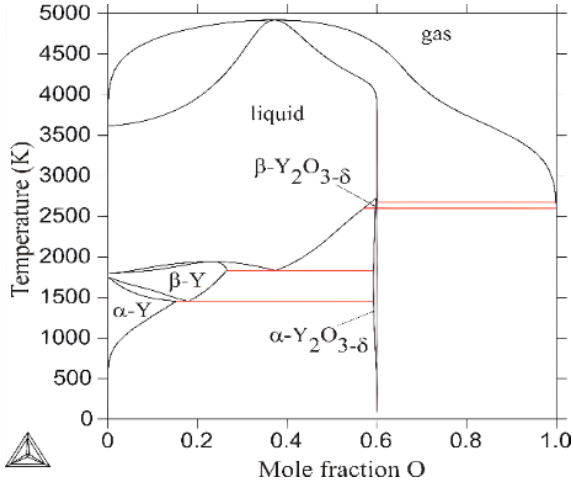

Figure 4-2 | Thermodynamic modeling of the yttrium oxygen system. This image illustrates the thermodynamic modeling of the yttrium oxygen system, highlighting the various stable phases as a function of temperature and oxygen content.

At room temperature, the deposited film in Region 2 exhibits X-ray amorphous characteristics, as previously mentioned. To investigate the effect of temperature on the structure in this region, the experiment was repeated at a higher temperature (~ 623 K) with Sample S_6. Additionally, a fully oxidized yttrium thin film was deposited at high temperatures (Sample S_8). To complete

the analysis and ensure accurate interpretation, another metallic thin film (Sample EB_6) was produced using an electron beam evaporator, chosen for its superior vacuum conditions (refer to Table 4.1). The purpose of producing fully oxidized (S_8), partially oxidized (S_6), and metallic yttrium (EB_6) thin films was to understand the behavior and characteristics of the partially oxidized structure by comparing it with the fully oxidized and metallic forms.

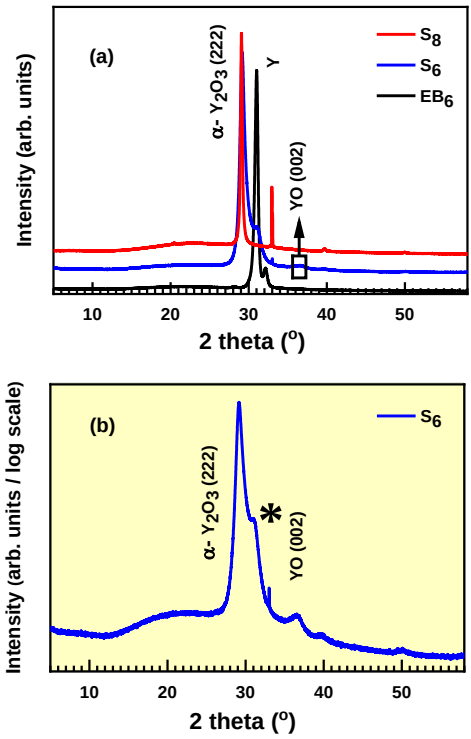

Figure 4-3 | X-ray Diffraction Patterns. X-ray diffraction of samples S_6, S_8, and EB_6 represented in (a). The diffractogram that belongs to S_6 is plotted into the logarithmic scale (b).

The X-ray diffractograms for samples S_6, S_8, and EB_6 are shown in Figure 4.3. Sample S_8, which represents fully oxidized yttrium, and Sample EB_6, which represents metallic yttrium, both display a distinct preferential growth direction, as shown in the figure. Additionally, a peak at approximately 28°, with minimal intensity and just above the noise level, is observed in the diffractogram for EB_6. A peak observed at around 32° may indicate the formation of a different phase, though a definitive conclusion cannot be made.

The diffractogram for S_6 reveals the presence of multiple phases, including both amorphous and crystalline structures, which require further investigation.

The diffractogram (S_6/ blue line) shown in Figure 4.3a, isolated from fully oxidized yttrium and metallic yttrium thin films, has been converted to a logarithmic scale, as depicted in Figure 4.3b. While the crystalline component of the diffractogram is primarily dominated by Y_2O_3, there is also a detectable contribution from YO. The shoulder observed in the same diffractogram, marked with an asterisk (*), could be attributed to YO and/or Y_2O_3. The results of this study are consistent with the literature. Notably, to date, no research has reported a single-phase YO thin film, underscoring the significance of these findings in potentially identifying and characterizing this phase within a mixed-phase system in this study.

In our published article[48], additional scanning electron microscopy (SEM), and transmission electron microscopy (TEM) measurements were conducted, revealing the related phases (both amorphous and crystalline) and the lattice spacing that could be attributed to YO and/or Y_2O_3.

4.2 Electrical Characterization

If sample S_6 contains the YO formation, it should display additional characteristic behaviors, for thin film, as detailed in the literature. To confirm this, temperature-dependent electrical conductivity measurements were carried out (Van der Pauw geometry is square; refer to Fig 3.13b). These measurements were conducted on both YO-containing samples and metallic thin films (S_2, S_3, S_4, EB_6), as shown in Figure 4.4.

Sample S_6 exhibits semiconducting characteristics, aligning with literature that indicates YO displays semiconducting behavior. In 2016, Kaminaga et al.[4] reported the semiconducting behavior of YO. The semiconducting properties of rare-earth monoxides are not restricted to yttrium; similar behavior has also been observed in YbO[150], LuO[151], GdO[152], EuO[153], and TbO[154].

Samples EB_6, S_2, S_3, and S_4 that represent metallic type electrical conductivity. The deposition/evaporation oxygen partial pressure levels of the sample are given in Table 4.1

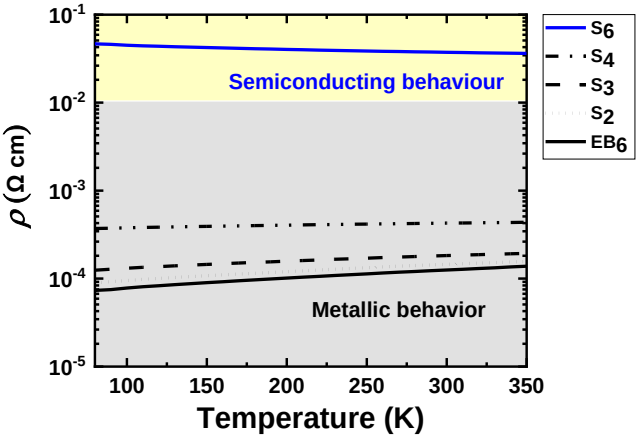

Figure 4-4 | The temperature-dependent electrical resistivity of the samples. Samples S_2, S_3, and S_4, which were prepared by magnetron sputtering, exhibit metallic conductivity. In contrast, sample EB_6, obtained through e-beam evaporation, also shows metallic conductivity. Sample S_6, prepared by magnetron sputtering, displays semiconducting behavior.

4.3 Chemical Characterization

The formation of YO requires the cation to be in a 2+ oxidation state, which warrants further investigation. To explore this, sample S_6 was analyzed using X-ray absorption spectroscopy (XAS), with powder Y_2O_3 (α, Sigma-Aldrich, ≥3N) and Y metal foil (~ 50µm, ≥3N, Standard foil used as a reference at the beamline where the experiments were conducted) used as reference materials to understand and confirm the 2+ oxidation state.

The spectra were recorded at the Y K-edge (17,038 eV) in fluorescence mode at the DESY PETRA-III P65 undulator beamline [155]. Harmonic rejection was achieved with a Rh-coated silicon plane mirror, and a fixed-exit Si (111) double-crystal monochromator was employed. X-ray intensity before the sample was measured using a nitrogen-filled ionization chamber, while the fluorescence signal was collected with a passivated implanted planar silicon (PIPS) detector positioned at 90° to the incident beam. The X-ray absorption near-edge structure (XANES) spectra were extracted from the experimental data using the XAESA code [100].

The results are depicted in Fig. 4.5. While there is a clear distinction in absorption edges between Y_2O_3 and Y metal foil, the difference between Y_2O_3 and sample S_6 (which exhibits the simultaneous formation of YO and Y_2O_3)

is less apparent, (refer to Fig. 4.5a). This complexity may arise from factors such as overlapping features and a broad absorption edge, which can affect the relative concentration ratio of YO and Y_2O_3. It is recommended to refer to article[48] where we demonstrated scanning electron microscopy (SEM) and transmission electron microscopy (TEM) images of the sample, revealing the material's topological complexity and internal characteristics.

To address this ambiguity, the spectrum is magnified around the absorption edge (refer to Figure 4.5b). Although the separation between the spectra is not significant, the results are consistent with those reported in the prior, singular study available in the literature [4].

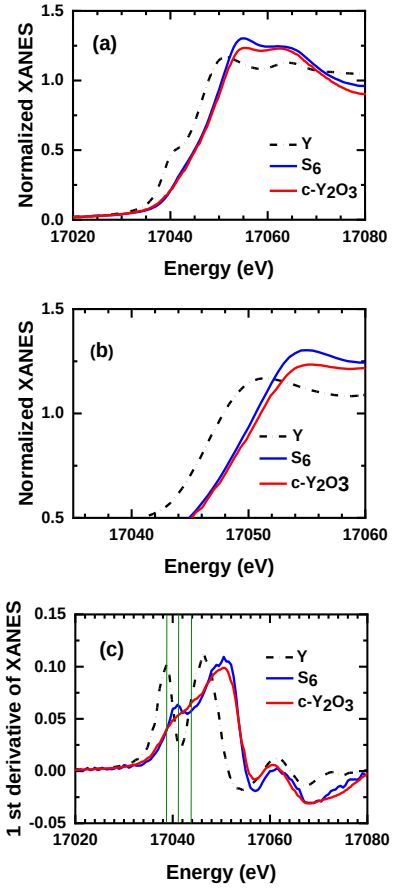

Figure 4-5 | Comparison of XANES spectra. The XANES spectrum of sample S6 (blue line) is compared with that of Y metal foil (black dash-dot line) and α-Y_2O_3 powder (red line). The normalized spectra are shown in panels (a) and (b), while the first derivatives of these spectra are displayed in panel (c).

Additionally, plotting the derivative of the XANES spectrum is a useful method for distinguishing features associated with different oxidation states, as shown in Fig. 4.5c. This figure displays the distinct shapes of the spectra and corresponding edge energies for different samples (Y foil, α-Y_2O_3, and S_6), making it easier to differentiate between them.

Further structural characterization using Extended X-ray Absorption Fine Structure (EXAFS) is impractical due to the material's composition of

multiple phases and the absence of a suitable reference structure for comparison.

Additional chemical characterization of samples S_6 (Y_2O_3 and YO), S_8 (Y_2O_3), and EB_6 (Y) were conducted using X-ray photoelectron spectroscopy (XPS). The spectrometer is calibrated to the Fermi level using silver (Ag) (refer to Figure 4.6). The calibration details are provided in the related article[48].

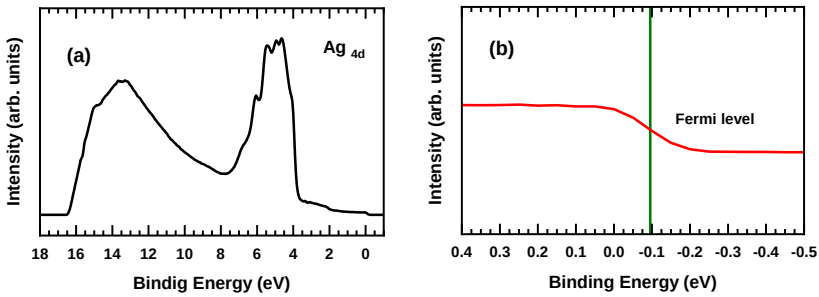

Figure 4-6 | Fermi level calibration of the spectrometer. (a) Ultraviolet Photoelectron Spectroscopy (UPS) measurement of reference sample. (b) Close-up image of the region near the Fermi level.

Extended oxidation state characterization of samples EB_6, S_6, and S_8 was performed employing X-ray photoelectron spectroscopy (XPS, ThermoFisher - ESCALAB Xi), and the spectrums depicted in figure 4.7. The experimental details of measurements can be found in our published article [48].

Figure 4.7a displays the Y_{3d} spectrum of sample S_8. The peak observed around 156.85 eV corresponds to the formation of Y^{3+} ($Y3d_{5/2}$), consistent with the results reported by Nefedov et al. [156]. Additionally, the peak at approximately 155.26 eV likely indicates the presence of Y^0 ($Y3d_{5/2}$) within the same spectrum[157,158] possibly due to the interaction between Ar^+ and the sample. A detailed study by G. Greczynski and L. Hultman[159] on various elements has noted a slight variation in the binding energy levels, which we also observed in the current research for S_8 (Y^0 ($Y3d_{5/2}$)) compared to the literature.

Figure 4.7c presents the Y3d spectrum for sample EB_6, where a peak detected at approximately 155.90 eV indicates the formation of Y^0 ($Y3d_{5/2}$). This finding aligns with the results reported in the earlier study by Mongstad, T. et al.[160].

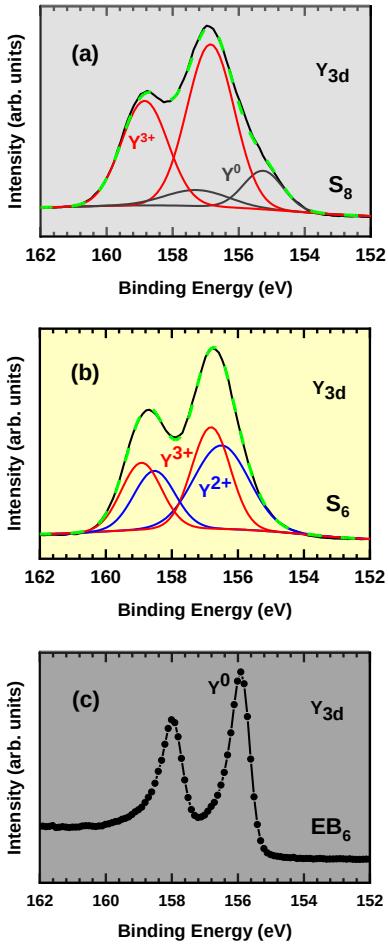

Figure 4-7 | X-ray Photoelectron Spectroscopy (XPS) measurements. (a) insulating (S_8), (b) semiconducting (S_6), and (c) metallic (S_8) behavior. The dashed lines (green) in panels (a) and (b) represent the fitting results of the spectra.

The binding energy of Y⁰ (Y3d) was further verified by measuring a bulk metal cube (≥3N) with dimensions of approximately 1 cm^3 (refer to Figure 4.8). The results from both the metal piece and the thin film were consistent, each corresponding to a binding energy of 155.90 eV.

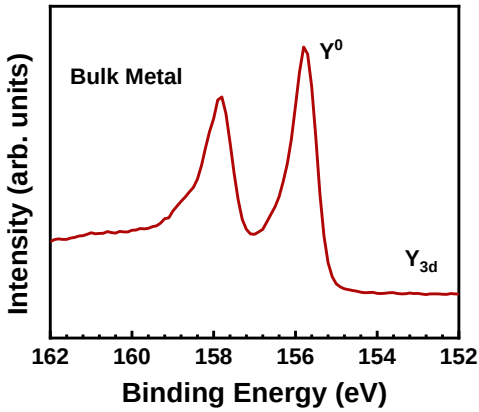

Figure 4-8 | X-ray Photoelectron Spectroscopy (XPS) measurements. Electron binding energy of Y^0. The spectrum is collected from a yttrium metal cube (1 cm^3).

Figure 4.7b illustrates the Y3d spectrum for the sample labeled S_6. The peak detected at 156.49 eV indicates the formation of Y^{2+} ($Y3d_{5/2}$), aligning well with literature values, such as 156.40 eV for YO [4] and 156.50 eV for $YH_{2.1}$[161]. Additionally, within the same spectrum, a peak observed at 156.81 eV corresponds to the formation of Y^{3+} ($Y3d_{5/2}$), consistent with reported values in the literature[156,162]. These observations validate the presence of different oxidation states in the sample, highlighting the spectrum's alignment with previously documented findings.

The calibration of the septum for samples was conducted using the work function method as outlined in [127]. The UPS spectra of these samples (S_6 and S_8) are shown in Figure 4.9. For further details on the calibration process, please refer to[48].

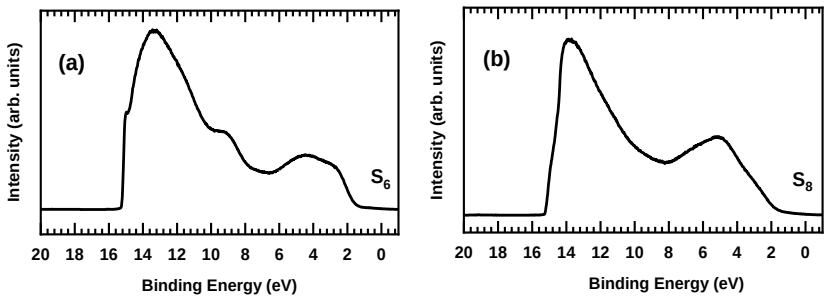

Figure 4-9 | Electronic Structure Analysis. Ultraviolet Photoelectron Spectroscopy (UPS) measurement of the samples S_6 and S_8

Additionally, Secondary Ion Mass Spectrometry (SIMS) measurements were carried out to evaluate the hydrogen content in samples S_6 and S_8, as illustrated in Figure 4.10. The analysis revealed that the concentration of oxygen in both samples was approximately 10^2 times higher than that of hydrogen. This significant disparity in concentration indicates that the amount of hydrogen present is relatively small. Consequently, we can infer that any contribution or contamination from hydrogen in these samples is minimal and unlikely to have a substantial impact on the overall results or properties of the materials.

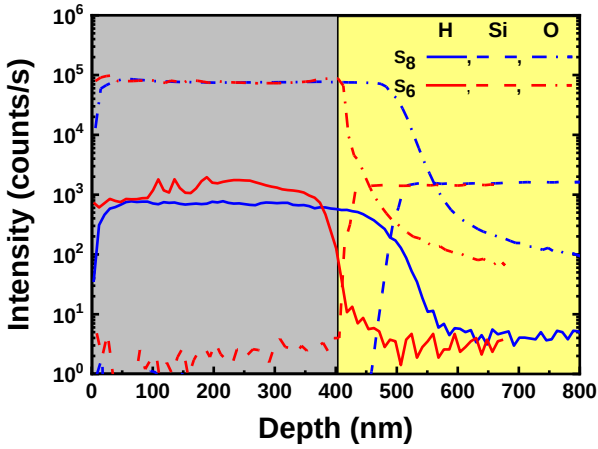

Figure 4-10 | Elemental composition and depth Profiling. Secondary Ion Mass Spectrometry (SIMS) measurements of samples S_6 and S_8.

4.4 Optical Characterization

The spectral distribution of optical characteristics (Ψ and Δ) is a critical method for analyzing and distinguishing the properties of metals (EB_6), semiconductors (S_6), and insulating materials (S_8), as shown in Fig. 4.11.

For the pure Y (EB_6) sample and the sample with a crystalline mixture (S_6), the absence of oscillations in the Ψ (amplitude ratio of the complex reflection coefficient) and Δ (phase difference between the two components of the reflected light) spectra strongly suggests that these materials have a high extinction coefficient (k) (refer to Figure 4.12). A high k value indicates significant light absorption/reflection, leading to low transparency.

Conversely, the S_8 sample exhibits numerous pronounced oscillations in the Ψ and Δ spectra (refer to Figure 4.11), which is characteristic of a material that is largely transparent across the spectral range. These oscillations occur due to interference effects within the film, which are prominent when the material has a low k, indicating minimal absorption/reflection (refer to Figure 4.12b).

However, the gradual decrease in the amplitude of these oscillations above 3 eV (refer to Figure 4.11a) indicates that the material begins to absorb light at higher energies. This behavior is typical for materials that remain transparent at lower photon energies but begin to exhibit absorptive characteristics as the photon energy increases, particularly as it approaches the material's electronic transitions or bandgap energy.

The refractive index n and extinction coefficient k as functions of photon energy are derived from Ψ and Δ, as illustrated in Fig. 4.12. The modeling of n and k was performed using Drude (DO), Gaussian (GO), Tauc-Lorentz oscillator (TLO), and Herzinger-Johs parameterized semiconductor (HJPS) oscillator functions. For more detailed information on the modeling methods, please refer to our published article[48].

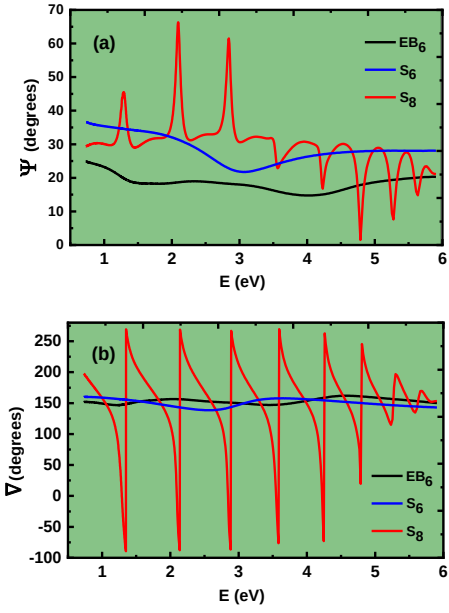

Figure 4-11 | Optical characterization. Main ellipsometric angles Ψ (a) and Δ (b) as a function of photon energy E for samples S_6, S_8, and EB_6.

The n and k curves for EB_6 exhibit typical metallic characteristics: both n and k increase as the photon energy decreases from 3 eV to 0.7 eV, the black curves for in Fig. 4.12. Notably, k remains relatively high (greater than 1) across the spectral range above 3 eV.

Sample S_8 (Y_2O_3) exhibits characteristic dielectric behavior, as shown in Fig. 4.12. With increasing photon energy, n increases more markedly. In contrast, the k also rises with photon energy, but this increase is generally less pronounced than that of n. This difference arises because k is more closely tied to absorption processes. In most dielectric materials, significant absorption begins primarily once the photon energy surpasses the material's bandgap.

The material comprising a mixture of semiconducting YO and dielectric Y_2O_3 phases, shown by the blue curves for S_6 in Fig. 4.12, displays notably lower k values throughout the entire spectral range compared to pure Y. This difference arises because the YO and Y_2O_3 mixture has lower absorption characteristics. YO is a semiconductor with lower absorption in the visible and near-infrared range, while Y_2O_3 is a dielectric material with minimal absorption (Y_2O_3 has a high optical excitation threshold). As a result, the mixed material exhibits reduced k values and thus less overall absorption compared to the high-absorption metal Y.

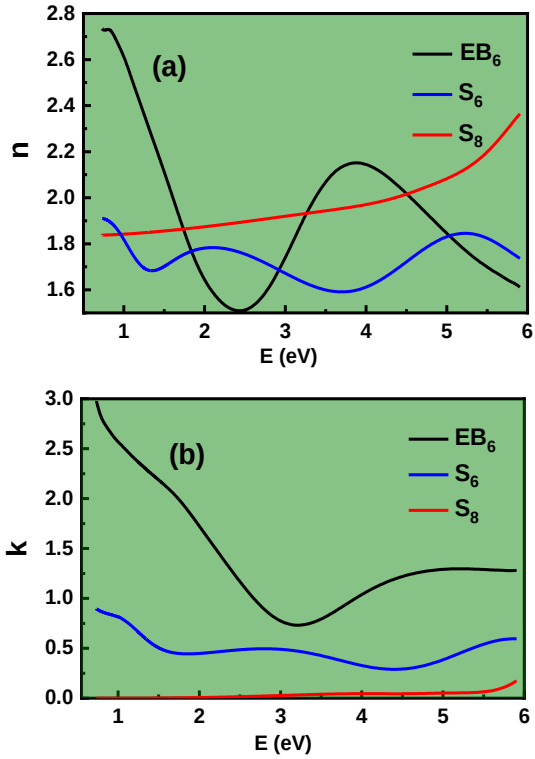

Figure 4-12 | Optical characterizations. Refractive index n and extinction coefficient k as a function of photon energy samples S_6, S_8, and EB_6.

Further characterization was directed toward examining the optical excitation threshold of samples S_6 and S_8. The optical band gap (E_g ~5.86) for sample S_8, obtained from the (HJPS) model, aligns well with literature values [43,163,164]. The observed absorption in the Y_2O_3 structure within the visible spectral range (2 to 4 eV, as shown in Fig. 4.12b) is attributed to variations in the refractive index n and extinction coefficient k throughout the film. These variations can result from inhomogeneities such as porosity, defects, and compositional fluctuations within the film.

For sample S_6, the optical band gap value derived from the Tauc-Lorentz oscillator (TLO) model is (0.30±0.21) eV. This value aligns with the results reported by Kaminaga et al.[4] for YO and Y_2O_3 mixture. Furthermore, the absorbance spectra shown in Fig. 4.13 offer additional confirmation of this finding alongside the transmission measurement.

In the broader context of narrow band-gap semiconductors, several related materials have been documented in the literature. TbO[154], YbO[150], and LuO[151] are all known for their narrow band gaps.

Given that sample S_6 contains both YO and Y_2O_3, it is crucial to consider the volume fraction of each phase. The high volume fraction of YO observed through spectroscopic ellipsometry (SE), details can be found in our published article[48], in sample S_6 suggests a significant presence of an amorphous YO phase. This observation is consistent with findings in the literature, where similar studies have reported the coexistence of monoxide and full oxide phases in related materials. Specifically, references[150,151] document the simultaneous presence of both oxide and monoxide phases in their respective samples.

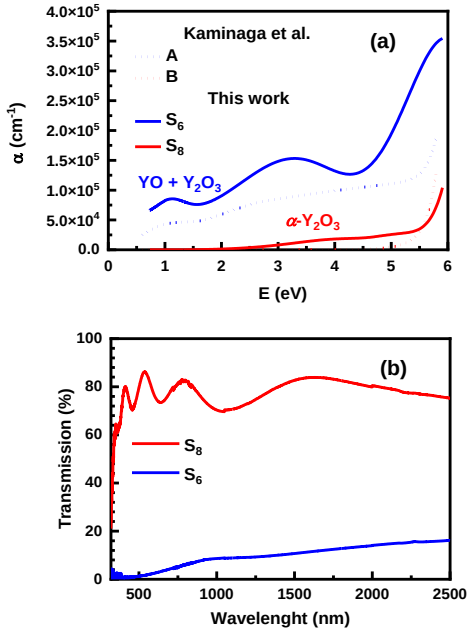

Figure 4-13 | Absorbance and Transmission comparison of the insulating and semi-conducting samples. Absorbance characteristics of samples S_6 (Semi-conducting) and S_8 (Insulating) are shown. (a) The graph compares these results with data from the literature[4], where A represents a crystalline mixture of α-Y_2O_3 and YO, and B corresponds to α-Y_2O_3. (b) Transmission measurements of S_8 and S_6.

The refractive index (n) and extinction coefficient (k) at 550 nm, along with the film thickness (d), surface roughness (S_r), and optical band gap

(E_g) for samples S_6, S_8, and EB_6, are summarized in our published article [48]. For comparison, the optical properties of Y, YO, and Y_2O_3 reported in the literature are also included in the same reference[48].

4.5 Conclusion

This chapter primarily examines the relationship between oxidation dynamics and the structural formation of yttrium oxide thin films. The results corroborate previous studies and add further evidence suggesting that yttrium can adopt a 2+ oxidation state under certain solid-phase conditions.

One key finding from this work is the deposition of yttrium monoxide (YO), achieved from a metallic target using reactive pulsed-DC magnetron sputtering for the first time at high temperatures. Another important outcome is the potential formation of semiconducting yttrium oxide at high temperatures, accompanied by crystalline Y_2O_3. Additionally, this study provides the first evaluation of refractive index (n) dispersion curves for a mixture of YO and Y_2O_3. The analysis reveals that amorphous YO significantly contributes to the (n, k) curves of the mixture.

Under ultralow oxygen partial pressures (~10^{-7} Pa) during thin film deposition, yttrium films predominantly crystallize as hexagonally structured metallic yttrium, concurrently forming sub-oxides. With increasing oxygen partial pressure, oxygen atoms progressively intercalate into the metallic lattice and/or enhance the nucleation of sub-oxide phases. This process induces gradual structural disorder, transitioning the system toward an amorphous state and electrical insulation. Further oxygen incorporation drives the nucleation of crystalline Y_2O_3, culminating in the formation of fully oxidized yttrium oxide at room temperature.

Mechanisms of the Photochromic Effect in Yttrium Oxyhydride Thin Films

Chapters **5**, **6**, and **7** are inextricably linked, each dedicated to unraveling the complex mechanisms underlying the photochromism of YHO thin films. While each chapter focuses on a distinct aspect of the material, together they aim to construct a cohesive and comprehensive thesis. This work elucidates both the atomic and nanoscale structural properties, as well as the photochemical mechanisms driving the photochromic behavior in yttrium oxyhydride (YHO) structures. To enhance understanding of this interconnected research, a diagram is provided below, illustrating the methodologies employed and the specific objectives pursued across these chapters.

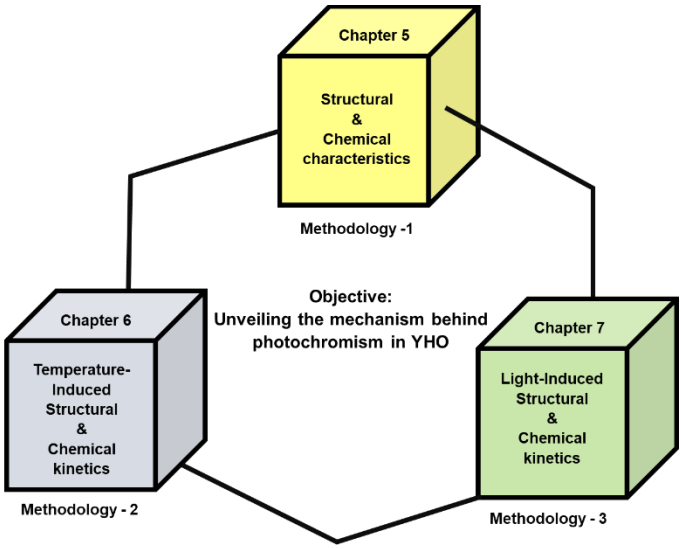

Main Objective | Methodological approaches for analyzing the mechanism of photochromism in Yttrium Oxyhydride (YHO)

Chapter 5

5 Photochromic Yttrium Oxyhydride Thin Films

The thin film samples were produced using a focused e-beam evaporator integrated with a vacuum cluster tool, located in a clean room environment classified as ISO 8. To ensure optimal conditions, the evaporation chamber was baked out for 72 hours at 368 K (± 5 K). Substrate loading and unloading were automated through a robotic arm and load lock, preserving the vacuum integrity within the process/evaporation chamber.

Before evaporation, the substrates underwent sequential cleaning in an ultrasonic bath with acetone, isopropanol, and deionized water (15 minutes each) and were subsequently dried with nitrogen gas. Positioned parallel to each other, the substrates were placed 26 cm from the crucible. The base pressure in the evaporation chamber was reduced to 3.00×10^{-5} Pa.

Thin films of metallic yttrium (eb_3), oxidized yttrium hydride (eb_4), and yttrium oxide (eb_5), each approximately 200 nm thick, were evaporated at 298 K (± 5 K). The metallic thin films were evaporated without reactive gases, while the oxidized and hydride films were produced in either an oxygen or a mixed hydrogen-argon atmosphere (35% H_2) for reactive evaporation. Detailed procedures for the evaporation process and subsequent characterization can be found in our published article[69].

5.1 Structural and Morphological Characterization

The X-ray diffraction patterns of the samples are presented in Fig. 5.1, with comparisons made to the standard JCPDS database. Furthermore, in this context, we referred to a prior investigation conducted[74] regarding high-contrast yttrium-based photochromic oxyhydride powder (obtained the powder by scraping the film that was deposited on the glass substrate).

This powder serves as a comparison/ reference for our discussion in this chapter and belongs to the same family of samples that will be analyzed in Chapters 6 and 7.

Sample eb_3 is primarily composed of the monoclinic phase, with the main peaks observed around $2\theta = 31°$ possibly corresponding to the (002) plane of α-Y and/or the (401) and (40-2) planes of β-yttria. This composition may result from the oxidation of yttrium during evaporation. This observation supports the findings in Chapter 4., where we noted the formation of Y metals

alongside β-yttria. In contrast, sample eb_5, which is fully oxidized, shows an amorphous or nano-crystalline structure, as evidenced by the blue line in the same figure.

Sample eb_4, which has photochromic properties, displayed a single peak around 29° (2θ), indicating a preferred growth orientation of the material. This peak suggests the potential simultaneous formation of cubic phases ((222) of α-yttria) and monoclinic phases ((111) of β-yttria), and/or cubic phases ((111) of YH1.98). Alternatively, it may indicate the exclusive presence of the cubic phase. Furthermore, the peak detected around 29° (2θ) is almost identical in characteristic and position to the peak observed for the powder form of YHO which is produced by magnetron sputtering.

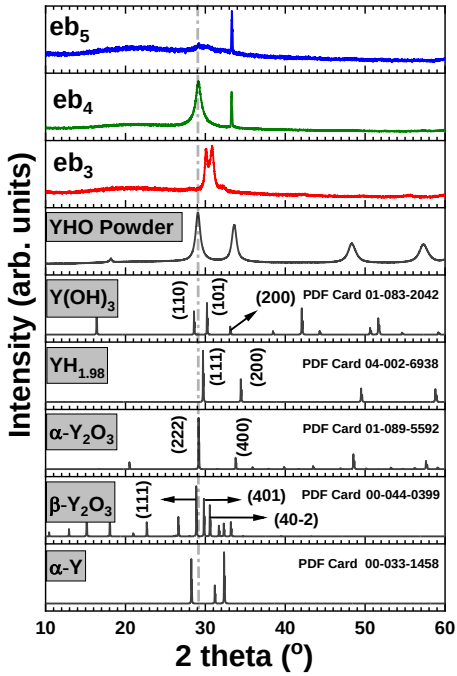

Figure 5-1 | Comparison of XRD Patterns for Yttrium-Based Samples and Reference Phases. XRD patterns of samples, eb_3, eb_4, and eb_5 compared with ICDD reference diffractograms for α-phase Y (hcp), Y_2O_3 (cubic), β-phase Y_2O_3 (monoclinic), YH1.98 (cubic), and $Y(OH)_3$ (hcp). Also included is the diffractogram for high-contrast yttrium-based oxyhydride photochromic powder used as a reference.

We further examined the morphology and structure of sample eb_4 using transmission electron microscopy. The films were analyzed on both glass and silicon substrates to assess any potential substrate-related structural variations at the nanoscale.

The results reveal the morphology of the sample's cross-section, showing the presence of multiple (3) layers, a formation not reported previously. However, a previous study[78] observed hydrogen and oxygen-rich regions using atomic probe tomography for GdHO structures. These findings suggest that similar behavior might be applicable to photochromic YHO structures. From this perspective, our observations could support the conclusions of the referenced study.

This distinctive formation is evident in lamellas extracted from films on both silicon and soda-lime glass substrates. In each case, the middle layer consistently has a thickness of approximately 85 nm. However, there is a noticeable variation of about 20 nm in the thicknesses of the top and bottom layers across different substrates.

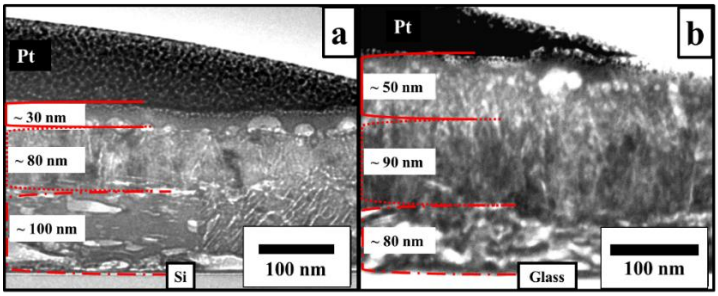

Figure 5-2 | TEM images of extracted lamellas. The image shows the layered structure of the sample extracted from both a silicon substrate (a) and a soda-lime glass substrate (b). The consistent thickness of the individual layers is evident on both substrates.

It is noteworthy that a previous study[165] reported a surface oxide layer thickness of around 8 nm, whereas, in this study, the upper layer measures approximately 30 nm on a silicon substrate and 50 nm on a glass substrate. Furthermore, Komatsu Y. et al. [64] observed the formation of a bi-layer yttrium oxyhydride thin film.

The formation of this unusual multiple layer remains unexplained. However, it likely occurred during the evaporation process and/or as a result of the post-oxidation step.

TEM measurements were performed on the extracted lamellas with dimensions of only a few hundred nanometers. This extraction process (refer to our published article[69]) could have introduced undesired modifications to the sample. Additionally, the sample was transferred from one vacuum environment (Focused Ion Beam chamber) to another (TEM chamber), exposing it to an ambient atmosphere during the transfer, which may have caused further modifications. Therefore, the results obtained from TEM could be artifacts and require further clarification.

To address this, we used X-ray photoelectron spectroscopy, spectroscopic ellipsometry, and ion beam analysis to obtain depth-resolved information.

5.2 Chemical Characterization

Figure 5.3 provides the XPS data for eb_4. The figure clearly shows the formation of a three-layer structure in the oxidized yttrium hydride thin film. Existing literature indicates that this structure often consists of a surface oxide layer, typically described as a two-layer system (see references[68,165]). Depth-resolved XPS analyses for metallic yttrium (eb_3) and yttrium oxide (eb_5) are detailed in our published article[69].

In Figure 5.3a, the depth-resolved spectrum of Y 3d5/2 is shown in three dimensions, illustrating the classification of the three layers into two distinct categories: interface layers and surface layers. Additionally, the corresponding two-dimensional spectrum is provided in Figure 5.3b.

The small peak around 155.8 eV likely indicates the formation of Y^0 [166]. In contrast, the primary peak at approximately 156.4 eV suggests the presence of Y_2O_3 and/or YH_x[167,168]. Additionally, the peak detected around 158 eV probably indicates the simultaneous formation of Y_2O_3, YH_x, or Y-OH, either individually or in combination, potentially in a double or triple fashion [161,167,169].

Figure 5.3c displays the depth-resolved O 1s spectrum in three dimensions, while the corresponding two-dimensional representation is shown in Figure 5.3d. Peaks observed at approximately 527, 529, and 530 eV are likely associated with the formation of O-H, Y-O, and Y-OH, respectively[169-171]. Generally, the peaks in the spectrum fluctuate around specific values due to interactions between Ar^+ ions and the sample and/or depth resolved nano-scale compositional differences. The influence of Ar^+ etching on the binding energy of elements or oxidation states is a well-documented phenomenon[159].

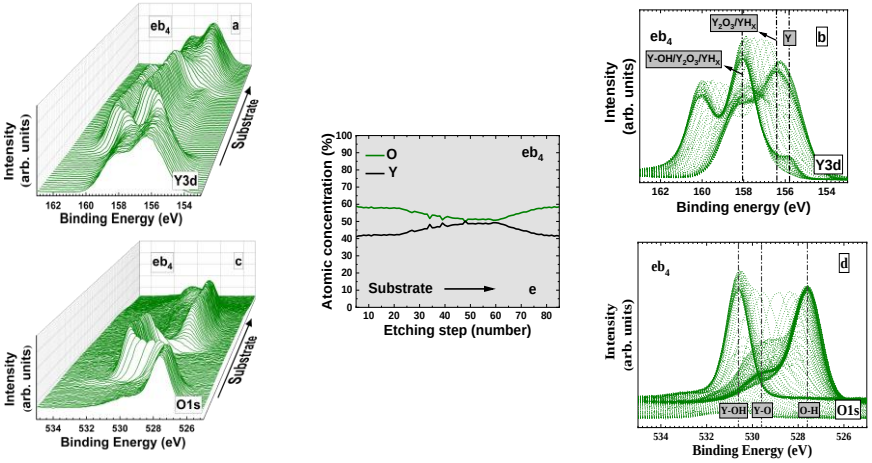

Figure 5-3 | Depth-resolved XPS analyses of sample eb4. (a) depth-resolved Y 3d spectrum dynamic in 3D, (b) corresponding Y 3d binding energy representation/density mapping of the spectrum, (c) depth-resolved O 1s spectrum dynamic in 3D, (d) corresponding O 1s binding energy representation/density mapping of the spectrum, (e) Atomic concentration of yttrium and oxygen depending on depth.

Figure 5.3e shows how the yttrium to oxygen concentration ratio varies with depth for the sample eb_4. The results reveal a decreasing oxygen concentration towards the intermediate layer, where the ratio stabilizes at approximately 1:1 (Y). As depth increases, the oxygen concentration rises again, reaching a balanced ratio of 2:3 (Y). It is important to note that the current analysis may not capture the complete depth profile of the entire film. A standard procedure was applied for binding energy calibration. To better understand the chemical bonding between Y, H, and O (including possible formations such as Y-H, Y-OH, and H-Y-O) and their effects on the XPS spectrum, further investigations are necessary. This includes using alternative binding energy calibration methods as proposed by G. Greczynski and L. Hultman[127].

Additional depth-resolved compositional analyses of sample eb_4 were performed to better understand its formation, oxidation, and hydrogenation dynamics. Ion beam-based techniques (refer to Figure 5.4) identified that, along with the main elements O, H, and Y, the film also contains 1-2 at. % C and trace amounts of F at the promille level.

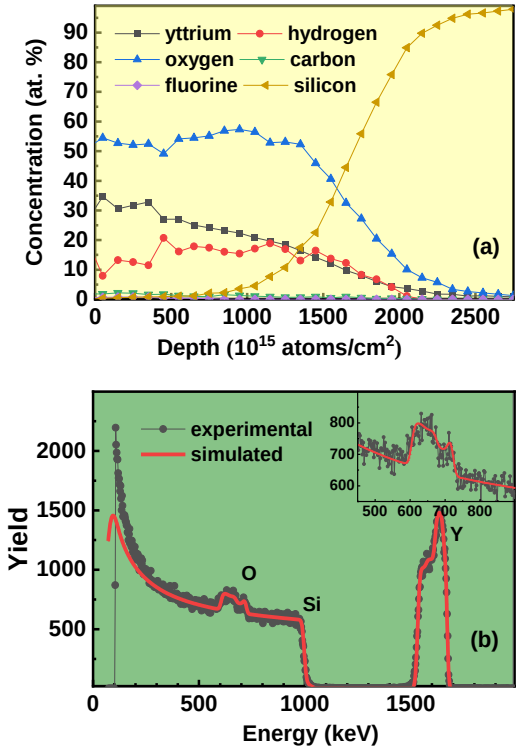

Figure 5-4 | Depth-resolved ion beam analysis of sample eb4. (a) Depth Profile of Chemical Elements from ToF-E ERDA; (b) RBS Spectrum with Fit (Black Dots: Data; Red Line: SIMNRA Fit).

The relative concentration ratios of the primary elements vary with depth, displaying trends consistent with TEM and XPS analyses. The observed differences between XPS and ion beam results are likely due to variations in the effective probing depth of each technique and the specific locations where measurements were conducted.

5.3 Optical Characterization

Spectroscopic ellipsometry, an indirect and nondestructive technique, was employed to investigate the depth-resolved stoichiometric and chemical variations in the photochromic YHO thin film structure (sample eb_4). Similar to our approach with the yttrium-based single anion system (YO) discussed in Chapter 4, we analyzed and compared YHO with metallic and fully oxidized yttrium in this chapter.

The measured and modeled spectroscopic ellipsometry data for samples eb_3, eb_4, and $3b_5$, along with their respective MSE values, are presented in Fig. 5.5. The dispersion curves of the complex refractive index (n, k) as a function of photon energy for the samples are shown in Fig. 5.6. A summary of the thickness, n, k, surface roughness, and Eg values for all samples is provided in our published article[69].

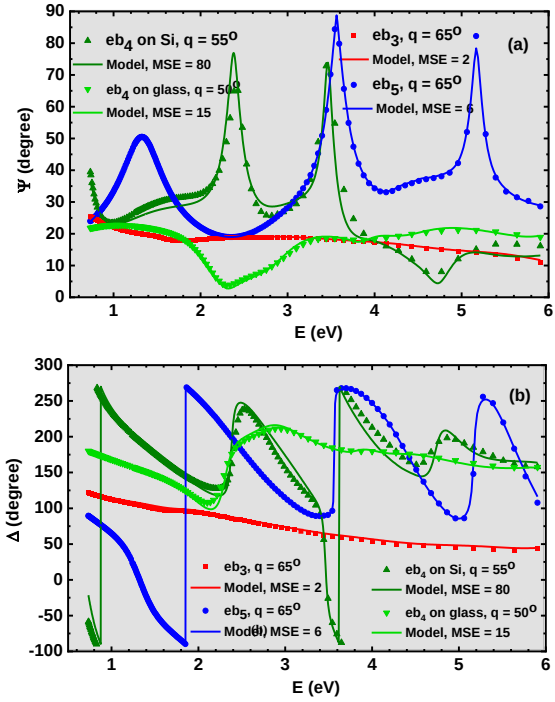

Figure 5-5 | Ellipsometric angles Ψ and Δ vs. photon energy for samples with model fit. (a) Ellipsometric angle Ψ and (b) Ellipsometric angle Δ as a function of photon energy (E) for four samples measured at a specific incident angle. The continuous line represents the model fit, along with the corresponding MSE values.

The refractive index (n) and extinction coefficient (k) values are calculated and shown in Figure 5.6. It is recommended to analyze these results and compare them with the data presented in Figure 4.11.

The n and k values for fully oxidized yttrium thin films exhibit similar behavior in both experiments, regardless of whether the samples were prepared by reactive e-beam evaporation or reactive magnetron sputtering, indicating the optical and/or structural stability of the films. This outcome

aligns with literature expectations, considering that Y_2O_3 is the most stable oxide form of yttrium.

For metallic thin films, the energy-resolved n and k values exhibit a general similarity in spectral distribution characteristics, though noticeable differences in n and k values are observed between films produced by reactive e-beam evaporation and reactive magnetron sputtering. Both methods show an increasing trend in n and k as photon energy decreases, driven by the interaction of free electrons in the metal. The spectral variations are likely due to differing oxygen concentrations/ sub-oxide phase formation in the films, as indicated by the diffractograms in Figures 4.2 and 5.1.

We further analysed the eb_4 thin film samples on both substrates, which exhibit a significant optical gradient (refer to Figure 5.7). The n and k parameters increase from a thickness of approximately 60–100 nm to about 175–220 nm, after which they decrease toward the surface of the films. The high mean squared error (MSE) observed for the eb_4 samples (refer to Figure 5.5) is attributed to the complex inhomogeneities within the YHO films, which cannot be fully captured by the graded effective medium approximation (EMA) model[172]. In this model, the films are considered a multi-layered structure, consistent with the TEM, XPS, and ion-beam results.

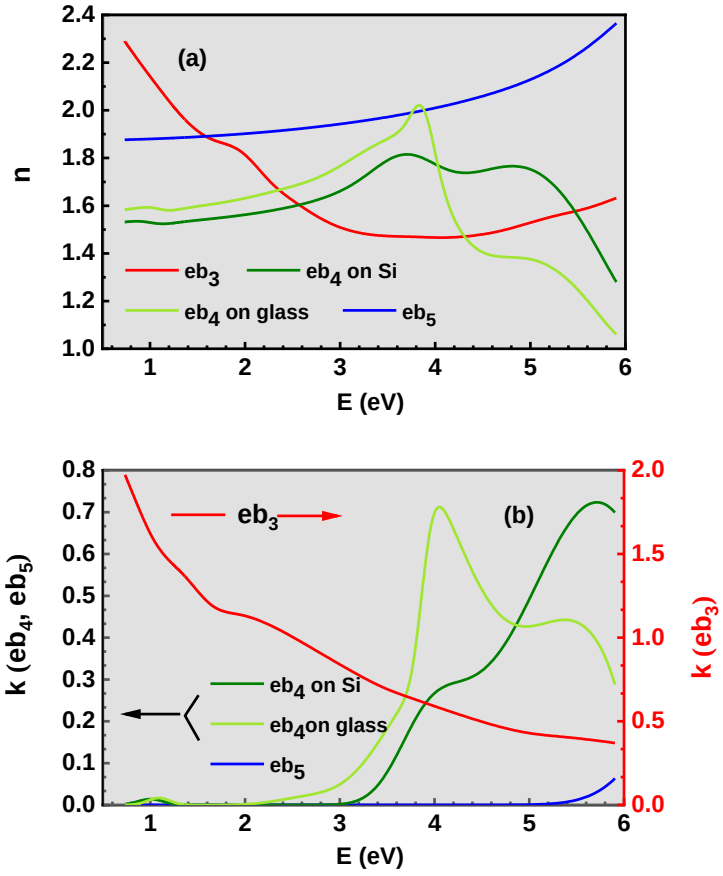

Figure 5-6 | Refractive Index (n) and Extinction Coefficient (k) vs. Photon Energy for Samples. (a) Refractive index (n) and (b) extinction coefficient (k) as functions of photon energy (E) for samples eb_3, eb_4on Si and glass substrates, and eb_5.

Two different models were developed to analyse the multi-layered structure (for more details, please refer to our published article[69]). We will discuss the model with the minimum mean squared error (MSE). In this model, the top YHO layer is represented as an effective medium approximation (EMA) mixture with Y_2O_3, while the middle layer features a gradient EMA mixture of YHO, Y_2O_3, and Y. This model assumes that YHO is the dominant phase in eb_4.

The observed increase in (n; k) toward the middle of the eb_4 sample (refer to Figure 5.7) is associated with the rising EMA volume fraction of Y_2O_3

and Y, as the (n; k) values for Y at 1.67 eV are higher compared to those for YHO. The significant increase in k around 150 nm and 200 nm film thicknesses for eb_4 on glass and Si, respectively, indicates a larger volume fraction of Y.

XPS data also suggest the presence of an interphase layer, likely involving Y metal formation (see Figure 5.7), near the bottom layer of the film (It should be emphasized that the XPS spectrum may not cover the entire thickness of the sample, from the surface of the thin film to the substrate). This observation could be influenced by the effect of Ar^+ etching on the binding energy of the relevant elements or oxidation states, and/or by measurements taken from different areas of the sample with varying inhomogeneities.

Nonetheless, the increase in Y and Y_2O_3 content toward the middle of the film, as obtained from SE, is relatively consistent with the XPS data presented (refer to Figure 5.3). The observations and interpretations from the depth-resolved characterization methods show that the YHO thin film with photochromic properties exhibits stoichiovariants characteristic. Additionally, it is important to note that this is the first study on the YHO structure that identifies regions rich in oxygen and/or hydrogen, as well as three distinguishable layers.

A previous[78] proposed mechanism for photochromism in rare-earth-based oxyhydride systems (such as GdHO, and YHO) based on the formation of multiple phases, including RE_2O_3 and REH_2 (RE: Gd, Y)

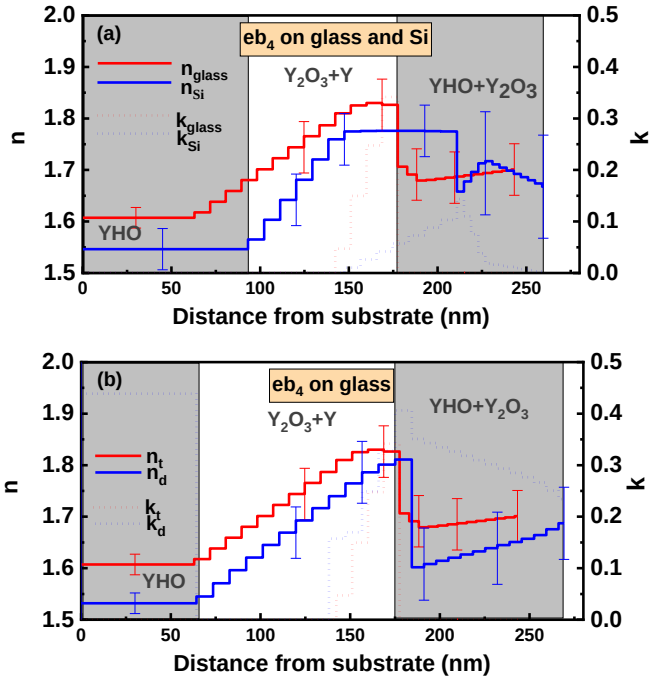

Figure 5-7 | Depth profile of eb4 at 1.67 eV on (a) both substrates and (b) transparent and dark state (glass substrate).

The photochromic effect of the sample eb_4 was further tested. The measurements were conducted on the substrate in both reflection and transmission modes, before and after UV light illumination. The complex dielectric functions (n and k), along with the experimental and modeled transmission spectra in both transparent and dark states, are shown in Figure 5.8. An increase in the extinction coefficient from approximately 3.5 eV to the infrared range is observed in the dark state of the sample for the given light source wavelength and power. This increase in k is also evident in the depth profile of the sample (refer to Figure 5.7b), suggesting significant structural changes in the thin film. The photochromic efficiency of the YHO thin film obtained is significantly higher than those reported in the literature.

The gap energies (Egap) for the three peaks observed in the (n; k) dispersion curves (refer to Figure 5.8a), along with the (n; k) values at 550 nm for both transparent and dark states, are summarized in Table 5.1. In the dark state, the refractive index decreases, the extinction coefficient increases, and the energy gaps for direct electron transitions also decrease. The film appears dark brown in the dark state.

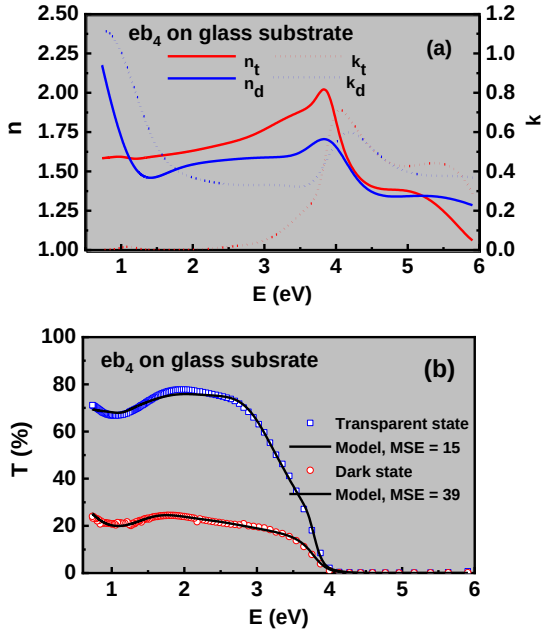

Figure 5-8 | Measured and modeled transmission spectra. (a) and corresponding complex refractive index dispersion curves (b) for $\boldsymbol{eb_4}$ sample on glass in a transparent and dark state.

The potential origin of the spectral variation in the refractive index n (see Figure 5.8) concerning the reported optical excitation thresholds will be explored in detail in Chapter 7. This chapter will provide a comprehensive discussion of how these variations are linked to the underlying mechanisms affecting the optical properties.

Table 5-1 | Optical Properties of sample on different substrates. The electron transition energies E_{gap}, n, and k at 550 nm for thin film on Si and glass substrates.

Substrate	E_{gap}, eV		n		k	
	Transparent	*Dark*	*Transparent*	*Dark*	*Transparent*	*Dark*
Si	3.50 ± 0.20 2.68 ± 0.39 0.56 ± 0.21	-	1.58 ± 0.04	-	0	-
SiO_2	3.48 ± 0.05 1.60 ± 0.40 0.41 ± 0.20	3.15 ± 0.29 1.16 ± 0.33 0.11 ± 0.10	1.66 ± 0.02	1.56 ± 0.04	0.007 ± 0.001	0.35 ±0.02

5.4 Chemical and Structural Characterization

X-ray absorption spectroscopy (XAS) was used for further structural and chemical characterization of the thin films eb_3, eb_4, and eb_5, deposited on Kapton substrates. Each sample was individually sealed in aluminum envelopes inside an Ar atmosphere glove box. For sample eb_3 (metallic thin film), measurements were conducted through the Al packing. In contrast, samples eb_4 (oxidized yttrium hydride thin film) and eb_5 (fully oxidized yttrium oxide thin film) were measured immediately after unpacking. Additionally, X-ray absorption spectra of three reference samples yttrium foil, bulk cubic yttrium oxide (c-Y_2O_3) powder, and photochromic yttrium oxyhydride (YHO) powder were recorded in transmission mode. Experimental details are available in reference[69]. The analysis followed the standard procedure of XAS and was divided into two parts.

The first part focused on the region up to around the absorption edge, known as the X-ray Absorption Near Edge Structure (XANES) region. In this region, the oxidation state of the cation in each sample, including references, was examined.

Figure 5.9 presents the experimental spectra and their first derivatives for samples and three reference compounds. The Y K-edge XANES spectra are dominated by the dipole-allowed 1s(Y)→np(Y) transitions. The first maximum of the XANES derivative, corresponding to the absorption edge, is located at 17038 eV for the yttrium foil (refer to Table A1 for the core level electron binging energies of Y). For the metallic yttrium thin film (eb_3), the edge is slightly shifted to 17039 eV, suggesting partial oxidation, consistent with findings from previous characterization methods such as XPS, XRD, and SE.

The absorption edge for the yttrium oxide thin film (eb_5) and bulk c-Y_2O_3 is observed at approximately 17041 eV, indicating complete oxidation of yttrium ions (3+). The corresponding XPS spectrum confirms the material's identity as Y_2O_3, with the expected elemental composition.

The edge position for YHO powder and the oxidized yttrium hydride thin film (eb_4) is approximately 17040.5 eV, which is 2.5 eV higher than that of the yttrium foil and 0.5 eV lower than bulk c-Y_2O_3. This suggests an approximate yttrium oxidation state of 2.5+.

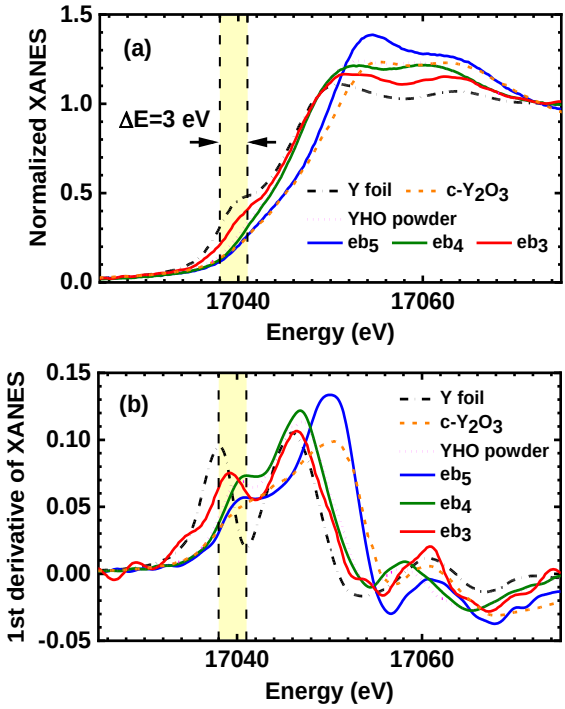

Figure 5-9 | Y K-Edge XANES Spectra and Derivatives. Normalized Y K-edge XANES spectra (a) and their first derivatives (b) for thin films eb_3, eb_4, and eb_5, compared with reference compounds (yttrium foil, bulk c-Y_2O_3, and YHO powder). Dashed vertical lines mark the absorption edge positions for the reference materials.

The second part of the study focuses on analysing and comparing the local structure of the cation in both the samples and reference materials. This analysis examines the oscillatory component of the X-ray Absorption Spectroscopy (XAS) spectrum, known as Extended X-ray Absorption Fine Structure (EXAFS) (refer to Figure 3.4c).

The Y K-edge EXAFS spectra $\chi(k)k^2$ and their Fourier transforms (FTs) are displayed in Fig. 5.11a-b. The EXAFS spectra and FTs for the yttrium foil and the metallic yttrium thin film (eb_3) are nearly identical. This similarity suggests that the local structure of the predominant cation in the thin film does not include anionic contributions (such as oxygen or other anionic contaminants).

The EXAFS spectra of the yttrium oxide eb_5 film and bulk c-Y_2O_3 exhibit some similarities; however, the FTs for the eb_5 film show reduced peak

amplitudes, indicating disorder and a nanocrystalline structure within the film[19,173]. This observation/interpretation is consistent with the XRD results, as shown in Figure 5.1.

It is important to note that the peak positions in the FTs differ from crystallographic values due to phase shifts inherent in EXAFS.

The EXAFS spectrum and FT for the oxidized yttrium hydride film (eb_4) closely resemble those of YHO powder. The peak positions corresponding to the first coordination shell (average distance between cation and anion) and the second coordination shell (average distance between cation and cation) are nearly identical. On the other hand, the amplitudes of the peaks for sample eb_4 and the powder, which reflect the density or number of anions in the region of interest, exhibit some variation.

Current literature (e.g., Reference[74]) does not specify the exact number and/or interstitial positions of the anions in photochromic YHO structures. This phenomenon will be discussed in chapter 6.

The local structural analysis of the photochromic YHO sample (eb_4) and the Y_2O_3 sample (eb_5) was further explored using reverse Monte Carlo simulations (refer to our published article[69] for details). This comparative study was conducted because Y_2O_3 is a well-known material with extensive X-ray Absorption Spectroscopy (XAS) data available[173].

In bulk cubic Y_2O_3 with the space group Ia-3, there are two structurally distinct yttrium sites located at the Wyckoff positions 8b (0.25, 0.25, 0.25) and 24d (u, 0, 0.25), where u = -0.0326 at T = 300 K[174]. Both yttrium atoms are octahedrally coordinated by oxygen atoms (refer to Figure 5.10).

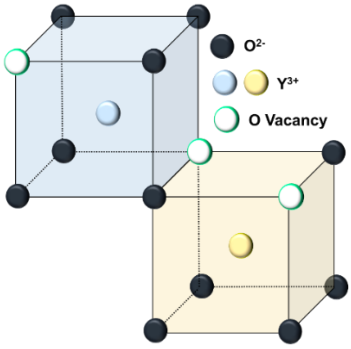

Figure 5-10 | Visual representation of yttrium coordination in bixbyite Y_2O_3. The Y atoms, colored blue and yellow, are octahedrally coordinated. Anionic vacancies and anionic sites are depicted in white and dark grey, respectively.

Furthermore, the second coordination shell of yttrium atoms (responsible from Y-Y) is divided into two distinct groups, each consisting of six yttrium atoms, located at approximately 3.5 Å and 4.0 Å.

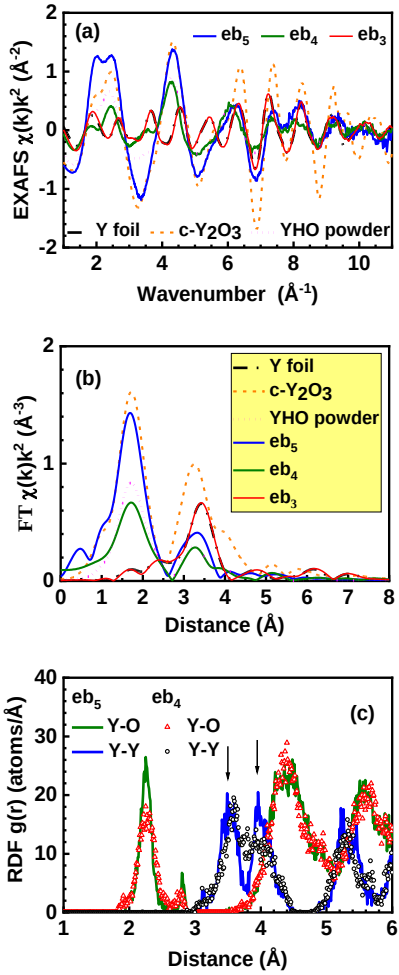

Figure 5-11 | Y K-Edge EXAFS of all samples including references, and radial distribution functions for eb_4 and eb_5. (a) Y K-edge EXAFS spectra $\chi(k)k^2$ and (b) their Fourier transforms (FTs) for the eb_3, eb_4, and eb_5 thin films, along with reference compounds (Y foil, bulk c-Y_2O_3, and YHO powder). Only the moduli of the FTs are shown. (c) Partial radial distribution functions (RDFs) g(r) for Y-O and Y-Y in the eb_4 (open symbols) and eb_5 (solid lines) thin films, derived from the Y K-edge EXAFS spectra using the RMC method. Arrows highlight two groups of yttrium atoms in the second shell.

For samples eb_4 and eb_5, the RMC results revealed a splitting in the second coordination shell (Y-Y) for both samples. The findings for the fully oxidized yttrium structure (eb_5) align with existing literature.
However, in the oxidized yttrium hydride thin film (eb_4), increased disorder in the anionic coordination shell (first coordination shell) of yttrium leads to a reduction in the first peak, attributed to the broadening of the cation-anion distribution (refer to Figure 5.11). Additionally, the splitting of the cationic coordination shell (second coordination shell around Y) distribution within the 3-4.5 Å range is less pronounced, and the distribution of yttrium atoms around 4 Å becomes more broadened. These observations indicate the presence of at least two broad families of distinct cationic geometric structures, each potentially comprising multiple specific structures. In Chapters 6 and 7, we will further investigate how temperature and light affect this splitting.

5.5 Conclusion

One of the key outcomes of this study is the identification of a multi-layered oxidized yttrium hydride thin film with notable photochromic properties. What differentiates this multilayer structure is the presence of distinct, localized stoichiometric variants, enriched in either hydrogen or oxygen. Evidence for this conclusion is primarily supported by X-ray photoelectron spectroscopy (XPS), spectroscopic ellipsometry (SE), transmission electron microscopy (TEM), and ion beam analysis (IBA).

Ellipsometry measurements provided detailed insights into the film thickness, surface roughness, optical band gap, and the (n, k) dispersion curves over a broad photon energy range (5.9 to 0.7 eV). For the first time, the (n, k) dispersion curves for electron beam-deposited YHO thin films have been reported in both the transparent and Photodarkened states following UV irradiation. A significant difference in the refractive index and extinction coefficient was observed between the bleached and Photodarkened states.

Furthermore, shifts in the Y K-edge position in XANES spectra indicate an effective oxidation state of approximately 2.5+ for yttrium ions in the oxidized hydride thin films. EXAFS analysis using the reverse Monte Carlo (RMC) method confirms the nanocrystalline structure of the YHO film. The local environment around the yttrium also exhibits splitting in the second coordination shell.

Chapter 6

6 Temperature-Dependent Structural Variation in Photochromic Yttrium Oxyhydride

In chapter 5 we discussed the potential origins of the splitting observed in the second coordination shell around Y in photochromic YHO structures. Here, we will explore this phenomenon in greater detail and investigate the effects of temperature, particularly at cryogenic temperatures. The photochromic YHO powder used in this thesis was obtained by carefully scraping the deposited thin film from a large-area substrate (refer to Figure 6.2). Thin films of YHO were deposited onto glass substrates using a two-step reactive sputtering process. During the first step, the deposition was performed in a mixed Ar-H_2 atmosphere, maintaining an H_2:Ar flow ratio of 1:10 (sccm) and a deposition pressure close to 1 Pascal (Pa). In the subsequent step, oxidation was achieved in ambient air using a Leybold Optics A550V7 magnetron sputtering system.The detailed Information regarding sample production, characterization, and computational research can be found in the corresponding article [65].

6.1 Optical Characterization

The photochromic characteristics of the YHO thin film are shown in Figure 6.1. Additionally, the large-area samples exposed to sunlight are demonstrated in Figure 6.2.

The transmission measurements (under laboratory conditions) were calibrated against air transmission, with optical scans performed across the 300 nm to 1000 nm wavelength range. To study the photochromic properties, the samples were illuminated for 30 minutes using a 405 nm Laser Diode with a power density of approximately 4.5 mW cm^{-2}. For cyclic testing, the average optical transmission between 650 nm and 850 nm was continuously monitored for 30 minutes during alternating on and off states of the laser.

Note:

In this chapter, optical characterization was performed on the thin-film form of YHO deposited on a soda-lime glass substrate. Further structural characterization and radial distribution function analysis were carried out on the powder form of YHO, obtained by scraping the thin film from the substrate.

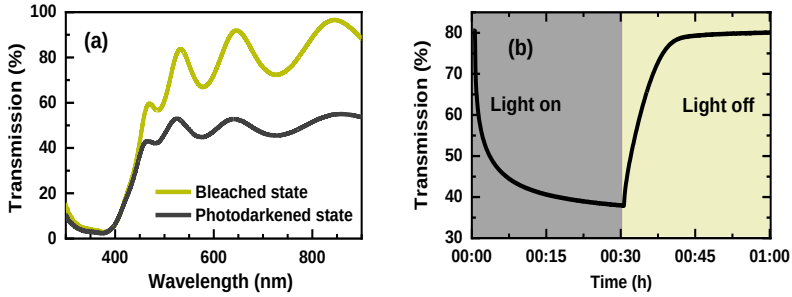

Figure 6-1 | Photochromic efficiency of YHO. (a) Transmission measurements of the YHO sample on a glass substrate in both transparent and Photodarkened states were conducted in a laboratory environment. (b) One-hour cycling test of the photochromic YHO sample on a glass substrate, performed in a laboratory environment.

Figure 6-2 | Natural photochromic efficiency of YHO. A 200 mm^2 photochromic YHO sample was exposed to sunlight for 15 minutes, visually displaying its transparent and Photodarkened states.

6.2 Structural Characterization

The procedure starts with the XRD analysis of the powder sample (refer to Figure 6.3a). Notably, this XRD measurement and refinement are the only ones used throughout this thesis to ensure consistency, strongly suggesting that the photochromic YHO predominantly forms in the Fm-3m crystal structure.

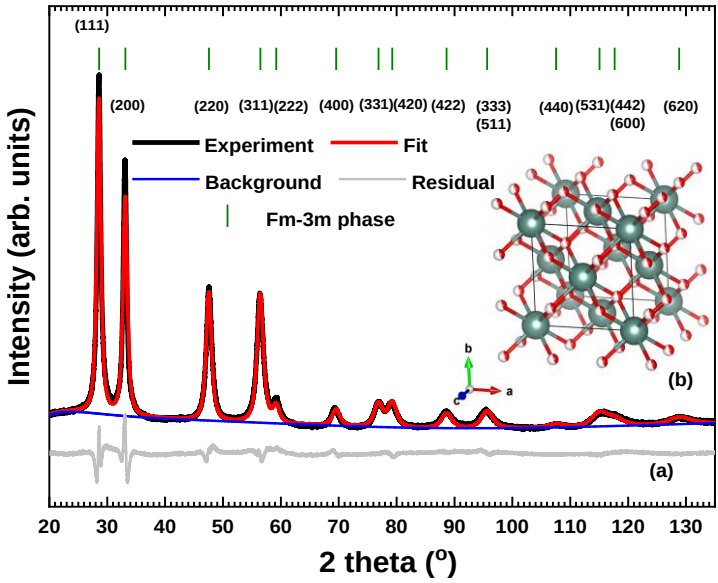

Figure 6-3 | Structural characterization of photochromic YHO powder. (a) X-ray diffraction measurement of the sample along with the refinement. (b) Unit cell representation of YHO, where grey spheres represent yttrium atoms located at FCC positions, and white/red spheres represent oxygen and hydrogen atoms positioned at interstitial sites.

XRD pattern of YHO powder was recorded at room temperature using a benchtop Rigaku MiniFlex 600 X-ray powder diffractometer in Bragg-Brentano θ-2θ geometry (refer to Figure 6.3a, black line). Data were collected over a 2θ range of 20–140° with a step size of Δ(2θ) = 0.005°, utilizing a 600 W Cu Kα radiation source (40 kV, 15 mA). A D/teX Ultra 1D high-speed silicon strip detector was used to capture the XRD pattern.

Refinement was then carried out on the measured Bragg peaks, which were indexed using the cubic space group Fm-3m (225). Our structural model builds upon the previously proposed model[74], which was defined using

synchrotron radiation powder diffraction (SR-PXD) and powder neutron diffraction (PND).

In this structure (refer to Figure 6.3b), yttrium and oxygen atoms occupy the high-symmetry Wyckoff positions 4a (0,0,0) and 8c (0.25,0.25,0.25), respectively, with yttrium forming an fcc sub-lattice surrounded by up to eight oxygen atoms in the first coordination shell. Refer to Table 6.1 in which the structural parameters are given.

Table 6-1 | Refined structure parameters for the sample from XRD. The cubic (space group Fm-3m (225)) lattice parameter a = 5.404(3) Å. Crystallite size d = 16(2) nm.

Element	Wyckoff position	Atomic coordinates	Occupation	B_{iso} (Å^2)
Y	4a	0, 0, 0	1	1.5(1)
O	8c	0.25, 0.25, 0.25	0.40(2)	5.2(3)

Unlike the referenced study[74], which used neutron diffraction (sensitive to hydrogen) and proposed Wyckoff positions for hydrogen, our study did not include this due to the weak sensitivity of X-rays to hydrogen.

The lattice constant we measured, a = 5.404(3) Å, is slightly larger than the value of a = 5.3226(3) Å reported in reference[74]. This discrepancy could be attributed to the small crystallite size of d = 16(2) nm in our sample.

As detailed in the referenced study[74] and evident from our research (will be explained), the interstitial positions and relative anionic concentration remain uncertain. To clarify the cationic local structure, we employed X-ray absorption spectroscopy. While the experimental results related to photochromic YHO, as shown in Chapters 5 and 6, provide the EXAFS spectrum, this chapter will focus on the origin of the observed splitting in the second coordination shell around the yttrium.

6.3 Radial Distribution Function Analysis

The RMC method, using an evolutionary algorithm approach [115,116] was employed. The comparison between experimental and calculated temperature-dependent k-weighted EXAFS signals and their corresponding Fourier transforms are represented in Figure 6.4. Interested readers are encouraged to find further details on the simulation in our published article[65].

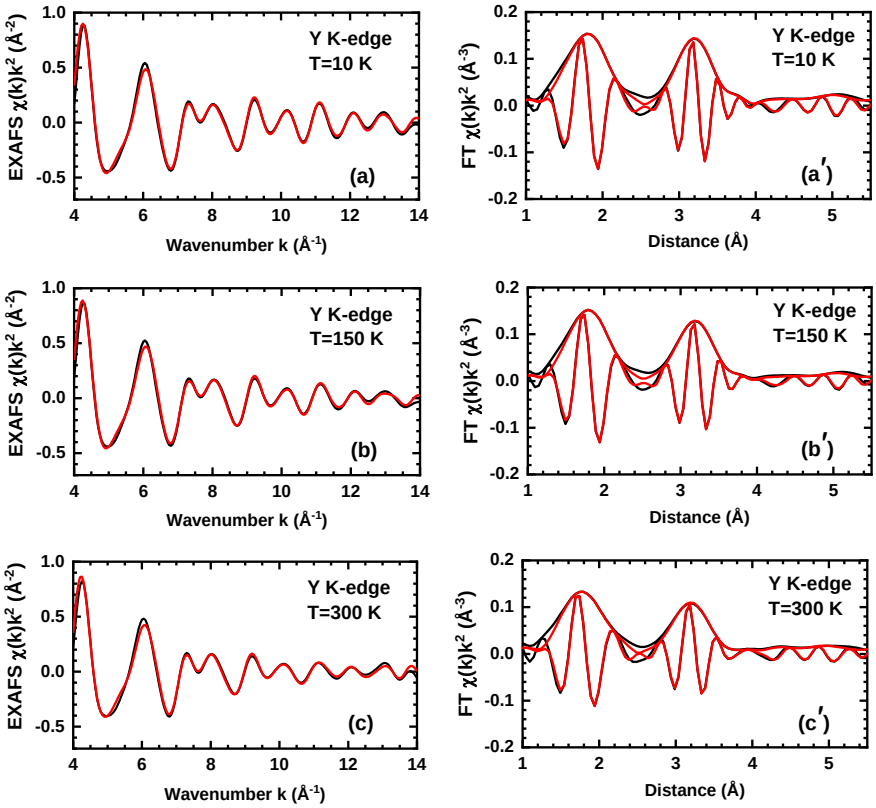

Figure 6-4 | Temperature-dependent EXAFS of powder YHO. Experimental (black) and RMC-calculated (red) Y K-edge EXAFS spectra $\chi(k)k^2$ (a, b, c) and their corresponding Fourier transforms (a′, b′, c′) at (a; a′) 10 K, (b; b′) 150 K, and (c; c′) 300 K.

The temperature-dependent radial distribution functions for atomic pairs (Y-Y, Y-O, O-O), obtained from the RMC, are shown in Figure 6.5.

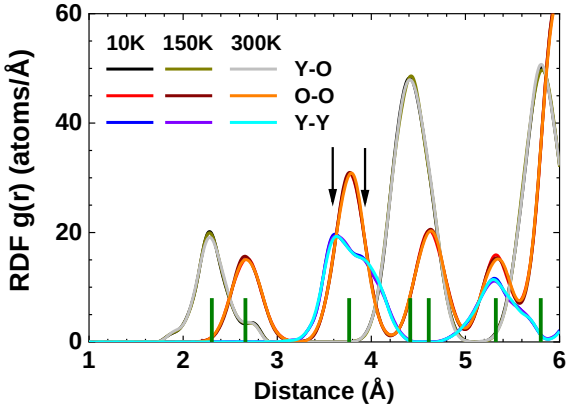

Figure 6-5 | Temperature-dependent radial distribution functions (RDFs) of Y-O, O-O, and Y-Y in YHO powder with coordination shells and Y-Y splitting. The RDFs for Y-O, O-O, and Y-Y in YHO powder at 10, 150, and 300 K were obtained using the RMC method from Y K-edge EXAFS spectra. Coordination shell positions are marked with vertical bars based on XRD data, and arrows indicate the observed splitting in the Y-Y distribution within the second coordination shell of yttrium atoms.

These RDFs measurements at different temperatures, show considerable similarity, suggesting minimal thermal disorder effects. At higher temperatures, the first peak at 2.3 Å, representing the first coordination shell of Y, exhibits some broadening.

The peak positions in the partial RDFs align well with the average values predicted by the crystallographic structure (as indicated by vertical bars in Fig. 6.5), except for the second coordination shell of yttrium. Specifically, the peak at 3.8 Å in the Y-Y RDF is significantly broadened and divided into two components at 3.6 and 3.9 Å.

This splitting is inconsistent with the commonly accepted cubic Fm-3m structure (reference[74]) and as suggested by our XRD results (refer to Fig. 6.3), where all yttrium atoms are equivalent and occupy the high-symmetry Wyckoff position 4a (0,0,0) (refer to Table 6.1).

Such splitting also contradicts any structure where yttrium atoms form a perfect face-centered cubic (fcc) lattice. This suggests that local distortions are present in the YHO structure, particularly around the yttrium sites. However, these distortions seem to be minimal, as they do not cause significant symmetry reduction detectable by diffraction. The observed distortions could be attributed to minor variations in the local environment around yttrium atoms, potentially resulting from differences in Y-O and Y-H bond interactions. This phenomenon will be further discussed in Chapter 7.

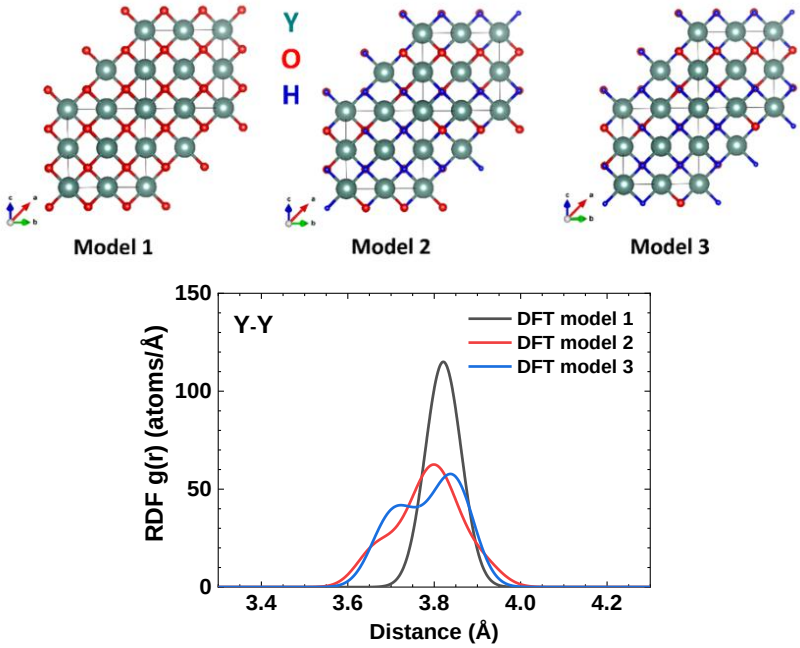

Figure 6-6 | RDFs for Y-Y Distance in YHO with the effects of anionic ratios. Partial radial distribution functions (RDFs) g(r) for Y-Y interatomic distance in the second coordination shell of yttrium in YHO obtained from the results of the first-principles DFT calculations for three models with different O:H ratios: O:H = 1:0 for model 1; O:H = 2:5 for model 2, and O:H = 5:12 for model 3 (see text for details). The RDFs for Y-O, O-O, and Y-Y in the Initial structural models of YHO were used in the DFT LCAO calculations. Y, O, and H atoms are shown by teal, red, and blue colors, respectively.

The splitting observed in the second coordination shell around Y in the YHO structure is not an artifact but a verified and consistent experimental observation, as demonstrated in this chapter and Chapter 5. Because photochromic YHO is a stoichiovariants material the following question must be answered. What is the reason behind the splitting we observed and does it depend on the anionic ratio?

To explore the origin of the second shell splitting in the Y-Y RDF, first-principles DFT calculations were performed on three structural models of YHO with varying anionic ratios.

In the first model, all yttrium atoms are surrounded by eight oxygen atoms, maintaining high-symmetry Wyckoff positions after structural relaxation, which prevents any distortion in the yttrium second shell (refer to Figure 6.6, black curve).

In the second model, the substitution of ten oxygen atoms with hydrogen introduces a non-symmetric environment around the yttrium, resulting in the distortion of the second Y-Y shell after relaxation (refer to Figure 6.6, red curve).

In the third model, substituting eleven oxygen atoms with hydrogen and adding one additional hydrogen atom caused the second Y-Y shell to split into two distinct peaks (refer to Figure 6.6, blue curve).

The DFT calculations indicate that the distortion of the second shell of yttrium arises from local symmetry breaking caused by the introduction of hydrogen atoms into the structural model. Additionally, the results suggest that anionic imbalance plays a crucial role in the formation of the splitting. However, the splitting shows only a subtle dependence on temperature variations.

6.4 Conclusion

In Chapter 5, we noted that most cations exhibit an oxidation state of approximately 2.5 +, with a distinct splitting observed in the second coordination shell (Y-Y). This chapter investigates the temperature dependence (10, 150, and 300 K) of the local atomic structure, specifically focusing on the splitting in the second coordination shell, within the transparent state of the photochromic YHO system. The structural properties of yttrium oxyhydride were analyzed using X-ray diffraction and X-ray absorption spectroscopy, which provided insights into both long-range and short-range order. Rietveld refinement of the X-ray powder diffraction data indicated that yttrium oxyhydride crystallizes into a nanocrystalline cubic phase (space group Fm-3m, 225), with a lattice parameter of a = 5.404(3) Å.

Analysis of the Y K-edge EXAFS spectra at the three different temperatures, conducted via the reverse Monte Carlo method, facilitated the reconstruction of partial radial distribution functions (g(r)) for the Y-O, O-O, and Y-Y atomic pairs. Comparisons of these findings revealed minimal effects of thermal disorder throughout the studied temperature range. The splitting of the second coordination shell observed consistently with Chapter 5, was again evident in the Y-Y radial distribution function, indicating local structural distortions associated with variations in Y-O and Y-H bonding. These observations were further supported by DFT calculations.

Chapter 7

7 Role of Anion Vacancies and Lattice Dynamics in Photochromic Yttrium Oxyhydride

In this chapter, we investigate the light-induced structural changes of magnetron-sputtered photochromic YHO thin film at both nano and atomic scales, which is identical to the material analyzed in previous chapters (5 and 6). For further experimental details regarding the thin film production and characterization methods, readers are encouraged to consult the corresponding article[175].

7.1 Optical and Nanoscale Structural Characterization

The investigation began with XRD and transmission measurements of the YHO thin film in its transparent state. The sample was then exposed to UV light under laboratory conditions, and the measurements were repeated for both the Photodarkened and bleached states. The corresponding optical and structural results are presented in Figures 7.1 and 7.2, respectively.

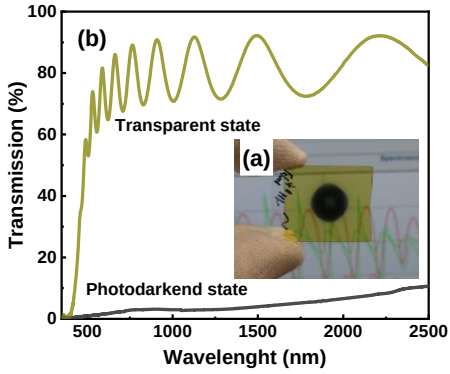

Figure 7-1 | Light-Induced Optical Changes in YHO. (a) A visual representation of the YHO thin film on a glass substrate, showing a central Photodarkened spot surrounded by a transparent region with a greenish hue. (b) Transmission measurements corresponding to the regions shown in (a), highlight the optical properties of the Photodarkened and transparent states.

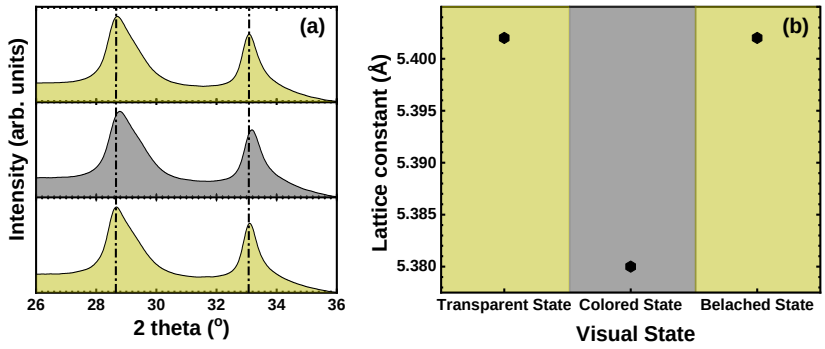

Figure 7-2 | Light-Induced Structural Changes in YHO. (a) XRD patterns of the YHO sample in its transparent, Photodarkened (colored), and bleached states, demonstrate the structural variations. (b) Lattice parameters of the material corresponding to the transparent, Photodarkened, and bleached states as indicated in (a).

As illustrated in Figure 7.1, illumination causes a significant change in the transmission of the YHO thin film on a glass substrate. Figure 7.1a shows the darkened state at the center, indicating the Photodarkened condition, while the surrounding area remains in the transparent state. This substantial transition occurs over an energy range of approximately 0.5 to 4 eV, as represented in the graphical transmission measurement in Figure 7.1b. The results also indicate that the YHO material we produce is highly responsive to light. The x-ray diffraction (XRD) measurements of the sample when its transparent, Photodarkened, and bleached states are given (refer to Figure 7.2a). Our results are consistent with a previous study[63], where the research team observed light-induced lattice contraction. We also calculated the lattice parameters for each state, as shown in Figure 7.2b.

The light-induced nanoscale structural changes observed in the XRD data, combined with the lack of a clear explanation behind this phenomenon, prompted us to investigate the material at the atomic scale.

7.2 Light-Induced Chemical and Structural Characterization

To achieve this, we used X-ray absorption spectroscopy to analyze the local structure around the cationic (Y) sites. We examine the absorption spectra in two distinct regions: 1) X-ray Absorption Near Edge Structure

(XANES) and 2) Extended X-ray Absorption Fine Structure (EXAFS). For further details, please refer to the theoretical chapter (chapter 3.3.3).

X-ray absorption spectra were collected for YHO thin films in both their transparent and Photodarkened forms. These measurements were performed at the Y K-edge (17038 eV) utilizing fluorescence mode at the DESY PETRA-III P65 undulator beamline. To eliminate harmonic interference, an Rh-coated silicon plane mirror was used, along with a fixed-exit Si (111) double-crystal monochromator for accurate energy resolution. The X-ray intensity before interacting with the sample was assessed using a nitrogen-filled ionization chamber. The fluorescence emitted by the sample was captured by a passivated implanted planar silicon (PIPS) detector, which was positioned at a 90° angle to the incoming beam. The resulting X-ray absorption near-edge structure (XANES) and extended X-ray absorption fine structure (EXAFS) spectra were derived from the experimental data with the help of the XAESA software.

We begin our discussion with the XANES region (refer to Figure 7.3), which provides valuable insights into the oxidation state, local electronic structure, and coordination environment surrounding the absorbing atom. The XANES spectra for both films reveal several distinct features: a shoulder (region 1) and two prominent peaks (regions 2 and 3) positioned above the absorption edge. These features are associated with the electronic transitions of Yttrium 1s electrons into unoccupied Y p-states, which are hybridized with oxygen p-states.

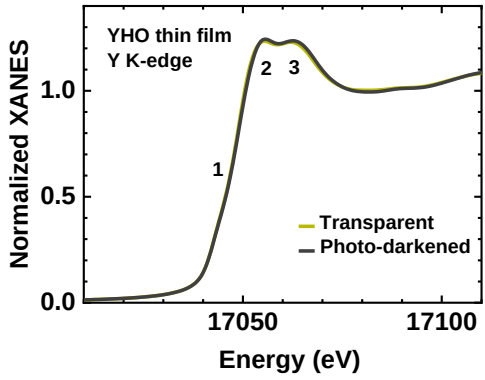

Figure 7-3 | Normalized X-ray Absorption Near Edge Structure (XANES) Spectra. The spectra are represented by transparent and Photodarkened states of YHO thin film.

XANES measurements were represented for the thin film in both its transparent and Photodarkened states (refer to Figure 7.1a for a visual representation of these states). The absence of a detectable shift in the absorption edge position, as shown in region 1 of Figure 7.3, suggests that the effective/average oxidation state of the cations does not change due to light exposure, with the majority of the Y cations having an oxidation state of approximately 2.5 +, as discussed in chapter 5.

Expanding on the interpretation of light-induced changes in the predominant oxidation states of the cations, we now shift our focus to the EXAFS region of the X-ray absorption spectrum to explore the light-induced localized structural variations of the cations. The k-weighted EXAFS spectrum (momentum space representation (a)) and its corresponding Fourier transform (position space representation (b)) are presented in Fig. 7.4. The light-induced structural variation is evident in the first and second coordination shells of yttrium (refer to Figure 7.4), leading to an increase in peak amplitude at 1.8 and 3.3 Å in the Fourier transforms. This difference becomes more significant when examining the second peak, which corresponds to the Y-Y distance.

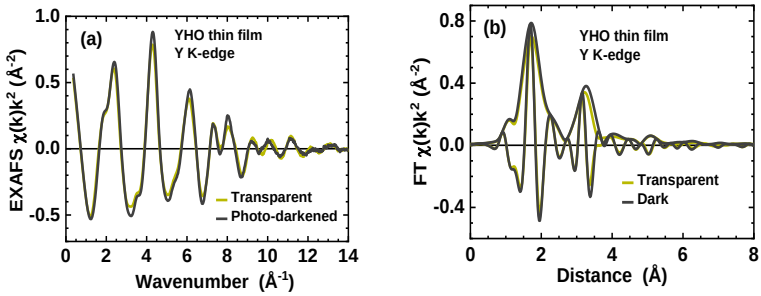

Figure 7-4 | XAS spectrum. (a) k-weighted spectrum of YHO thin film in both its transparent and Photodarkened states. (b) Corresponding position-space representation of the local structure around Y.

The difference observed in the second coordination shell was further investigated using RMC methods, as illustrated in Figure 7.5. The details of the calculations can be found in the related article.

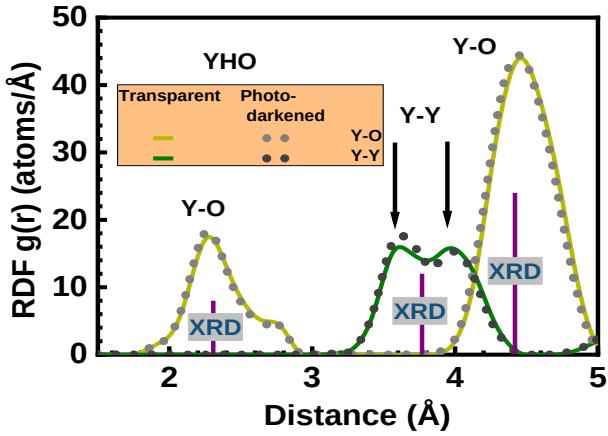

Figure 7-5 | Radial Distribution Functions of YHO Thin Films: Comparison of Transparent and Photodarkened States. Partial radial distribution functions (RDFs) g(r) for Y–O and Y–Y in transparent (solid lines) and photodarkened (dotted lines) YHO thin films were derived from the Y K-edge EXAFS spectra using the RMC method. The vertical bars indicate the positions of coordination shells, which are based on crystallographic data obtained from X-ray diffraction (see Fig. 6.3).

The atomic coordinates obtained from the RMC method were utilized to calculate the partial radial distribution functions (RDFs) g(r) for Y–O and Y–Y in both transparent and photodarkened YHO thin films, as illustrated in Figure 7.5. This analysis yields two important conclusions. First, the second coordination shell of yttrium cations is divided into two distinct subshells, which correspond to peaks at 3.62 Å and 3.98 Å. These findings indicate that the splitting persists even in the transparent state of YHO, reflecting variations induced by visible light. While the observed splitting and its temperature dependence were discussed in Chapters 5 and 6, the light-induced variations at the nano and atomic scales were not addressed.

7.3 Relationship Between Atomic-Scale and Nanoscale Structural Variations

Here, we establish a connection between these aspects by introducing a new approach that examines anionic vacancies in YHO structures. A key driving force behind this investigation is the observation from XAS, which indicates that while the majority of cations do not exhibit light-induced

variations in their oxidation state, a structural change is still induced by visible light.

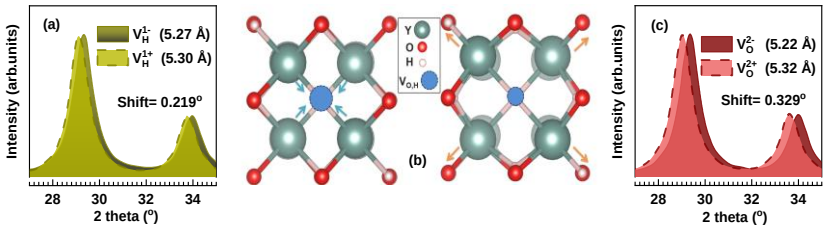

Figure 7-6 | Light-Induced Structural Modifications in Yttrium Oxyhydrides. (b) Local structural arrangements around anion vacancies (VH^{1-}, VO^{2-} (on the left) and VH^{1+}, VO^{2+} (on the right)) in YHO induced by light; (a) the corresponding shift in XRD peak position for vacancy type VH, along with the associated lattice constants; and (c) the related shift in XRD peak position for vacancy type VO, including the corresponding lattice constants.

The experimental observation presented in Figure 7.2a, based on XRD data, demonstrates that under UV light, the material undergoes reversible lattice relaxation, exhibiting contraction during UV exposure followed by expansion once the UV exposure has ceased (the photochromic efficiency of YHO is given in Figure 6.1.).

We investigated the causes of reversible lattice relaxation using first-principles calculations, revealing the dynamic behavior of anionic vacancies. Light absorption transfers electrons from the valence band to defect states, changing charge states from VH^{1+} to VH^{1-} and VO^{2+} to VO^{2-}. Lattice optimization showed significant relaxation, with Y cations moving outward for VO^{2+} and VH^{1+}, and inward for VO^{2-} and VH^{1-} (refer to Figure 7.6b), causing light-induced lattice contraction and expansion. XRD peaks (refer to Figure 7.6a-c) for the Photodarkened film with VO^{2-} and VH^{1-} shifted to larger angles compared to the transparent films with VO^{2+} and VH^{1+}.

The presence of vacancies in the cationic environments elucidates the persistence of the oxidation state of the majority of cations in both the transparent and Photodarkened states of YHO, despite observable structural variations. Furthermore, the incorporation of anionic vacancies surrounding the cations accounts for the deviation of YHO from an ideal Fm-3m structure, in line with the interpretations presented in Chapters 5 and 6. Additionally, the RDF results[173] for Y_2O_3 demonstrate a splitting in the second cationic coordination shell (Y-Y), indicating that yttrium exhibits two distinct octahedral environments, each associated with anionic vacancies.

7.4 Electronic Structure and Optical Characterization

Anion vacancies are pivotal in driving light-induced structural modifications, as mentioned earlier. When examining the light-induced optical changes in photochromic YHO, our attention centers on the material's electronic band structure. In yttrium oxyhydride (YHO), these vacancies can create localized energy states within the band gap, potentially improving the absorption or reflection of sub-bandgap photons that correspond to specific colors.

Figure 7.7 illustrates the modified electronic band structure that includes VO^{2+}(red-lines) and VH^{1+}(green-line), with results derived from hybrid functional calculations. The electronic structure of ideal YHO can be found in our related article[175], which documents the optical excitation threshold as being around 3.9 eV.

Depending on their charge states, VO and VH generate distinct energy levels within the band gap of YHO. For instance, VH^{1+} introduces a band approximately 2.3 eV (green) above the highest valence band, as shown in Figure 7.7a. In contrast, VO^{2+} creates several bands positioned around 1.0 eV (near infrared) and 3.0 eV (UV) above the highest valence band, depicted in Figure 7.7b. Alterations in charge states will lead to changes in these energy levels.

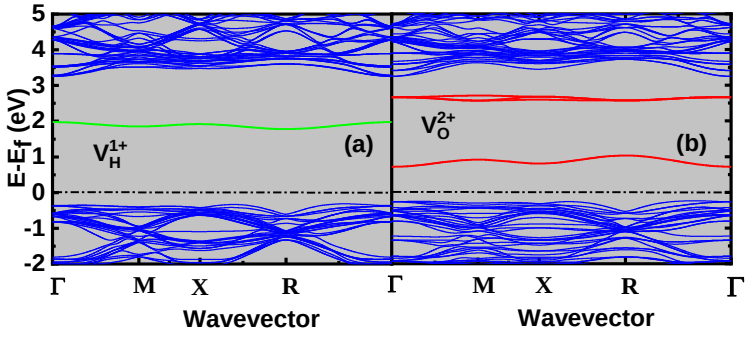

Figure 7-7 | Modified band structure of YHO. The electronic band structure of yttrium oxyhydride (YHO) in the presence of specific vacancies: (a) VH^{1+} representing hydrogen vacancies and (b) VO^{2+} indicating oxygen vacancies.

The alteration of the electronic band structure of YHO due to anionic vacancies, particularly when considering their combinations, leads to the absorption of wavelengths with specific energies.

Consequently, this results in a darkening of the material's color. Figure A2 presents the CIE Lab color space diagram, showcasing all visible colors and their combinations that lead to the creation of deeper shades.

Anion vacancy-induced photochromism, as observed in YHO, has been previously identified in other materials, including Al_2O_3[176], $BaMgSiO_4$[177], and naturally occurring minerals from the aluminosilicate group such as hackmanite ($Na_8Si_6Al_6O_{24}Cl_2$), tugtupite ($Na_8Al_2Be_2Si_8O_{24}Cl_2$), and scapolite ($[Na, Ca]_4Al_3Si_9O_{24}[Cl, CO_3]$)[178].

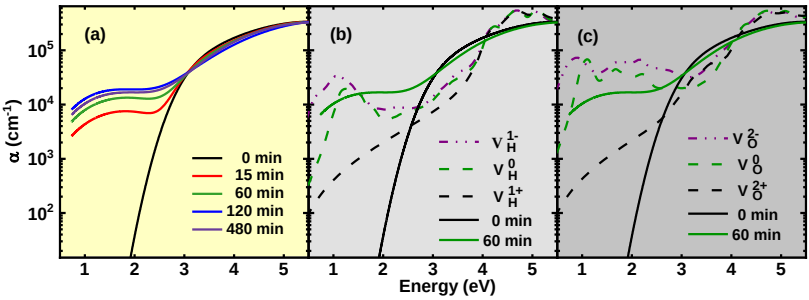

Figure 7-8 | Time-Resolved Absorption Coefficient and Anion Vacancy Comparison in YHO Films. (a) Spectral distribution of the absorption coefficient was recorded at different time intervals 0, 15, 60, 120, and 480 minutes during UV light exposure. (b) The calculated absorption coefficient for YHO films with hydrogen anion vacancies, and (c) for oxygen anion vacancies, both compared with experimentally measured curves at 0 and 60 minutes.

We examined the optical characteristics of YHO thin films using time-resolved spectroscopic ellipsometry (trSE), as illustrated in Figure 7.8a. The results reveal that, in the transparent state, the absorption coefficient in the visible spectrum is minimal. This is attributed to the highly localized nature of anion vacancy-induced states (refer to Figures 7.8b-c), leading to weak light absorption. The theoretical absorption coefficients for YHO with VH^{1+}, VH^{1-}, VO^{2+}, and VO^{2-} closely match those obtained from trSE for Photodarkened films. The analysis indicates that the strong light absorption in YHO within the visible range primarily results from hydride and oxide anion vacancies. Discrepancies between theory and experiment may stem from uncertainties in fitting the ellipsometry parameters from trSE measurements, as well as the complex nature of the defect spectra and their associated energy levels in YHO thin films.

7.5 Conclusion

Chapters 5, 6 and 7 are intricately interconnected, each building upon the previous one to provide a comprehensive understanding of the YHO system. The construction of these chapters is critical, as it allows for a systematic exploration of various aspects of the material. Chapter 5 focuses on defining the stoichiometric nature, crystal structure, and average oxidation state of the cations, laying a foundational understanding essential for subsequent analyses. In Chapter 6, we extend our examination to confirm these structural properties and investigate the temperature-dependent variations in the cationic (Y-Y) coordination shell. This logical progression not only reinforces the initial findings but also establishes a clear link between light-induced nanoscale changes and atomic-level structural modifications.

Finally, chapter 7 integrates these insights to discuss the implications of our findings on the photochromic behavior of the YHO system. Through first-principles calculations, we demonstrate that vacancies in the hydride and oxide anions introduce deep localized energy levels within the band gap, enhancing light absorption capabilities. These anion vacancies are pivotal to the photochromic effect observed in the system. The light-induced changes in the charge states of the oxide and hydride anion vacancies lead to localized structural rearrangements, potentially causing lattice contraction and shifts in the X-ray diffraction peaks toward higher angles. Moreover, analyses performed using X-ray absorption spectroscopy (XAS), in conjunction with reverse Monte Carlo (RMC) simulations and assessments of the partial radial distribution functions (RDFs), reveal a significant splitting in the Y-Y distance, characterized by the emergence of two distinct peaks. This phenomenon is likely attributed to the presence of anion vacancies, which would not be expected in an ideal YHO lattice exhibiting face-centered cubic (fcc) symmetry, where Y cations occupy equivalent positions. Complementary compositional analysis conducted with ion beam techniques indicates that the samples are not stoichiometric, further confirming the substantial presence of hydride and oxide anion vacancies.

Chapter 8

8 Conclusion

This treatise aims to provide a comprehensive understanding of yttrium-based systems, primarily focusing on yttrium oxyhydride (YHO) as a double-anion system (H, O), while also addressing yttrium monoxide (YO) as a single-anion system (O).

In the single-anion system, we investigated the growth kinetics of yttrium/yttrium oxide thin films across ultralow to moderate oxygen partial pressures. Our findings reveal that during thin film deposition/evaporation at low/ultralow oxygen partial pressures, yttrium predominantly forms a hexagonally structured metallic phase, accompanied by sub-oxides. Based on our analysis, we propose that β-Y_2O_3 is the most probable sub-oxide under ultralow oxygen partial pressures. As the oxygen partial pressure increases, oxygen atoms integrate into the metallic crystal lattice and/or facilitate the formation of additional sub-oxide phases. This process gradually leads to the material's amorphization, transitioning it into an electrically insulating state, ultimately resulting in full amorphization. At sufficiently high oxygen levels, fully oxidized Y_2O_3 crystals form at room temperature. Nevertheless, the precise upper and lower oxygen partial pressure limits for the concurrent formation of metallic yttrium crystals and sub-oxides in yttrium/yttrium oxide thin films remain unclear. In the partial pressure range where the material becomes fully amorphous, deposition at elevated temperatures promotes the formation of semiconducting yttrium monoxide (YO) alongside Y_2O_3.

In the double anion system, the structural characteristics of photochromic YHO are explored at both nanoscale and atomic levels, along with the effective state of the cations. Our analysis examines YHO's photochromic behavior from three different perspectives, offering a deeper understanding of its light-induced kinetics. We propose that photochromic YHO has a stoichiovariants nature, with most yttrium atoms exhibiting an oxidation state around 2.5 +, a state that remains stable between bleached and photodarkened conditions. The distorted face-centered cubic (FCC) structure of YHO shows splitting in the second coordination shell around the yttrium, caused by the addition of extra hydrogen atoms and random substitution of oxygen by hydrogen within the FCC lattice. This splitting points to the presence of two broad families of distinct cationic geometric structures, each potentially containing multiple configurations. In the literature, a similar phenomenon is observed in Y_2O_3, where yttrium atoms are coordinated by oxygen atoms in two distinct octahedral environments.

Moreover, the observed shell splitting in the transparent state shows subtle temperature dependence, further emphasizing the complexity of the system. We also suggest that the light-induced structural variations observed through XRD are closely tied to localized movements of anionic defects, which induce distortions in the second coordination shell around the yttrium.

We have also observed a correlation between single-anion and double-anion systems. Yttrium's propensity to form sub-oxide phases under ultralow oxygen partial pressures during the deposition or evaporation of YH thin films (considered the initial state for producing photochromic YHO) suggests that the film may consist of a mixture of YH, YO, or even YHO. This simultaneous formation appears to be directly linked to the photochromic performance of YHO.

To explore this further, we monitored the evolution of residual gas species during the deposition of yttrium hydride (YH) and yttrium (Y) thin films using a mass spectrometer. The detailed results of these measurements will be presented in a separate study. Figure 8.1 highlights the fluctuations in partial pressures of key residual gases, including hydrogen (H_2), oxygen (O_2), and water vapor (H_2O), over time, providing insights into the deposition process. During YH thin film deposition, hydrogen plays a vital role in promoting oxygen absorption. The resulting hydrogen-oxygen interactions are likely absorbed or accumulated by components within the process chamber, including the deposited film, target surface, and inner chamber elements. For Y thin films, residual gas behavior is similar, although hydrogen exhibits more pronounced variations during deposition and is highly sensitive to changes in partial pressure levels.

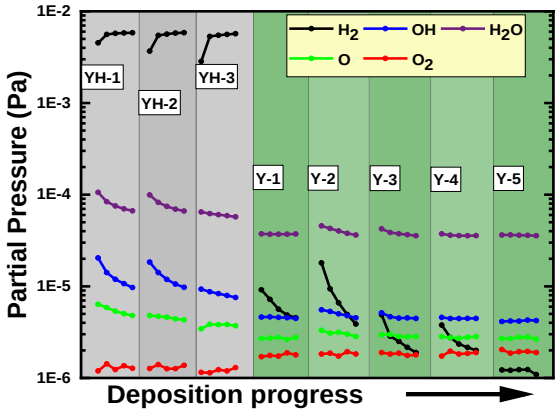

Figure 8-1 | Residual gases kinetics during YH and Y metal thin film deposition. This image represents the time evolution of residual gas species observed during the deposition of yttrium hydride (YH) and yttrium (Y) metal thin films.

Additionally, we conducted a comparative chemical study between photochromic YHO and semiconducting YO, revealing that the effective coxidation state of yttrium in both materials is approximately 2.5 + (refer to Figure 8.2).

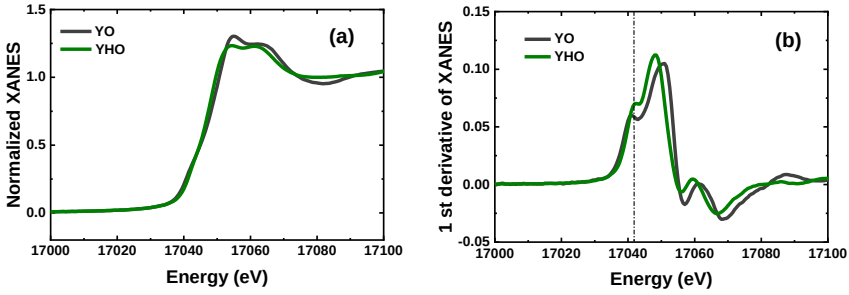

Figure 8-2 | XANES studies of photochromic YHO and semiconducting YO thin films. (a) normalized XANES spectra of the materials, with YHO representing the transparent state; (b) the first derivative of the corresponding spectra.

Chapter 9

Main Theses

1- Yttrium/yttrium oxide thin films, during deposition or evaporation under ultralow oxygen partial pressure (~10^{-7} Pa), predominantly form as metallic yttrium with a hexagonally oriented structure, accompanied by sub-oxides. As oxygen partial pressure increases, oxygen atoms become integrated into the metallic crystal lattice and/or promote the increased formation of sub-oxide phases. This results in gradual amorphization and a transition to electrical insulation. While amorphization occurs, further oxygen incorporation eventually triggers the reformation of crystalline phases, leading to the formation of fully oxidized Y_2O_3 crystals at room temperature. **(AI, AII)**

2- Yttrium/yttrium oxide thin films produced by magnetron sputtering from a metallic target attain a fully amorphous state characterized by electrical insulation and semi-transparency at an oxygen partial pressure of approximately 7.57×10^{-5} P at room temperature. However, when deposition occurs at elevated temperatures around 623 K, it promotes the simultaneous formation of semiconducting yttrium monoxide (YO), which exhibits both rock salt and amorphous phases alongside Y_2O_3, resulting in an overall semi-transparent material. (**AI)**

3- Yttrium oxyhydride (YHO) crystallizes into a face-centered cubic (FCC) lattice with the yttrium cations in the oxidation state of ~2.5+ in both bleached and Photodarkened states. **(AII, AIII, AIV)**

4- The Y-Y distance in the face-centered cubic (FCC) lattice of YHO exhibits splitting into two distinct peaks, attributed to both the incorporation of an extra hydrogen atom and the random substitution of hydride anions with oxide anions. This splitting is also influenced by light-induced changes, as the reversible shift of the XRD peak suggests local lattice rearrangements around anion vacancy sites. These vacancies, along with temperature-dependent structural changes, contribute to the observed Y-Y shell splitting and highlight the material's response to UV light exposure through hydrogen diffusion. **(AII, AIII, AIV).**

5- The reason for the photochromism of YHO is related to light absorption by the anion vacancies. The photochromic performance of the YHO thin films can be controlled by adjusting the concentration and/or ratio of anionic defects that can be managed by controlling the residual gas concentration and the H_2/Ar ratio during the film growth. **(AII, AIII, AIV)**

Author's Patent and Publication List

A. Contributions to the Doctoral Thesis

1. **PI**- Patent: **Arslan H.**, A method for deposition of yttrium monoxide film and yttrium monoxide coatings European Patent EP4033003 (Patent LV / LVP2020000090; LV15646) **(2022)**
2. **AI**- Article: **Arslan H.**, Aulika I., Sarakovskis A., Bikse l., Zubkins M., Azarov A., Gabrusenoks J., Purans J., Reactive pulsed direct current magnetron sputtering deposition of semiconducting yttrium oxide thin film in ultralow oxygen atmosphere: A spectroscopic and structural investigation of growth dynamics, Vacuum, 211 **(2023)**
3. **AII**- Article: **Arslan H.**, Kuzmin A., Aulika I, Moldarev D, Wolff M., Primetzhofer D., Pudza I., Kundzins K., Sarakovskis A., Purans J, Karazhanov S. Zh., Chemical state and atomic structure in stoichiovariants photochromic oxidized yttrium hydride thin films, Zeitschrift für Physikalische Chemie, 0 **(2024)**
4. **AIII**- Article: **Arslan H.**, Pudza I., Kuzmins A., Karazhanov S., Evidence of local structural distortions and subtle thermal disorder in transparent photochromic yttrium oxyhydride, Applied Physics Letters, 124 **(2024)**
5. **AIV**- Article: **Arslan H.**, Kuzmin A., Kumar K. V., Aulika I., Moldarev D., Primetzhofer D., Wolff M., Pudza I., Nordseth Ø., and Karazhanov S. Zh., Anion Vacancy-Induced Photochromism and Lattice Relaxation in Yttrium Oxyhydride, Submitted manuscript. https://doi.org/10.21203/rs.3.rs-5171857/v1 **(2024)**

B. Additional Research Publications

1. **BI**- Article: Zubkins M., Aulika I., Strods E., Vibornijs V., Bikse L., Sarakovskis A., Chikvaidze G., Gabrusenoks J., **Arslan H.**, Purans J., Optical properties of oxygen-containing yttrium hydride thin films during and after the deposition, Vacuum, 203 **(2022)**
2. **BII**- Article: Zubkins M., **Arslan H.**, Bikse L., Purans J., High power impulse magnetron sputtering of Zn/Al target in an Ar and Ar/O_2 atmosphere: The study of sputtering process and AZO films, Surface and Coatings Technology, 369 **(2019)**

3. **BIII**- Article: Skvortsova V., Zubkins M., Kalendarev R., **Arslan H.**, and Purans J., Optical properties of zinc-iridium oxide thin films, IOP Conference Series: Materials Science and Engineering, 503 **(2019)**

Participation in Conferences

1. FM&NT-NIBS (Poster Presentation)
   Title: "Reactive E-Beam Evaporation of Yttrium: A Spectral and Structural Analysis of Yttrium Oxide and Oxyhydride Thin Films"
   (Arslan H., Aulika I., Pudza I., Sarakovskis A., Bikse L., Zubkins M., Chikvaidze G., Purans J.)
   University of Latvia, Riga, Latvia | 03.07.2022 – 06.07.2022
2. E-MRS Virtual Conference (Poster Presentation)
   Title: "Reactive E-Beam Evaporation of Yttrium: A Spectral and Structural Investigation of Metallic Yttrium, Yttrium Oxide, and Yttrium Oxyhydride Thin Films"
   (Arslan H., Aulika I., Sarakovskis A., Bikse L., Gabrusenoks J., Zubkins M., Purans J.)
   30.05.2022 – 03.06.2022
3. Annual ISSP UL Scientific Conference (Poster Presentation)
   Title: "Reactive E-Beam Evaporation of Yttrium: A Spectral Investigation of Yttrium in Different Chemical Environments"
   (Arslan H., Aulika I., Sarakovskis A., Bikse L., Gabrusenoks J., Chikvaidze G., Zubkins M., Purans J.)
   Riga, Latvia | 22.02.2022–24.02.2022
4. E-MRS Virtual Conference (Poster Presentation)
   Title: "Nanocrystalline-Amorphous Semiconducting Yttrium Monoxide"
   (Arslan H., Aulika I., Sarakovskis A., Zubkins M., Bikse L., Gabrusenoks J., Purans J.)
   20.09.2021 – 23.09.2021
5. Annual ISSP UL Scientific Conference (Oral Presentation)
   Title: "Deposition and Properties of Yttrium Oxide Thin Films"
   (Arslan H., Zubkins M., Sarakovskis A., Purans J.)
   Riga, Latvia | 23.02.2021–25.02.2021
6. Annual ISSP UL Scientific Conference (Poster Presentation)
   Title: "Yttrium and Yttrium Oxide Thin Films Deposition by Reactive DC Magnetron Sputtering"
   (Arslan H., Zubkins M., Butikova J., Azens A., Butanovs E., Purans J.)

Riga, Latvia | 11.02.2020 – 13.02.2020

7. Advanced Materials and Technologies (Poster Presentation)
   Title: "Local Structure and Valence State of Iridium in Nanocrystalline and Amorphous Thin Film ZnO-IrO"
   (Arslan H., Skvortsova V., Zubkins M., Kalendarevs R., Purans J.)
   Palanga, Lithuania | 19.08.2019 – 23.08.2019
8. International Conference on Sputter Technology (Poster Presentation)
   Title: "Y_mO_n, Yttrium-Doped ZnO Thin Films and Multilayers"
   (Arslan H., Azens A., Zubkins M., Purans J.)
   Braunschweig, Germany | 19.06.2019 – 20.06.2019
9. E-MRS (Poster Presentation)
   Title: "Optical, Structural, and Electrical Characterization of Y doped ZnO Thin Films and Multilayers"
   (Arslan H., Azens A., Zubkins M., Purans J.)
   Nice, France | 28.05.2019 – 30.05.2019
10. Trends in Modern Photon Science (DESY) (Poster Presentation)
    Title: "Local Structure and Valence State of Iridium in Nanocrystalline and Amorphous Thin Film ZnO–IrO"
    (Arslan H., Zubkins M., Gabrusenoks J., Zitolo A., Purans J.)
    Hamburg, Germany | 27.02.2019 – 01.03.2019
11. Annual ISSP UL Scientific Conference (Poster Presentation)
    Title: "Optical and Structural Characterization of Y-doped ZnO and Y_nO_m Thin Films"
    (Arslan H., Zubkins M., Butanovs E., Bikse L., Purans J.)
    Riga, Latvia | 20.02.2019 – 22.02.2019
12. FM&NT (Poster Presentation)
    Title: "Local Structure and Valence State of Iridium in Nanocrystalline and Amorphous Thin Film ZnO-IrO"
    (Arslan H., Zubkins M., Kalendarevs R., Skvortsova V., Purans J.)
    Riga, Latvia | 02.10.2018 – 05.10.2018

Participation in International Schools

1. International Summer School “Advanced Materials for Chromogenic Device Applications” and “Thin Films: Synthesis and Characterization”
   Riga, Latvia | 02.06.2024 – 05.06.2024

2. Spectroscopy Summer School (Poster Presentation)
   Title: "Reactive E-Beam Evaporation of Yttrium: A Spectral and Structural Analysis of Yttrium Oxide and Oxyhydride Thin Films" (Arslan H., Kuzmin A., Pudza I., Sarakovskis A., Purans J., Karazhanov S.)
   MAX IV – LINXS, Lund, Sweden | 21.08.2023 – 25.08.2023

Participation in Large-Scale Research Infrastructure-Based Experiments

1. X-ray Absorption Spectroscopy (XAS) Measurement
   DESY PETRA-III, P65
   Hamburg, Germany | 18.04.2024 – 22.04.2024
2. X-ray Absorption Spectroscopy (XAS) Measurement
   DESY PETRA-III, P65
   Hamburg, Germany | 11.10.2023 – 16.10.2023
3. Rutherford Backscattering Spectrometry (RBS) and Time-of-Flight Elastic Recoil Detection Analysis (TOF-E ERDA) Measurements
   Tandem Laboratory, Uppsala, Sweden | 08.05.2023 – 11.05.2023

Chapter 10

Bibliography

1 Singh R., Prakash U., Kumar D. & Laha K. Development of creep resistant high yttria 18Cr ferritic ODS steel through hot powder forging route. Journal of Nuclear Materials, 154566 (2023).

2 Fava S. et al. Magnetic field expulsion in optically driven $YBa_2Cu_3O_{6.48}$. Nature, 1-6 (2024).

3 Mongstad T. et al. A new thin film photochromic material: Oxygen-containing yttrium hydride. Solar energy materials and solar cells 95, 3596-3599 (2011).

4 Kaminaga K. et al. A divalent rare earth oxide semiconductor: Yttrium monoxide. Applied Physics Letters 108 (2016).

5 Colombi G., Cornelius S., Longo A. & Dam B. Structure model for anion-disordered photochromic gadolinium oxyhydride thin films. The Journal of Physical Chemistry C 124, 13541-13549 (2020).

6 Kumazoe H. et al. Bayesian sparse modeling of extended x-ray absorption fine structure to determine interstitial oxygen positions in yttrium oxyhydride epitaxial thin film. AIP Advances 11 (2021).

7 Banerjee S. et al. Exploring Multi-Anion Chemistry in Yttrium Oxyhydrides: Solid-State NMR Studies and DFT Calculations. The Journal of Physical Chemistry C 127(29), 14303-14316 (2023).

8 Dam B. et al. Perspective on the photochromic and photoconductive properties of Rare-Earth Oxyhydride thin films. Solar Energy Materials and Solar Cells 273, 112921 (2024).

9 Moldarev D., Wolff M. & Primetzhofer D. Modification of the photochromic properties of oxygen-containing yttrium hydride by irradiation with keV and MeV ions. The Journal of Physical Chemistry C 127, 24676-24682 (2023).

10 Slade R. A., Parkinson B. J. & Walsh R. M. Test results for a 1.5 T MRI system utilizing a cryogen-free YBCO magnet. IEEE transactions on applied superconductivity 24, 1-5 (2013).

11 Liang L., Pang P., Wang Y., Yan Z. & Deng, Z. Design and analysis of a novel HTS thin film device as planar maglev levitator and fault current limiter. Applied Physics A 130, 331 (2024).

12 Gonçalves F. et al. Effectiveness of 980-mm diode and 1064-nm extra-long-pulse neodymium-doped yttrium aluminum garnet lasers in implant disinfection. Photomedicine and laser surgery 28, 273-280 (2010).

13 Kaushal H. & Kaddoum, G. Applications of lasers for tactical military operations. IEEE Access 5, 20736-20753 (2017).

14 Rashid W. T. in AIP Conference Proceedings. (AIP Publishing).

15 Li Y. et al. Controllable degradation behavior of Mg-Sr-Y alloys for the bio-applications. npj Materials Degradation 7, 45 (2023).

16 Xia Y., Zhang L., Zhu K., Zhang B. & Xia C. Sintering composite electrolytes of yttria-doped bismuth oxide and yttria-stabilized zirconia for solid oxide fuel cells. Journal of Solid State Electrochemistry, 1-12 (2024).
17 López-Gándara C., Ramos F. M. & Cirera A. YSZ-Based Oxygen Sensors and the Use of Nanomaterials: A Review from Classical Models to Current Trends. Journal of Sensors 2009, 258489 (2009).
18 Lima R. & Marple B. Nanostructured YSZ thermal barrier coatings engineered to counteract sintering effects. Materials Science and Engineering: A 485, 182-193 (2008).
19 Ordás N. et al. The role of yttrium and titanium during the development of ODS ferritic steels obtained through the STARS route: TEM and XAS study. Journal of Nuclear Materials 504, 8-22 (2018).
20 Auger M. et al. Effect of yttrium addition on the microstructure and mechanical properties of ODS RAF steels. Journal of Nuclear Materials 455, 600-604 (2014).
21 Ngene P., Longo A., Mooij L., Bras W. & Dam B. Metal-hydrogen systems with an exceptionally large and tunable thermodynamic destabilization. Nature communications 8, 1846 (2017).
22 Purans J. et al. Local electronic structure rearrangements and strong anharmonicity in YH_3 under pressures up to 180 GPa. Nature Communications 12, 1765 (2021).
23 Montero Amenedo J. Photochromism in rare earth oxyhydrides for large-area transmittance control. Solar Energy Materials and Solar Cells 272, 112900, (2024).
24 You C. C., Mongstad T., Maehlen J. P. & Karazhanov S. Dynamic reactive sputtering of photochromic yttrium hydride thin films. Solar Energy Mater. Solar Cells 143, 623-626, (2015).
25 Hultgren R. R. Selected values of the thermodynamic properties of binary alloys. (1973).
26 Grosshans W., Vohra Y. & Holzapfel W. High pressure phase transformations in yttrium and scandium: Relation to rare earths and actinides crystal structures. Journal of Magnetism and Magnetic Materials 29, 282-286 (1982).
27 Skriver H. L. Crystal structure from one-electron theory. Physical Review B 31, 1909 (1985).
28 Carter W. J., Fritz J., Marsh S. & McQueen R. Hugoniot equation of state of the lanthanides. Journal of Physics and Chemistry of Solids 36, 741-752 (1975).
29 Vohra Y., Olijnik H., Grosshans W. & Holzapfel, W. Structural phase transitions in yttrium under pressure. Physical Review Letters 47, 1065 (1981).

30 Liu H., Naumov I. I., Hoffmann R., Ashcroft N. & Hemley R. J. Potential high-Tc superconducting lanthanum and yttrium hydrides at high pressure. Proceedings of the National Academy of Sciences 114, 6990-6995 (2017).
31 Kong P. et al. Superconductivity up to 243 K in yttrium hydrides under high pressure. arXiv preprint arXiv:1909.10482 (2019).
32 Li Y. et al. Pressure-stabilized superconductive yttrium hydrides. Scientific Reports 5, 9948 (2015).
33 Troyan I. A. et al. Anomalous high-temperature superconductivity in YH_6. Advanced Materials 33, 2006832 (2021).
34 Huiberts J. N. et al. Yttrium and lanthanum hydride films with switchable optical properties. Nature 380, 231-234 (1996).
35 Kim D. Y., Scheicher R. H. & Ahuja R. Predicted high-temperature superconducting state in the hydrogen-dense transition-metal hydride YH_3 at 40 K and 17.7 GPa. Physical review letters 103, 077002 (2009).
36 Matsuoka T. et al. Electrical properties of YH_3 under high pressure. Journal of the Physical Society of Japan 76, 86-87 (2007).
37 Shannon R. D. Revised effective ionic radii and systematic studies of interatomic distances in halides and chalcogenides. Foundations of Crystallography 32, 751-767 (1976).
38 Gschneidner K. A., Eyring L., Lander G. & Choppin G. R. Lanthanides/actinides: chemistry. (1994).
39 Zinkevich M. Thermodynamics of rare earth sesquioxides. Progress in Materials Science 52, 597-647 (2007).
40 Sato S., Takahashi R., Kobune M. & Gotoh H. Basic properties of rare earth oxides. Applied Catalysis A: General 356, 57-63 (2009).
41 Gy G.-y. A. & Imanaka N. The binary rare earth oxides. Chemical reviews 98, 1479-1514 (1998).
42 Swamy V., Dubrovinskaya N. & Dubrovinsky L. High-temperature powder x-ray diffraction of yttria to melting point. Journal of materials research 14, 456-459 (1999).
43 Mudavakkat V., Atuchin V., Kruchinin V., Kayani A. & Ramana C. Structure, morphology and optical properties of nanocrystalline yttrium oxide (Y_2O_3) thin films. Optical Materials 34, 893-900 (2012).
44 Atanassov G., Thielsch R. & Popov D. Optical properties of TiO_2, Y_2O_3 and CeO_2 thin films deposited by electron beam evaporation. Thin Solid Films 223, 288-292 (1993).
45 Greenwood N. & Earnshaw A. Chemistry of the elements 2nd Edition. (Butterworth-Heinemann, 1997).
46 Greenwood N. N. & Earnshaw A. Chemistry of the Elements. (Elsevier, 2012).

47 Rushchanskii K. Z., Blügel S. & Ležaić M. Ab initio phase diagrams of Hf–O, Zr–O and Y–O: a comparative study. Faraday discussions 213, 321-337 (2019).
48 Arslan H. et al. Reactive pulsed direct current magnetron sputtering deposition of semiconducting yttrium oxide thin film in ultralow oxygen atmosphere: A spectroscopic and structural investigation of growth dynamics. Vacuum 211, 111942 (2023).
49 Yang Q. et al. Pressure-induced yttrium oxides with unconventional stoichiometries and novel properties. Physical Review Materials 5, 044802 (2021).
50 Brugman B. L. et al. Computationally Led High Pressure Synthesis and Experimental Thermodynamics of Rock Salt Yttrium Monoxide. Chemistry of Materials 36, 332-339 (2023).
51 Saeed N., Swart H. & Coetsee E. X-ray photoelectron spectroscopy and NIR self-quenching emission behavior in Ho^{3+} doped YOF and V-YOF. Optical Materials 150, 115303 (2024).
52 Tang Z. et al. The Etching Behaviour and Fluorine-Based-Plasma Resistance of YOF Coatings Deposited by Atmospheric Plasma Spraying. Coatings 14, 1091 (2024).
53 Ashizawa H. & Yoshida K. Plasma-resistance evaluation of yttrium oxyfluoride coating prepared by aerosol deposition method. International Journal of Applied Ceramic Technology 19, 375-382 (2022).
54 Tsunoura T., Yoshida K., Yano T. & Kishi Y. Fabrication, characterization, and fluorine-plasma exposure behavior of dense yttrium oxyfluoride ceramics. Japanese Journal of Applied Physics 56, 06HC02 (2017).
55 Wen T. et al. Multicolour and up-conversion fluorescence of lanthanide doped Vernier phase yttrium oxyfluoride nanocrystals. Journal of Materials Chemistry C 1, 1995-2001 (2013).
56 Gaviría J. & Bohé A. Carbochlorination of yttrium oxide. Thermochimica Acta 509, 100-110 (2010).
57 Anderson A. & Mishra B. Investigation of the carbochlorination process for conversion of cerium and neodymium oxides into their chlorides. Journal of Sustainable Metallurgy 1, 189-198 (2015).
58 Strugovshchikov E. & Pishtshev A. Exploring The Anion Chemical Space: A Model of Electroelastic Material $Ln_2OF_{2-x}Cl_xH_2$ (Ln= Y, La, Gd) with High Mechanical Sensitivity and Remarkable Energy Harvesting. (2020).
59 Kageyama H. et al. Expanding frontiers in materials chemistry and physics with multiple anions. Nature Communications 9, 772, (2018).
60 Cornelius S. et al. Oxyhydride Nature of Rare-Earth-Based Photochromic Thin Films. The Journal of Physical Chemistry Letters, 1342-1348, (2019).

61 Maehlen J. P., Mongstad T. T., You C. C. & Karazhanov S. Lattice contraction in photochromic yttrium hydride. Journal of alloys and compounds 580, S119-S121 (2013).
62 Montero J. et al. Photochromic mechanism in oxygen-containing yttrium hydride thin films: An optical perspective. Physical Review B 95, 201301, (2017).
63 Baba E. M., Montero J., Strugovshchikov E., Zayim, E. Ö. & Karazhanov, S. Light-induced breathing in photochromic yttrium oxyhydrides. Physical Review Materials 4, 025201 (2020).
64 Komatsu Y. et al. Repeatable photoinduced insulator-to-metal transition in yttrium oxyhydride epitaxial thin films. Chemistry of Materials 34, 3616-3623 (2022).
65 Arslan H., Pudza I., Kuzmin A. & Karazhanov S. Evidence of local structural distortions and subtle thermal disorder in transparent photochromic yttrium oxyhydride. Applied Physics Letters 124 (2024).
66 Moldarev D. et al. Yttrium oxyhydrides for photochromic applications: Correlating composition and optical response. Physical Review Materials 2, 115203 (2018).
67 Moldarev D. et al. Photochromic properties of yttrium oxyhydride thin films: Surface versus bulk effect. Materialia 11, 100706 (2020).
68 Moldarev D. et al. Composition of photochromic oxygen-containing yttrium hydride films. Solar Energy Materials and Solar Cells 177, 66-69 (2018).
69 Arslan H. et al. Chemical state and atomic structure in stoichiovariants photochromic oxidized yttrium hydride thin films. Zeitschrift für Physikalische Chemie 0 (2024).
70 Kantre K., Moro M. V., Moldarev D., Wolff M. & Primetzhofer D. Synthesis and in-situ characterization of photochromic yttrium oxyhydride grown by reactive e^--beam evaporation. Scripta Materialia 186, 352-356 (2020).
71 Pitthan E. et al. In-situ, real-time investigation of the formation of oxygen-containing rare-earth hydrides by combining a quartz crystal microbalance and ion beam analysis. Materialia 27, 101675 (2023).
72 Zapp N., Auer H. & Kohlmann, H. YHO, an air-stable ionic hydride. Inorganic Chemistry 58, 14635-14641 (2019).
73 Yamashita H. et al. Chemical Pressure-Induced Anion Order–Disorder Transition in LnHO Enabled by Hydride Size Flexibility. Journal of the American Chemical Society 140, 11170-11173, (2018).
74 Sørby M. H., Martinsen F., Karazhanov S. Z., Hauback B. C. & Marstein E. S. On the Crystal Chemistry of Photochromic Yttrium Oxyhydride. Energies 15, 1903 (2022).

75 Pishtshev A. & Karazhanov S. Z. Role of oxygen in materials properties of yttrium trihydride. Solid state communications 194, 39-42 (2014).
76 Aðalsteinsson S. et al. Correlating chemical composition and optical properties of photochromic rare-earth oxyhydrides using ion beam analysis. Nuclear Instruments and Methods in Physics Research Section B: Beam Interactions with Materials and Atoms 485, 36-40 (2020).
77 Sorby M. H. et al. The crystal structure of $Zr_2NiD_{4.5}$. Acta Crystallographica Section B-Structural Science 62, 972-978 (2006).
78 Hans M. et al. Photochromic mechanism and dual-phase formation in oxygen-containing rare-earth hydride thin films. Advanced Optical Materials 8, 2000822 (2020).
79 Moro M. V., Aðalsteinsson S. M., Moldarev D., Wolff M. & Primetzhofer D. Photochromism in Isotopically Labeled Oxygen-Containing Yttrium–Hydride and Deuteride Thin-Film Systems. physica status solidi (RRL) – Rapid Research Letters 16, 2100508, (2022).
80 Seshan K. Handbook of thin film deposition. (William Andrew, 2012).
81 Mattox D. M. Handbook of physical vapor deposition (PVD) processing. (William Andrew, 2010).
82 Nastasi M. Ion-solid Interactions: Fundamentals and Applications. (Cambridge University Press, 1996).
83 Fuller L. Physical vapor deposition–evaporation and sputtering. Microelectronic Engineering Rochester Institute of Technology (2011).
84 Shah S. I., Jaffari G. H., Yassitepe E. & Ali, B. Evaporation: Processes, bulk microstructures, and mechanical properties. Handbook of Deposition Technologies for Films and Coatings, 135-252 (2010).
85 Chen Z. et al. UV-vis Spectroscopy. Photoelectrochemical water splitting: standards, experimental methods, and protocols, 49-62 (2013).
86 Swinehart D. F. The beer-lambert law. Journal of chemical education 39, 333 (1962).
87 Perkampus, H.-H. UV-VIS Spectroscopy and its Applications. (Springer Science & Business Media, 2013).
88 Huray P. G. Maxwell's equations. (John Wiley & Sons, 2009).
89 Lvovsky A. I. Fresnel equations. Encyclopedia of Optical Engineering 27, 1-6 (2013).
90 Mistrik J., Kasap S., Ruda H. E., Koughia C. & Singh, J. Optical properties of electronic materials: fundamentals and characterization. Springer handbook of electronic and photonic materials, 1-1 (2017).

91 Gonçalves D. & Irene E. A. Fundamentals and applications of spectroscopic ellipsometry. Química Nova 25, 794-800 (2002).
92 Li L., Lei J., Wu L. & Pan, F. in Handbook of Modern Coating Technologies 45-83 (Elsevier, 2021).
93 Irene E. b. H. G. T. a. E. A. Handbook of Ellipsometry. Springer Berlin, Heidelberg (2005).
94 Glatzel P. & Juhin A. X-ray Absorption and Emission Spectroscopy. Local Structural Characterisation: Inorganic Materials Series, 89-171 (2013).
95 Newville M. Fundamentals of XAFS. Reviews in Mineralogy and Geochemistry 78, 33-74 (2014).
96 Als-Nielsen J. & McMorrow, D. Elements of modern X-ray physics. (John Wiley & Sons, 2011).
97 Auger P. The auger effect. Surface Science 48, 1-8 (1975).
98 Burhop E. H. S. The Auger effect and other radiationless transitions. (Cambridge University Press, 2014).
99 Rehr J. J. & Albers R. C. Theoretical approaches to x-ray absorption fine structure. Reviews of modern physics 72, 621 (2000).
100 Kalinko, A. XAESA v.0.07, 2023. https://gitlab.desy.de/aleksandr.kalinko/xaesa.
101 Newville M. in Journal of Physics: Conference Series. 012007 (IOP Publishing).
102 Ravel B. & Newville, M. ATHENA, ARTEMIS, HEPHAESTUS: data analysis for X-ray absorption spectroscopy using IFEFFIT. Journal of synchrotron radiation 12, 537-541 (2005).
103 Newville M. EXAFS analysis using FEFF and FEFFIT. Journal of synchrotron radiation 8, 96-100 (2001).
104 Abraham F. F. Computational statistical mechanics methodology, applications and supercomputing. Advances in Physics 35, 1-111 (1986).
105 Van Gunsteren W. F. & Berendsen H. J. Computer simulation of molecular dynamics: methodology, applications, and perspectives in chemistry. Angewandte Chemie International Edition in English 29, 992-1023 (1990).
106 Kuzmin A. & Evarestov R. Quantum mechanics–molecular dynamics approach to the interpretation of X-ray absorption spectra. Journal of Physics: Condensed Matter 21, 055401 (2009).
107 Timoshenko J. et al. Neural network approach for characterizing structural transformations by X-ray absorption fine structure spectroscopy. Physical review letters 120, 225502 (2018).
108 Kuno A. & Matsuo M. Nondestructive speciation of solid mixtures by multivariate calibration of X-ray absorption near-edge structure using artificial neural networks and partial least-squares. Analytical sciences 16, 597-602 (2000).

109 Timoshenko J., Lu D., Lin Y. & Frenkel A. I. Supervised machine-learning-based determination of three-dimensional structure of metallic nanoparticles. The journal of physical chemistry letters 8, 5091-5098 (2017).
110 Tucker M. G., Dove M. T. & Keen D. A. Application of the reverse Monte Carlo method to crystalline materials. Journal of applied crystallography 34, 630-638 (2001).
111 Keen D., Tucker M. & Dove M. Reverse Monte Carlo modelling of crystalline disorder. Journal of Physics: Condensed Matter 17, S15 (2005).
112 Tucker M. G., Keen D. A., Dove M. T., Goodwin A. L. & Hui Q. RMCProfile: reverse Monte Carlo for polycrystalline materials. Journal of Physics: Condensed Matter 19, 335218 (2007).
113 Petkov V. et al. Periodicity and atomic ordering in nanosized particles of crystals. The Journal of Physical Chemistry C 112, 8907-8911 (2008).
114 Kuzmin A. & Chaboy J. EXAFS and XANES analysis of oxides at the nanoscale. IUCrJ 1, 571-589 (2014).
115 Timoshenko J., Kuzmin A. & Purans J. EXAFS study of hydrogen intercalation into ReO_3 using the evolutionary algorithm. Journal of Physics: Condensed Matter 26, 055401 (2014).
116 Timoshenko J., Kuzmin A. & Purans J. Reverse Monte Carlo modeling of thermal disorder in crystalline materials from EXAFS spectra. Computer Physics Communications 183, 1237-1245 (2012).
117 Timoshenko J. Reverse Monte Carlo modelling of structural and thermal disorder in crystalline materials. PhD thesis, Department of Physics and Mathematics, University of Latia (2015).
118 Timoshenko J. & Kuzmin A. Wavelet data analysis of EXAFS spectra. Computer Physics Communications 180, 920-925 (2009).
119 Metropolis N., Rosenbluth A. W., Rosenbluth M. N., Teller A. H. & Teller E. Equation of state calculations by fast computing machines. The journal of chemical physics 21, 1087-1092 (1953).
120 Chantler C., Bunker B. & Boscherini F. International Tables for Crystallography, Volume I: X-ray absorption spectroscopy and related techniques. Vol. 1 (John Wiley & Sons, 2024).
121 Koningsberger D., Mojet B., Van Dorssen G. & Ramaker D. XAFS spectroscopy; fundamental principles and data analysis. Topics in catalysis 10, 143-155 (2000).
122 Pudža I. Impact of the local structure on the thermochromic properties of copper molybdate and its solid solutions. (2022).
123 Humphreys C. The significance of Bragg's law in electron diffraction and microscopy, and Bragg's second law. Acta Crystallographica Section A: Foundations of Crystallography 69, 45-50 (2013).

124 Lee M. X-Ray diffraction for materials research: from fundamentals to applications. (CRC Press, 2017).
125 Seeck O. H. & Murphy, B. X-ray diffraction: modern experimental techniques. (CRC Press, 2015).
126 Chastain J. & King Jr R. C. Handbook of X-ray photoelectron spectroscopy. Perkin-Elmer Corporation 40, 221 (1992).
127 Greczynski G. & Hultman L. X-ray photoelectron spectroscopy: towards reliable binding energy referencing. Progress in Materials Science 107, 100591 (2020).
128 Stevie F. A. & Donley C. L. Introduction to x-ray photoelectron spectroscopy. Journal of Vacuum Science & Technology A 38 (2020).
129 Greczynski G. & Hultman L. A step-by-step guide to perform x-ray photoelectron spectroscopy. Journal of Applied Physics 132 (2022).
130 Zhou W., Apkarian R., Wang Z. L. & Joy D. Fundamentals of scanning electron microscopy (SEM). Scanning microscopy for nanotechnology: techniques and applications, 1-40 (2007).
131 De Broglie L. Matter and Light-The New Physics. (Read Books Ltd, 2013).
132 Goldstein J. I. et al. Scanning electron microscopy and X-ray microanalysis. (springer, 2017).
133 Williams D. B., Carter C. B., Williams D. B. & Carter C. B. The transmission electron microscope. (Springer, 1996).
134 Zuo J. M. & Spence J. C. Advanced transmission electron microscopy. (Springer, 2017).
135 Radamson H. H., Hallén A., Sychugov I. & Azarov A. Analytical methods and instruments for micro-and nanomaterials. (Springer, 2023).
136 Watts J. F., Wolstenholme J. & Webb R. P. Secondary ion mass spectrometry. Characterization of Materials, 1-33 (2002).
137 McPhail D. Applications of secondary ion mass spectrometry (SIMS) in materials science. Journal of materials science 41, 873-903 (2006).
138 Benninghoven A., Rudenauer F. & Werner H. W. Secondary ion mass spectrometry: basic concepts, instrumental aspects, applications and trends. (1987).
139 Wilson R. G., Stevie F. A. & Magee C. W. Secondary ion mass spectrometry: a practical handbook for depth profiling and bulk impurity analysis. (1989).
140 Mayer M. in Workshop on Nuclear Data for Science and Technology: Materials Analysis.
141 Chu W.K. Backscattering spectrometry. (Elsevier, 2012).
142 Berger P., Raepsaet C. & Khodja H. Elastic Recoil Detection Analysis. Neutron Scattering and Other Nuclear Techniques for Hydrogen in Materials, 277-314 (2016).

143 Friedbacher G. & Bubert H. Surface and thin film analysis: a compendium of principles, instrumentation, and applications. (John Wiley & Sons, 2011).
144 Bardeen J. Electrical conductivity of metals. Journal of Applied Physics 11, 88-111 (1940).
145 Set F.V. Encyclopedia of Modern Optics. (2005).
146 Rockett A. The materials science of semiconductors. (Springer Science & Business Media, 2007).
147 van der Pauw L. J. A method of measuring the resistivity and Hall coefficient on lamellae of arbitrary shape. Philips technical review 20, 220-224 (1958).
148 Zhang T., Ma S., Xing F. & Zhang L. Diffusivities and atomic mobilities in α-Y (O) and α-Y_2O_3 and their applications to oxidation of pure α-Y during the initial stage. Solid State Ionics 361, 115559 (2021).
149 Djurovic D., Zinkevich M. & Aldinger F. Thermodynamic modeling of the yttrium–oxygen system. Calphad 31, 560-566 (2007).
150 Yamamoto T., Kaminaga K., Saito D., Oka D. & Fukumura T. High electron mobility with significant spin-orbit coupling in rock-salt YbO epitaxial thin film. Applied Physics Letters 114 (2019).
151 Kaminaga K., Oka D., Hasegawa T. & Fukumura T. New lutetium oxide: Electrically conducting rock-salt LuO epitaxial thin film. ACS omega 3, 12501-12504 (2018).
152 Yamamoto T., Kaminaga K., Saito D., Oka D. & Fukumura, T. Rock salt structure GdO epitaxial thin film with a high ferromagnetic Curie temperature. Applied Physics Letters 117 (2020).
153 Schmehl A. et al. Epitaxial integration of the highly spin-polarized ferromagnetic semiconductor EuO with silicon and GaN. Nature materials 6, 882-887 (2007).
154 Sasaki S. et al. A high-TC heavy rare earth monoxide semiconductor TbO with a more than half-filled 4f orbital. Dalton Transactions 51, 16648-16652 (2022).
155 E. Welter R. C., M. Herrmann R. Nemausat. p. 1-6. (AIP Conference Proceedings).
156 Nefedov V., Gati D., Dzhurinskii B., Sergushin N. & Salyn Y. V. X-ray electron study of oxides of elements. Zhurnal Neorganicheskoi Khimii 20, 2307-2314 (1975).
157 Vasquez R., Foote M. & Hunt B. Reaction of nonaqueous halogen solutions with $YBa_2Cu_3O_{7-x}$. Journal of Applied Physics 66, 4866-4877 (1989).
158 Hayoz J. et al. Preparation and characterization of clean, single-crystalline YH_x films ($0 \leqslant x \leqslant 2.9$) on W (110). Journal of Vacuum Science & Technology A: Vacuum, Surfaces, and Films 18, 2417-2431 (2000).

159 Greczynski G. & Hultman L. Towards reliable X-ray photoelectron spectroscopy: sputter-damage effects in transition metal borides, carbides, nitrides, and oxides. Applied Surface Science 542, 148599 (2021).
160 Mongstad T., Thøgersen A., Subrahmanyam A. & Karazhanov S. The electronic state of thin films of yttrium, yttrium hydrides and yttrium oxide. Solar energy materials and solar cells 128, 270-274 (2014).
161 Fujimori A. & Schlapbach L. Electronic structure of yttrium hydride studied by X-ray photoemission spectroscopy. Journal of Physics C: Solid State Physics 17, 341 (1984).
162 Hughes A. & Sexton B. Comments on the use of implanted Ar as a binding energy reference. Journal of electron spectroscopy and related phenomena 50, C15-C18 (1990).
163 Pearce S. J., Parker G. J., Charlton M. D. & Wilkinson J. S. Structural and optical properties of yttrium oxide thin films for planar waveguiding applications. Journal of Vacuum Science & Technology A: Vacuum, Surfaces, and Films 28, 1388-1392 (2010).
164 Gaboriaud R., Pailloux F., Guerin, P. & Paumier, F. Yttrium oxide thin films, Y_2O_3, grown by ion beam sputtering on Si. Journal of Physics D: Applied Physics 33, 2884 (2000).
165 Mongstad T. et al. Surface oxide on thin films of yttrium hydride studied by neutron reflectometry. Applied Physics Letters 100 (2012).
166 Powell C. J. Recommended Auger parameters for 42 elemental solids. Journal of Electron Spectroscopy and Related Phenomena 185, 1-3 (2012).
167 Majumdar D. & Chatterjee D. X-ray photoelectron spectroscopic studies on yttria, zirconia, and yttria-stabilized zirconia. Journal of applied physics 70, 988-992 (1991).
168 Baba Y. & Sasaki T. A. Chemical states and thermal stability of hydrogen-implanted Ti and V studied by X-ray photoelectron spectroscopy. Journal of Nuclear Materials 132, 173-180 (1985).
169 Mai L. et al. Water assisted atomic layer deposition of yttrium oxide using tris (N, N′-diisopropyl-2-dimethylamido-guanidinato) yttrium (iii): process development, film characterization and functional properties. RSC advances 8, 4987-4994 (2018).
170 Kudo Y., Yoshida N., Fujimoto M., Tanaka K. & Toyoshima, I. Acid-dissociation behavior of para-hydroxyl group in the N, N, O-terdentate ligand, 4-(4-methyl-2-pyridylazo) resorcinol, coordinated to a transition metal ion. Bulletin of the Chemical Society of Japan 59, 1481-1486 (1986).
171 Guo X., Sun Y.Q. & Cui K. Darkening of zirconia: a problem arising from oxygen sensors in practice. Sensors and Actuators B: Chemical 31, 139-145 (1996).

172 Aspnes D., Theeten J. & Hottier F. Investigation of effective-medium models of microscopic surface roughness by spectroscopic ellipsometry. Physical Review B 20, 3292 (1979).
173 Jonane I. et al. Temperature-dependent EXAFS study of the local structure and lattice dynamics in cubic Y_2O_3. Journal of synchrotron radiation 23, 510-518 (2016).
174 Bonnet M., Delapalme A. & Fuess H. Redetermination of the scattering length of yttrium. Acta Crystallographica Section A: Crystal Physics, Diffraction, Theoretical and General Crystallography 31, 264-265 (1975).
175 Arslan H. et al. Anion vacancy-induced photochromism and lattice relaxation in yttrium oxyhydride.
Preprint https://doi.org/10.21203/rs.3.rs-5171857/v1 (2024).
176 Ramírez R., Tardío M., González R., Chen Y. & Kokta M. R. Photochromism of vacancy-related defects in thermochemically reduced α-Al_2O_3:Mg single crystals. Applied Physics Letters 86, (2005).
177 Akiyama M., Yamada H. & Sakai K. Photochromism enhancement in reduced tridymite $BaMgSiO_4$ by Fe-doping. Journal of the Ceramic Society of Japan 119, 338-341, (2011).
178 Colinet P. et al. The structural origin of the efficient photochromism in natural minerals. Proceedings of the National Academy of Sciences 119, e2202487119, (2022).
179 Understanding the CIE system. International Commission on Illumination, CIE Publication.
180 Sansonetti J. E. & Martin W. C. Handbook of basic atomic spectroscopic data. Journal of physical and chemical reference data 34, 1559-2259 (2005).
181 Lide D. R. CRC handbook of chemistry and physics. Vol. 85 (CRC press, 2004).
182 Andersen T., Haugen H. & Hotop H. Binding energies in atomic negative ions: III. Journal of Physical and Chemical Reference Data 28, 1511-1533 (1999).
183 Williams G. P. Electron binding energies of the elements. CRC Handbook of Chemistry and Physics, 92nd edition, Section 10, 221-226 (1992).
184 Book G. 5. Electronic Structure of the Elements. Rn 7, 4.0727.
185 Gary L. Miessler, Fischer Paul J & A, T. D. Inorganic Chemistry. Pearson.
186 Clementi E., Raimondi D. & Reinhardt W. P. Atomic screening constants from SCF functions. II. Atoms with 37 to 86 electrons. The Journal of chemical physics 47, 1300-1307 (1967).
187 Waldron K. A., Fehringer E. M., Streeb A. E., Trosky J. E. & Pearson J. J. Screening percentages based on Slater effective nuclear charge as

a versatile tool for teaching periodic trends. Journal of Chemical Education 78, 635 (2001).
188 Firestone R. B. & Shirley, V. (Wiley, New York, 1996).
189 Krause M. O. Atomic radiative and radiationless yields for K and L shells. Journal of physical and chemical reference data 8, 307-327 (1979).
190 Campbell J. Fluorescence yields and Coster–Kronig probabilities for the atomic L subshells. Atomic Data and Nuclear Data Tables 85, 291-315 (2003).
191 Kittel C. & McEuen P. Introduction to solid state physics. (John Wiley & Sons, 2018).
192 Yaws C. L. The yaws handbook of physical properties for hydrocarbons and chemicals: physical properties for more than 54,000 organic and inorganic chemical compounds, Coverage for C1 to C100 Organics and Ac to Zr Inorganics. (Gulf Professional Publishing, 2015).
193 Ho C. Y., Powell R. W. & Liley P. E. Thermal conductivity of the elements. Journal of Physical and Chemical Reference Data 1, 279-421 (1972).
194 Horvath A. Critical temperature of elements and the periodic system. Journal of Chemical Education 50, 335 (1973).
195 Cohen R. E., Lide D. & Trigg G. Physicist's Desk Reference. (Springer Science & Business Media, 2003).
196 De Podesta M. Understanding the properties of matter. (CRC Press, 2020).
197 Stewart G. Measurement of low-temperature specific heat. Review of Scientific Instruments 54, 1-11 (1983).
198 Yaws C. L. Liquid Density Of the Elements. Chemical Engineering 114 (2007).
199 Prohaska T. et al. Standard atomic weights of the elements 2021 (IUPAC Technical Report). Pure and Applied Chemistry 94, 573-600 (2022).
200 Singman C. N. Atomic volume and allotropy of the elements. Journal of Chemical Education 61, 137 (1984).
201 Samsonov G. V. Handbook of the Physicochemical Properties of the Elements. (Springer Science & Business Media, 2012).
202 Barsan M. E. NIOSH pocket guide to chemical hazards. (2007).
203 Cardarelli F. Materials handbook: a concise desktop reference. (2008).
204 Hamlin J., Tissen V. & Schilling J. Superconductivity at 20 K in yttrium metal at pressures exceeding 1 Mbar. Physica C: Superconductivity and its applications 451, 82-85 (2007).
205 Hamlin J., Tissen V. & Schilling J. Superconductivity at 17 K in yttrium metal under nearly hydrostatic pressures up to 89 GPa.

Physical Review B Condensed Matter and Materials Physics 73, 094522 (2006).
206 Huheey J. E., Keiter E. A., Keiter R. L. & Medhi O. K. Inorganic chemistry: principles of structure and reactivity. (Pearson Education India, 2006).
207 Sanderson R. Principles of electronegativity Part I. General nature. Journal of Chemical Education 65, 112 (1988).
208 Allred A. L. & Rochow E. G. A scale of electronegativity based on electrostatic force. Journal of Inorganic and Nuclear Chemistry 5, 264-268 (1958).
209 Allred A. L. Electronegativity values from thermochemical data. Journal of inorganic and nuclear chemistry 17, 215-221 (1961).
210 Smith D. W. Electronegativity in two dimensions: reassessment and resolution of the Pearson-Pauling paradox. Journal of Chemical Education 67, 911 (1990).
211 Ghosh D. C. & Gupta K. A new scale of electronegativity of 54 elements of periodic table based on polarizability of atoms. Journal of Theoretical and Computational Chemistry 5, 895-911 (2006).
212 Nagle J. K. Atomic polarizability and electronegativity. Journal of the American Chemical Society 112, 4741-4747 (1990).
213 Pearson R. G. Absolute electronegativity and hardness: application to inorganic chemistry. Inorganic chemistry 27, 734-740 (1988).
214 Mann J. B., Meek T. L., Knight E. T., Capitani J. F. & Allen L. C. Configuration energies of the d-block elements. Journal of the American Chemical Society 122, 5132-5137 (2000).
215 Smith D. W. Inorganic substances: a prelude to the study of descriptive inorganic chemistry. (Cambridge university press, 1990).
216 Waber J. & Cromer D. T. Orbital radii of atoms and ions. The Journal of Chemical Physics 42, 4116-4123 (1965).
217 Pyykkö P. & Atsumi M. Molecular single-bond covalent radii for elements 1–118. Chemistry–A European Journal 15, 186-197 (2009).
218 Pyykkö P. & Atsumi M. Molecular double-bond covalent radii for elements Li–E112. Chemistry–A European Journal 15, 12770-12779 (2009).
219 Pyykkö P., Riedel S. & Patzschke M. Triple-bond covalent radii. Chemistry–A European Journal 11, 3511-3520 (2005).
220 Cordero B. et al. Covalent radii revisited. Dalton Transactions, 2832-2838 (2008).
221 Pauling L. The nature of the chemical bond, 3rd edn Cornell University Press. Ithaca, NY, 236 (1960).
222 Batsanov S. S. Van der Waals radii of elements. Inorganic materials 37, 871-885 (2001).
223 Slater J. C. Atomic radii in crystals. The Journal of Chemical Physics 41, 3199-3204 (1964).

224 Emsley J. Nature's building blocks: an AZ guide to the elements. (Oxford University Press, USA, 2011).
225 Bratsch S. G. Revised Mulliken electronegativities: I. Calculation and conversion to Pauling units. Journal of Chemical Education 65, 34 (1988).
226 Silbey R. J., Alberty R. A., Papadantonakis, G. A. & Bawendi, M. G. Physical chemistry. (John Wiley & Sons, 2022).
227 Bondi A. v. van der Waals Volumes and Radii. The Journal of physical chemistry 68, 441-451 (1964).

Chapter 11

Appendix

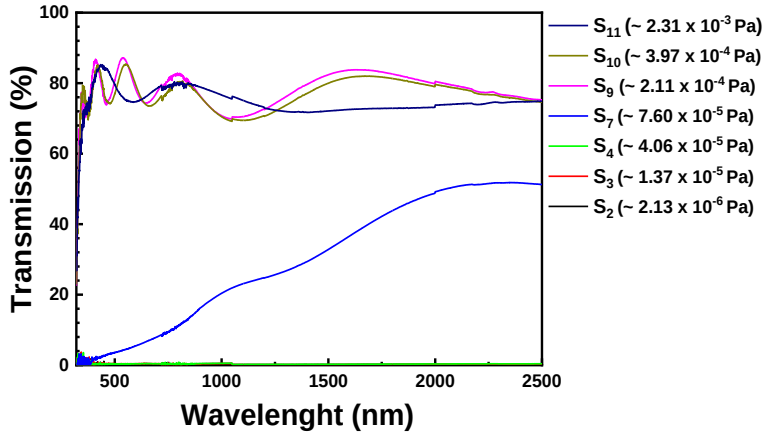

Figure A-1 | Optical characterization of Y/YO thin films on soda-lime glass substrates. Transmission measurements of metallic (S_2, S_3, S_4), insulating (semi-transparent/S_7), and insulating (transparent/S_9, S_{10}, S_{11}) thin films. The corresponding oxygen partial pressure levels under which the thin films were produced are indicated in parentheses.

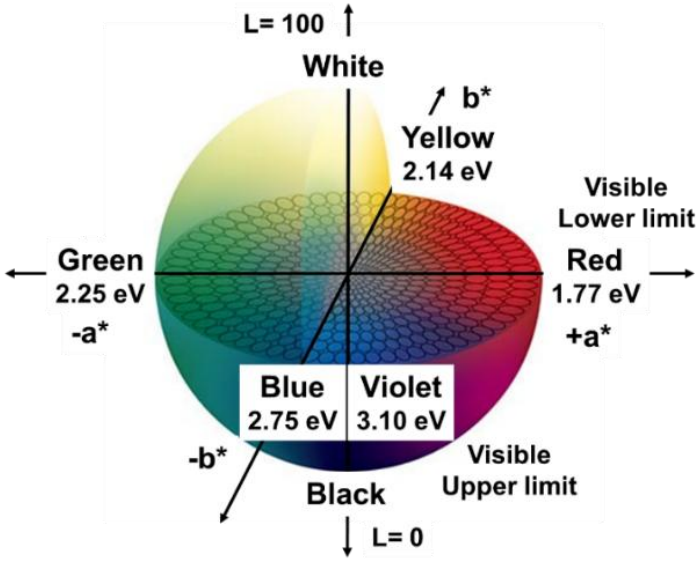

Figure A-2 | Color space diagram. Energy levels of visible light wavelengths, illustrated on a CIELAB[179] color space diagram, showing the full range of colors perceived by the human eye.

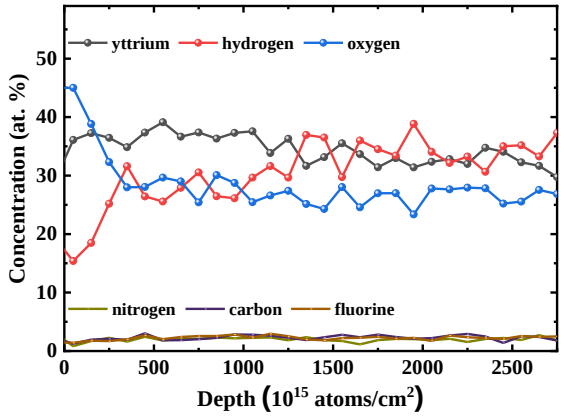

FIgure A-3 | Compositional analyses of photochromic YHO. Depth profile of chemical elements in the sample derived from ToF-ERDA

Table A-1 | Yttrium. Extensive data on atomic structure, physical properties, and thermodynamics.

Yttrium (Y)		
Yttrium Atomic Structure		
Ionization Energies	I (1)	6.2173 eV [180]
	II (2)	12.224 eV [180]
	III (3)	20.52 eV [181]
Electron Affinity		0.307 ∓ 0.012 eV [181]
		2480 ∓ 100 cm^{-1} [182]
Electron Binding Energies	K (1s)	17038 eV [183]
	LI (2s)	2373 eV [183]
	LII ($2p_{1/2}$)	2156 eV [183]
	LIII ($2p_{3/2}$)	2080 eV [183]
	MI (3s)	392.0 eV [183]
	MII ($3p_{1/2}$)	310.6 eV [183]
	MIII ($3p_{3/2}$)	298.8 eV [183]
	MIV ($3d_{3/2}$)	157.7 eV [183]
	MV ($3d_{5/2}$)	155.8 eV [183]
Electron Configuration	Orbital Occupancy	[Kr] $4d^1$ $5s^2$ [184]
	Orbital Filling Order	[Kr] $5s^2$ $4d^1$ [185]
	Term Symbol	$^2D_{3/2}$ [184]
Clementi-Raimondi Effective Nuclear Charge	**5s**	
	Orbital Exponent	1251 [186]
	Principle Quantum Number	5 [186]
	Effective Nuclear Charge	6.256 [186]
	4d	
	Orbital Exponent	3.989 [186]
	Principle Quantum Number	4 [186]
	Effective Nuclear Charge	15.958 [186]
Screening Percentage		91.4% [187]
Fluorescence Yields	wk	0.716 [188]
	wL1	0.0059 [188]
	wL2	0.026 [188]
	wL3	0.028 [188]
Coster-Kronig Yields	F12	0.26 [189]
	F13	0.57 [190]
	F23	0.094 [190]
Yttrium Crystal Structure	Allotrope	α-yttrium [181]
	Symbol	αY
	Allotrope	β-yttrium
	Symbol	βY [181]
Nearest Neighbor Distance (300 K, 1 atm)		355 pm [191]
Atomic Concentration (300 K, 1 atm)		3.02 $x10^{22}$ cm^{-3} [191]

Table A-1 | Continued.

Yttrium Thermodynamics		
Melting Point (1 atm)		1795 K [192]
Boiling Point (1 atm)		3618 K [192]
Thermal Conductivity (solid)	400 K, Polycrystalline	18.0 W/(m K) [193]
	300 K, Polycrystalline	17.2 W/(m K) [193]
	298 K, Polycrystalline	17.2 W/(m K) [193]
	273 K, Polycrystalline	17.0 W/(m K) [193]
	200 K, Polycrystalline	16.6 W/(m K) [193]
Critical Point		8950 K [194]
Vapor Pressure	3607 K	100 kPa [195]
	3036 K	10 kPa [195]
	2627 K	1 kPa [195]
	2320 K	100 Pa [195]
	2075 K	10 Pa [195]
	1883 K	1 Pa [195]
Enthalpy of Fusion (1 atm)		17.2 kJ/mol [196]
Enthalpy of Vaporization (1 atm)		393.3 kJ/mol [196]
Isobaric Molar Heat Capacity (298 K, 1 bar)		26.53 J/(mol K) [181]
Isobaric Specific Heat Capacity (298 K, 1 bar)		0.298 J/(g K) [181]
Electronic Heat Capacity Coefficient		8.2 mJ/(mol K^2) [197]
Debye Temperature	Room Temperature (298K)	214 K [197]
	Low-Temperature Limit (0K)	248 K [193]
Yttrium Physical Properties		
Density	Liquid, 1795 K	4,240 g/ml [198]
	Solid, 298 K	4,469 g/cm^3 [192]
Molar Mass	Rounded	88.91 g/mol [199]
	Standard	88.90585 + 0.00002 g/mol [199]
Molar Volume (solid, 298 K, 1 atm)		19.88 cm^3/mol [200]
Physical Form		silvery metal [192]
Linear Thermal Expansion Coefficient (298 K)		$10.6x10^{-6}$ K^{-1} [195]
Speed of Sound (solid, 293 K)		3300 m/s [201]
Specific Gravity (68 °F, water at 4 °C (39.2 °F))		4.47 [202]
Young's Modulus		63.5 Gpa [203]
Poisson's Ratio		0.243 [203]
Electrical Resistivity (solid, 295 K)		$58.5x10^{-6}$ Ohm.cm [191]
Superconducting Transition Temperature	115 GPa	20K [204]
	89.3 GPa	17K [205]
	30 GPa	3.5K [205]
Isothermal Bulk Modulus (300 K)		36.6 Gpa [191]
Isothermal Compressibility (300 K)		0.0273 GPa^{-1} [191]

Table A-1 | Continued.

Yttrium Atomic Interaction		
Oxidation States		3+ [46]
		2+ [46]
Pauling Electronegativity		
Oxidation state: 3+		1.22 [206]
Sanderson Electronegativity	Oxidation State: 3+	0.65 [207]
	Oxidation State: 2+	0.40 [207]
Allred-Rochow Electronegativity		
Oxidation State: 3+		1.11 [208]
Allred Electronegativity		
Oxidation State: 3+		1.22 [209]
Smith Electronegativity		
Oxidation State: 3+		1.2 [210]
Ghosh-Gupta Electronegativity		2.7237 eV [211]
Nagle Electronegativity		1.11 eV [212]
Pearson Absolute Electronegativity		3.19 eV [213]
Chemical Hardness		3.19 eV [213]
Configuration Energy	Electron Volt Units	6.631 eV [214]
	Pauling Units	1.12 [214]
Cohesive Energy	Per Mole	422 kJ/mol [191]
	Per Atom	4.37 eV/atom [191]
Yttrium Atomic Size	Atomic Radius	182 pm [215]
	Orbital Radius	169.3 pm [216]
Pyykkö Covalent Radius	Single Bond	163 pm [217]
	Double Bond	130 pm [218]
	Triple Bond	124 pm [219]
Cordero Covalent Radius		190 pm [220]
Shannon-Prewitt Crystal Radius, ion charge: 3+	Coordination Number 6	104.0 pm [37]
	Coordination Number 7	110.0 pm [37]
	Coordination Number 8	115.9 pm[37]
	Coordination Number 9	121.5 pm [37]
Shannon-Prewitt Effective Ionic Radius, ion charge: 3+	Coordination Number 6	90.0 pm [37]
	Coordination Number 7	96.0 pm [37]
	Coordination Number 8	101.9 pm [37]
	Coordination Number 9	107.5 pm [37]
Pauling Empirical Crystal Radius, ion charge: 3+		93 pm [221]
Pauling Univalent Radius, ion charge: 1+		120 pm [221]
Batsanov Crystallographic Van Der Waals Radius		240 pm [222]
Batsanov Equilibrium Van Der Waals Radius		271 pm [222]
Slater Atomic-Ionic Radius		180 pm [223]

Table A-2 | Oxygen. Basic data on atomic structure, physical properties, and thermodynamics.

Oxygen (O)			
Ionization Energies		I (1)	13.61805 eV [181]
		II (2)	35.121 eV [181]
		III (3)	54.935 eV [181]
Electron Affinity			1.461 ∓ 0.0000027 eV [182]
			11784.664 ∓ 0.022 cm^{-1} [182]
Electron Binding Energies		K (1s)	543.1 eV [183]
		LI (2s)	42.6 eV [183]
Electron Configuration		Orbital Occupancy	[He] $1s^2$ $2s^4$ [206]
		Orbital Filling Order	[He] $2s^2$ $2p^4$ [185]
		Term Symbol	$^3P_2$ [184]
Clementi-Raimondi Effective Nuclear Charge	1s	Orbital Exponent	7.6579 [186]
		Principle Quantum Number	1 [186]
		Effective Nuclear Charge	7.6579 [186]
	2s	Orbital Exponent	2.2458 [186]
		Principle Quantum Number	2 [186]
		Effective Nuclear Charge	4.4916 [186]
	2p	Orbital Exponent	2.2266 [186]
		Principle Quantum Number	2 [186]
		Effective Nuclear Charge	4.4532 [186]
Screening Percentage			43.1% [187]
Oxidation States			2 [46]
			1 [46]
			0 [224]
			-1 [46]
			-2 [46]
Pauling Electronegativity			3.44 [209]
Mulliken-Jaffe Electronegativity		hybrid: sp^2	3.94 [225]
		hybrid: sp^3	3.68 [225]
		hybrid: 16.7% s	3.41 [225]
		orbital p	2.82 [225]
Sanderson Electronegativity			3.65 [207]
Allred-Rochow Electronegativity			3.50 [208]
Allred Electronegativity, Oxidation State: 2+			3.44 [209]
Smith Electronegativity, Oxidation State: 2-			3.65 [210]
Ghosh-Gupta Electronegativity			8.7861 eV [211]
Nagle Electronegativity			3.62 eV [212]
Pearson Absolute Electronegativity			7.54 eV [213]

Table A-3 | Hydrogen. Basic data on atomic structure, physical properties, and thermodynamics.

Hydrogen (H)		
Ionization Energies	I (1)	13.5984 eV [180]
Electron Affinity		0.7542 ∓ 0.00000003 eV [182]
		6083.0641 ∓ 0.000030 cm^{-1} [182]
Electron Binding Energies	K (1s)	13.6 eV [183]
Electron Configuration	Orbital Occupancy	$1s^1$ [206]
	Orbital Filling Order	$1s^1$ [185]
	Term Symbol	$^2S_{1/2}$ [184]
Screening Percentage		0% [187]
Oxidation States		1 [224]
		0 [224]
		-1 [224]
Pauling Electronegativity		2.20 [209]
Mulliken-Jaffe Electronegativity, Orbital s		2.25 [225]
Sanderson Electronegativity		2.592 [207]
Allred-Rochow Electronegativity		2.20 [206]
Allred Electronegativity, Oxidation State: 1+		2.20 [209]
Smith Electronegativity	Oxidation State: 1+	2.1 [210]
	Oxidation State: 1-	2.0 [210]
Ghosh-Gupta Electronegativity		7.1862 eV [211]
Nagle Electronegativity		2.27 eV [212]
Pearson Absolute Electronegativity		7.18 eV [213]
Hydrogen Atomic Size	Atomic Radius	37 pm [215]
	Orbital Radius	52.9 pm [226]
Pyykkö Covalent Radius	Single Bond	32 pm [217]
Cordero Covalent Radius		31 pm [220]
Shannon-Prewitt Crystal Radius ion charge: 1+	Coordination Number 1	-24 pm [37]
	Coordination Number 2	-4 pm [37]
Shannon-Prewitt Effective Ionic Radius ion charge: 1+	Coordination Number 1	-38 pm [37]
	Coordination Number 2	-4 pm [37]
Pauling Empirical Crystal Radius	ion charge: 1-	208 pm [221]
Pauling Univalent Radius	ion charge: 1-	208 pm [221]
Bondi Van Der Waals Radius		120 pm [227]
Pauling Van Der Waals Radius		120 [221]
Slater Atomic-Ionic Radius		25 pm [223]